INFORMATION TO USERS

University of Alberta

Damage Investigations of Glass Fibre/Epoxy Resin Composite Laminates Under Cyclic Loading

by

Alan W. Wharmby   ©

A thesis submitted to the Faculty of Graduate Studies and Research in partial fulfillment of the requirements for the degree of Master of Science

Department of Mechanical Engineering

Edmonton, Alberta

Spring, 2000

Canada

University of Alberta

Library release form

Name of Author: Alan William Wharmby

Title of Thesis: Damage Investigations of Glass Fibre/Epoxy Resin Composite Laminates Under Cyclic Loading.

Degree: Master of Science

Year this Degree Granted: 2000

11044 80 Ave
Edmonton, AB
T6G 0R3
Canada

January 28, 2000

University of Alberta

Faculty of Graduate Studies and Research
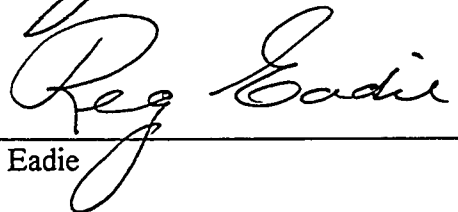
The undersigned certify that they have read, and recommended to the Faculty of Graduate Studies and Research for acceptance, a thesis entitled Damage Investigations of Glass Fibre/Epoxy Resin Composite Laminates Under Cyclic Loading submitted by Alan William Wharmby in partial fullfillment of the requirements for the degree of Master of Science.

Dr. F.Ellyin

Dr. Z. Xia

Dr. R.L. Eadie

2000/01/27

Abstract

This study was separated into two components.

In the first component, cyclic loading of cross-ply and multi-ply specimens was examined. $(0_2/90_3)_s$ and $(\pm 45/90_3)_s$ laminates were tested under quasi-static and cyclic loading. Damage curves for crack initiation, delamination initiation, and final failure were developed. Visual damage growth, transverse crack growth, and stiffness reduction measurements were examined to determine how and why damage grew throughout the specimens.

In the second component, constrained angle ply specimens were examined. Laminates with orientations of $(0/\pm\theta_4/0)_T$ where $\theta = 25$, 45, and 75 degrees were tested under monotonic and cyclic loading. For these specimens damage curves for crack initiation, crack saturation, and delamination initiation were developed. Visual damage growth was compared with stiffness reduction measurements and correlations were observed between the two. Visual damage was examined using a microscope to examine the edges, and an image processor to examine through the width of the specimen.

Acknowledgements

List of Tables

List of Figures

1   Introduction

The use of continuous fibre composite materials has grown enormously during the latter half of this century. From their beginnings as a high strength material mainly employed in costly military aviation projects, their use has spread to many different civilian applications. New designs range from aeroplane parts such as rudders and wings for commercial aircraft to sporting equipment such as handlebars and frames for mountain bikes. In recent years composite materials have been studied for applications such as pressure vessels and piping.

Advanced composite materials are unique mainly because of the ability to tailor design the material properties for a required application. By varying the orientation of the fibres in the laminate, it can be optimized for strength and stiffness, or on the other hand optimized for improved ductility. With this ability comes the benefit of a lighter material with better corrosion resistance compared to conventional homogeneous materials such as steel.

One of the drawbacks of composites is an incomplete understanding of their damage characteristics. By studying how damage initiates and propagates in a composite material under both uniaxial and multiaxial loading conditions, during both monotonic and cyclic loading, a clearer concept of how the material behaves can be gained. A better understanding of the material properties could lead to reduced safety factors, lower costs, superior design, and the institution of new applications. The purpose of this thesis is to examine how continuous fibre composite materials behave under cyclic loading conditions.

A large amount of work has already been performed in the area of cyclic loading in composite laminates. Inspite of this, a full understanding of how damage initiates and propagates through a laminate is not yet clear. It is still very difficult to predict how damage will propagate in composites with varying lay-ups. How the damage initiates is also not fully understood. These fundamental problems need to be solved before critical component design with composites can take place.

1.1   Differences between Composite Laminates and Metals

There are many differences between a composite laminate and an isotropic metal that cause conventional damage analysis to be ineffective.

Whereas a metal can usually be considered as an isotropic material, a composite laminate must be considered anisotropic. Since a composite is much stronger in the direction of the fibres, the strength characteristics will vary depending on the orientation examined. In a composite laminate, elastic moduli E_{11}, E_{22}, and E_{33} vary greatly, whereas in a metal these directional properties are relatively close to one another.

The main difference between the behaviour of metals and laminated composites is the failure mode. Whereas a metal has mainly one dominant failure mode that consists of a crack propagating through the material, a composite laminate has many failure modes. These consist of microdamage, transverse cracking, delamination, and fibre-failure and will be discussed in Section 1.2. Also, whereas the damage mode in a metal consists of a single dominant event, the overall damage progression in a composite laminate is a multiplicity of interacting and competing failure modes. Experiments have shown that

these different modes vary between specimens depending on lay-up of the laminae plies

with respect to the applied loading conditions, loading rate and amplitude, loading type,

dimensions of the specimens and whether the specimens are tubular or coupon in shape.

Damage in composites occurs on different scales. The first damage mode, microdamage,

is usually defect induced and occurs at the microscopic scale. On the other hand, damage

such as transverse cracking, delamination, and fibre failure occur in the macroscopic

scale of the specimen.

It is these differences that differentiate examination of composites from that of

metals.

1.2   Description of Damage in Composites

Damage growth has different modes during the life of a composite laminate.

These do not simply proceed one after the other, but occur as competing events that

interact with one another. These different modes of damage can be split into four distinct

and different types of damage.

1.2.1   Microdamage

The first type of damage growth in a composite laminate as it is being loaded is

microdamage. This damage develops throughout the specimen and is due to defects in

the laminate. A noticeable scaling effect can be seen in composite specimens, whereby

larger specimens fail under lower stresses than smaller specimens. This is due to the

effect of microvoids in the specimen [1-3]. The defects can be in the form of microvoids,

damage caused by residual stresses, areas of high or low fibre content, impurities inserted during the manufacturing of the laminate, and small defects in the initial fibre and matrix mixture that emerge during production of the fibres. This damage is exclusively in the microscale, yet it has been shown that this damage serves as an initiation site for macroscopic scale matrix cracking [4,5].

Microvoids can sometimes appear due to improper lay-up of the laminae in the specimen, which results in trapped air voids between individual plies [6]. They can also emerge due to improper vacuuming after lay-up, which has been found to reduce trapped air in the specimens. To reduce this type of microdamage individual laminae must be pressed together tightly when producing the laminate. Added pressure during the cure cycle of the composite should also be performed to extricate as many voids as possible.

High or low fibre content is seen when too little or too much pressure is applied when curing the composite. When there is high fibre content in the laminate, the fibres can cluster together with no polymer matrix between them. Stress concentrations arise and are likely sites for damage initiation in the specimen. On the other hand, areas of low fibre content have an abundance of polymer. In these regions, when a crack initiates, it can propagate very easily without hitting any restricting boundaries such as fibres. These are also sites for likely damage initiation in the specimen. Any void in the matrix is a potential site of stress concentration and could result in crack initiation.

The last type of microdamage is defects that arise during manufacture of the laminate. This can be in the form of interfibre cracking, debonds between the fibre and the matrix, and broken fibres. These develop due to residual stresses in the composite.

Residual stresses are the result of different expansion and contraction properties between the fibres and matrix. When the specimen is cured the matrix and fibres expand. After curing, when the specimen cools, the two different materials contract at different rates, leaving residual stresses that may initiate microdamage [7]. This microdamage, once initiated, is distributed throughout the specimen.

1.2.2 Matrix Cracking

The second type of damage consists of matrix cracking. Matrix cracking takes place in two forms. The first is a combination of fibre and matrix decohesion, and the second is interfibre matrix cracking. This damage is usually a growth from defects in the material, such as microdamage or from defects at the edges of cut composites, and is distinguished from microcracking by the formation of macroscopic cracks. These cracks typically run parallel to the fibre direction and through the thickness of the ply. Work performed by Reifsnider et al.[8,9] on transverse cracking (matrix cracking perpendicular to the loading direction) found that there was a point where the accumulation of matrix cracks saturated and new damage modes took place instead. He called this the Characteristic Damage State (CDS). This is simply a semi-uniformly distributed pattern of matrix cracks that form in a laminate for any cyclic loading condition. Figure 1.1 shows a typical matrix crack through a laminae ply of a composite specimen. The dark areas surrounding the individual fibres are resin, and the crack has propagated vertically down the middle of the image.
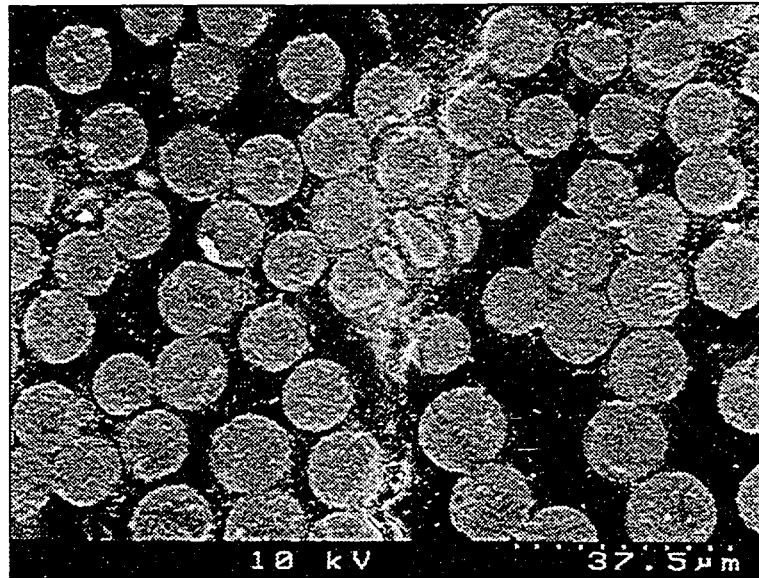
Figure 1.1. Typical matrix cracking in a glass fibre/epoxy resin laminae ply

1.2.3 Delamination

Delamination damage is separation of layers due to differences in properties between the plies. When the stiffness variance between differing ply orientations is large, and when there is a defect such as a transverse crack [10,11] or a geometric boundary such as a free edge [12,13], delaminations can initiate and propagate.

Delaminations usually follow matrix cracking in the tensile coupon testing of a specimen. During cyclic loading a matrix crack propagates until it reaches a constraining boundary, i.e. varying angle plies. When this happens, the crack takes the path of least resistance, which often can be propagation between the two plies. This crack then becomes a delamination. Figure 1.2 shows a matrix crack that has propagated until it reached a boundary and then proceeded into a delamination. The delamination can be

seen on the far right side of the figure and propagates in both directions from the matrix

crack.
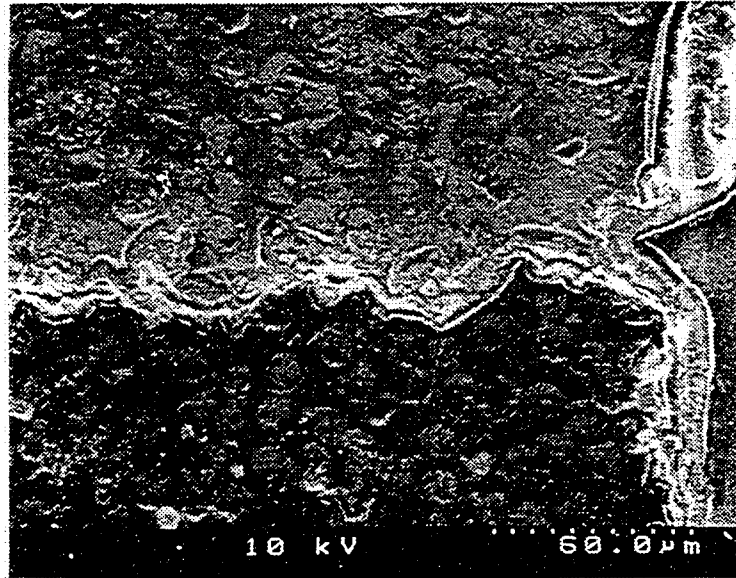
Figure 1.2: Delamination growth between 90° and 0° ply where transverse crack has
propagated into a delamination

It has been noticed that varying types of delamination occur in different

specimens. Whereas a cross-ply laminate will have delaminations that grow throughout

the length of the 0° plies, a quasi-isotropic or angle-ply specimen will experience

delamination in a concentrated cross-section. It is these delamination characteristics that

determine the ultimate failure of the specimen.   In the cross-ply laminates, the

delaminations grow throughout the length of the specimen until a final brush failure

results.   (See Figure 1.3).   In the angle ply and quasi-isotropic specimens the

delamination growth occurs in a smaller cross-section which results in ultimate failure.

(See Figure 1.4).
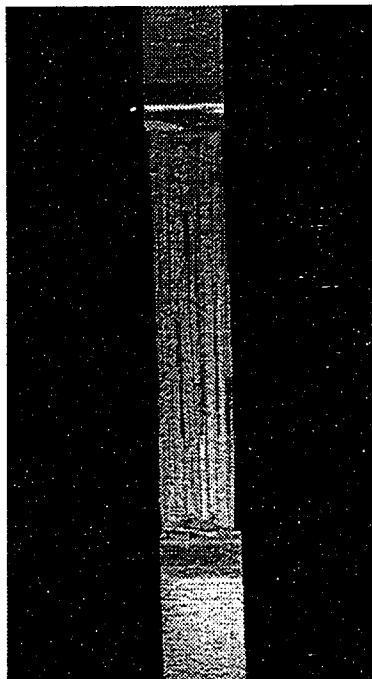
Figure 1.3. Brush failure due to lengthwise delamination growth in a $(0_2/90_3)_s$ laminate
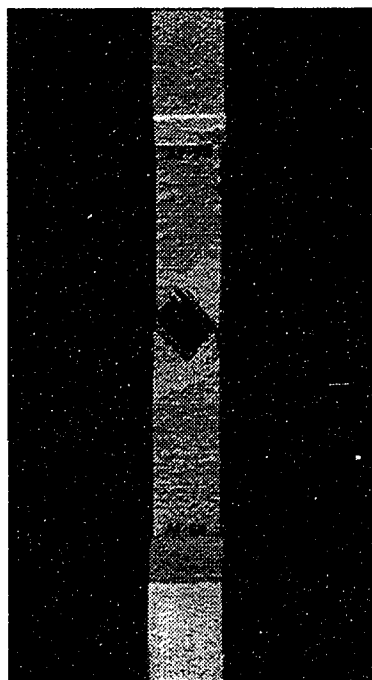
Figure 1.4. Failure due to widthwise delamination growth in a $(\pm45/90_3)_s$ laminate

1.2.4   Fibre Failure

Fibre failure is the final mode of damage in a specimen. This mode is the result of the tensile strength of the fibres themselves being exceeded. This type of damage typically takes place when all other modes of damage have been exhausted, since the strongest part of the composite constituents is the fibres. This damage results in the ultimate failure of the laminate for fibre dominated loading.

Figure 1.5 shows a common fibre-failure in the constraining 0° plies of a cross-ply laminate. The fibres have fractured across the cross-section and there is considerable fibre pull-out, as shown by the long fibre strands.
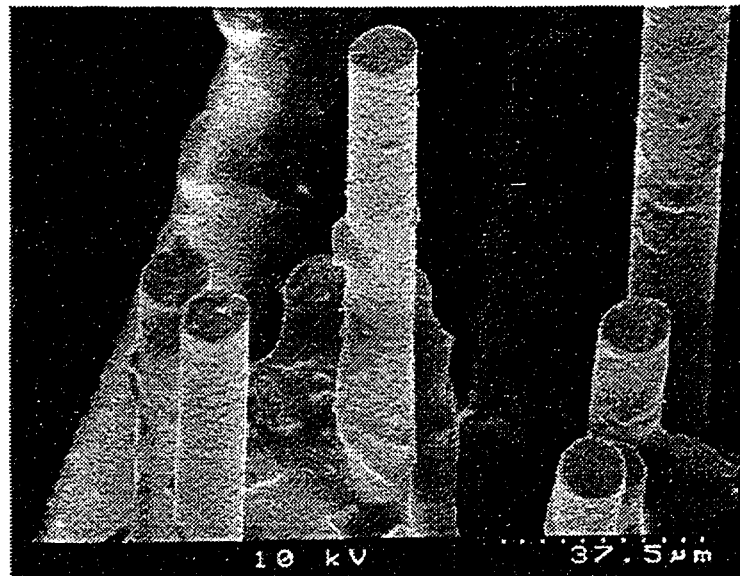
Figure 1.5. Fibre failure in constraining plies of a $(0_2/90_3)_s$ laminate
(Courtesy of Rohrbacher [27])

Although most fatigue-life curves for composites are plotted with respect to the final fibre failure of the specimen, such a curve does not show all of these damage modes, and conveys nothing of the preceding damage that has taken place in the specimen.

1.3   Types of Composite Laminates

There are various geometries of laminates used in fibre/resin composite experimentation. The orientation of the fibres in a composite can be described by a standard set of symbols. The standard laminate description consists of the angle that the plies are oriented with respect to the loading direction, and are organized from the outside inwards. An example is $(0_2/90_3)_s$. This description implies that the outer plies are oriented $0°$ with respect to the direction of loading. The subscript '2' indicates that there are two plies in this direction. Next are the inner $90°$ plies. The subscript here shows there are three such plies. The 's' subscript outside of the brackets indicates that the laminate is symmetric with respect to the mid-plane. In total there are ten plies in this description in a configuration of (0/0/90/90/90/90/90/90/0/0). In some laminate descriptions the subscript 'S' is replaced with a 'T' representing the total lay-up.

The types of specimens examined can be split into four different categories, described on the following pages:

1.3.1 Cross-ply : $(0_m/90_n)_s$

Cross-ply specimens are made up of varying numbers of plies that are oriented in two directions. The plies are either in the direction of loading ($0°$ plies), or in the direction perpendicular to loading ($90°$ plies). These specimens are useful in examining the damage that occurs in the matrix of the specimen. A typical cross-ply specimen would be $(0/90/0)$, $(0_2/90_3)_s$, or $(0_n/90_m)_s$.

1.3.2 Uni-directional : (θ_n)

Uni-directional specimens are made up of varying numbers of plies of specimens all oriented in the same direction. These specimens are useful in determining the material properties of a single orientation of the test material.

1.3.3 Multi-directional : $(\pm\theta/90_n)_s$

Multi-directional specimens refer to those specimens that have a wide variety of differing laminae geometries. These are sometimes prepared with the fibres in many directions to give quasi-isotropic material properties for the composite laminate.

1.3.4 Angle-ply : $(\pm\theta)_{ns}$

Angle-ply specimens refer to those specimens that have plies of varying angle of orientation with respect to the direction of loading. These specimens are important to examine due to the fact that for many practical applications of composite laminates, the

plies are oriented in directions different from that of the direction of the largest load. The reason for this can be either multidirectional loading, or uncertainty in the actual direction of loading of the laminate.

1.4   Characterization of Damage in Composite Coupon Specimens

In the last 20 years a large amount of research has been aimed at the examination of damage growth in composite materials. Of considerable note, much work has been done on the cross-ply laminates, namely any laminates with an orientation of $(0_n/90_m)_s$. These have been examined in large part due to the ease of seeing the damage growth in the matrix dominated 90° layers. These lay-ups are also one of the easiest to model, since damage in the form of matrix cracking occurs almost exclusively in the 90° layers, and because the viscoelastic effects of the matrix can be minimized.

As early as 1969, the cyclic properties of composite materials were being examined. Boller [14] aimed his research at unidirectional specimens and found that the anisotropic nature of composite laminates lead them to be more complicated to analyze than isotropic materials such as metals. He found that the fatigue strength of composites was dependent upon the proper fibre to epoxy ratio. He also found that there were many factors that could effect the final fatigue properties of the composite laminate. These included the stiffness properties of the composite laminates, environmental factors, fabrication factors, and service factors. This was then classified into effects such as temperature, moisture, notches, imperfections, surface conditions, specimen size, damping characteristics, adhesion, orientation of fibres, and the rate of loading.

A large amount of experimental work has been performed trying to model the damage growth during cyclic loading of composite laminates. Much of this work has focused on the stiffness reduction over the life of the composite. Work performed by Highsmith and Reifsnider [8,9] found that the stiffness reduction was linked to the transverse matrix cracking in a cross-ply laminate. This work found that for a given laminate ply orientation, a characteristic damage state (CDS) occurred, whereby the matrix cracking in the cross-ply grew until it reached an approximately uniform crack pattern. They found that as matrix cracking increased in a specimen, the stiffness decreased in a very similar pattern, indicating that the matrix cracking was the dominant cause of the reduction in stiffness. The matrix cracking grew at a rapid rate at first and then slowed until a characteristic damage state was reached. In a similar manner, the stiffness reduction grew rapidly early on and reached a steady level as the CDS was reached. Another interesting point was that the largest stiffness changes developed when the crack density was the largest. Experimental plots of the stiffness reduction and the crack density were found to correlate well with theoretical shear lag analyses. Similar results were found by Camponeschi and Stinchcomb [15], Talreja [16], and by Ogin, Smith, and Beaumont [17].

Work performed in recent years by Crocker et al. [18] has focused on mixed mode transverse crack growth in (0/θ/0) specimens. Crack initiation and propagation was investigated for (0/θ/0) specimens with holes drilled in the θ layers to various depths before performing the tests. It was found that the matrix cracking of the specimens was dependent on the angle θ, while the depth the holes were drilled into the specimen had no

effect on the propagation rate of matrix cracks. With regard to the angle θ, they found that a (0/90/0) laminate is notch insensitive, while laminates that had a θ value between 45° and 75° were notch sensitive. This meant that there was an increase in the incremental strain required to grow a crack as the value of θ decreased.

Work was also performed by Tong, et al. [19] in the area of quasi-static and cyclic loading of quasi-isotropic laminates. Investigations were undertaken to see how matrix cracking grew in $(0/90/-45/+45)_s$ laminates. They found that there were large differences in the damage states between quasi-static and cyclic loading. Higher saturation crack densities were observed in the 90° layers under quasi-static loading than under cyclic loading, while the cyclic loading produced a larger reduction in stiffness, mainly due to extra damage accumulation in the ±45° layers. They noted that trying to model fatigue loading using simply static results could lead to non-conservative estimates of damage.

Angle-ply laminates were studied in a similar manner by Tahiri, Henaff-Gardin, and Lafarie-Frenot [20]. They studied a $(+45_2/-45_2)_{2s}$ specimen under both quasi-static and cyclic loading. They found that under quasi-static loading for this type of laminate there were large axial stiffness and shear modulus decreases. These decreases were largely attributed to non-linear visco-plastic and visco-elastic phenomena occurring in the matrix of the laminate. Under cyclic loading they found that the axial stiffness and shear modulus reductions fell by only 9% before failure of the specimen. They reasoned that the non-linear visco-elastic and visco-plastic effects did not have time to manifest under the higher strain rates that the specimens underwent in cyclic loading.

Another study by Henaff-Gardin and Lafarie-Frenot consisted of examining the crack growth in two different carbon/epoxy cross-ply specimens under cyclic loading [21]. The two specimens examined were a $(0_3/90/0_4)_s$ specimen and a $(0_7/90)_s$ specimen. These specimens had equivalent numbers of 0° and 90° layers, with the only difference being the stacking sequence. The purpose of this study was to see what the effect of the total of the 90° plies thickness had on the transverse cracking in the specimen. They found that for similar cyclic tests, the $(0_7/90)_s$ specimen produced approximately half (2 cracks/mm) of the final number of transverse cracks that the $(0_3/90/0_4)_s$ specimen produced (4.4 cracks/mm). A crack onset delay was found to occur in both specimens. The crack onset delay for the $(0_3/90/0_4)_s$ specimens was 1000 times longer than for the $(0_7/90)_s$. This work suggested that for design purposes, thinner 90° plies are more favourable. Longer crack onset delays, lower cracked surface growth rates, and smaller cracked surface areas are the result of thinner transverse plies.

An examination of angle ply cracking in $(\pm\theta/-45_3/+45_3)_s$ glass-fibre/epoxy resin laminates undergoing monotonic loading was performed by J. Hoover [22]. He found that by adding constraining plies to a composite specimen the failure stress and strains increased. This effect increased as the θ angle decreased. It was also suggested that crack densities, and damage in plies was lower for specimens whose neighbouring plies were 'compatible plies'. Compatible plies are those plies that have angles of less than 30° between themselves. It was observed that no delamination grew between compatible plies. The only delamination growth was seen in 'incompatible plies' with larger stress and strain gradients. These tests were performed only under uniaxial monotonic loading.

The relevant angles between compatible plies may increase or decrease during cyclic loading. Further research is needed to determine if the above holds true for cyclic loading.

Hoover, Kujawski, and Ellyin [23] also looked into transverse cracking of symmetric and unsymmetric glass-fibre/epoxy-resin laminates under monotonic loading. Symmetric specimens with orientations of $(\pm\theta/90_3)_s$ with $\theta = 0°$, $25°$, and $45°$, and unsymmetric specimens with orientations of $(\pm\theta/90_6/0_2)_T$ with $\theta = 25°$ and $45°$ were examined. In this work the effect that transverse cracking had on the stiffness reduction of the specimen was studied. The findings showed that during a quasi-static test, three distinct damage stages took place. The first stage was before any transverse cracking materialized and was in a range of $0 - 0.5\%$ strain. The second stage was a linear range in which almost all of the transverse cracks emerged. The third and final stage had a large stiffness drop over a small range that was due to large scale delamination, fibre failure, and constrained ply cracking as well as some transverse cracking. It was in this third and final stage that the specimen failed.

Work performed by Kujawski [24] looked into the width effects of angle ply laminates under both monotonic and cyclic loading. He performed tests on six different $(\pm\theta_2)_s$ specimens with angles ranging from $\pm25°$ to $\pm75°$ and for five different widths. He found that as the angle decreases below $45°$, the effects of the specimen width becomes more pronounced. For specimens with fibre angles below $45°$, an increase in the specimen width led to an increase in both the tensile strength and fatigue life of the specimens. For specimens with fibre angles greater than $45°$ the width effects were less

pronounced. This study suggests that the edge effect may be similar between all specimens, although in relation to the overall cross-sectional area of a specimen it has less total effect on specimens with larger cross-sections.

A qualitative examination of the frequency-dependant behaviour of laminates under cyclic loading was also undertaken by Kujawski and Ellyin[25]. Through the examination of a matrix dominated specimen $((\pm 45)_{5s})$ they found that an accumulated cyclic creep occurred which depended on the frequency and applied load. Specimens at low loads and higher frequencies failed later than specimens at low loads and low frequencies. Specimens at higher loads and higher frequencies failed earlier than specimens at higher loads and lower frequencies. They also found that specimens had larger cyclic creep at the beginning and end of the fatigue tests, while there was a lower, steady creep rate throughout the rest of the specimen life. By examining the hysteresis loops of the specimens throughout their life, they also saw that there was a significant decrease in the stiffness of the specimen throughout its life.

1.5 Description of the Current Study

Work performed in the current study has two aims. The first objective is to examine damage growth and propagation between cross-ply and multi-ply laminates. The second objective is to examine the fatigue properties of constrained angle-ply laminates that have practical significance.

For the first objective, monotonic and cyclic tests are performed to investigate how the composite material varies with different loading conditions. Two different lay-

ups, one $(0_2/90_3)_s$ and the other $(\pm45/90_3)_s$, were examined. These specimens were chosen because the $(0_2/90_3)_s$ specimens produce ultimate failure modes that are dominated by the $0°$ fibres, while the $(\pm45/90_3)_s$ specimens produce ultimate failure modes that are dominated by the matrix in the $45°$ constraining plies. As well the $90°$ layers in both provided distinct matrix crack patterns for qualitative damage analysis. The differences between monotonic and cyclic loading was determined by examining parameters such as crack density, stiffness reduction, the achievement of a characteristic damage state, visual inspection of damage propagation, as well as fatigue life curves for the different lay-ups. Differences in cyclic loading between the two types of specimens were examined. The damage characteristics were also compared between the different loading types (load control vs. strain control), to study the laminate response to the loading mode.

The purpose of the second objective was to examine the cyclic properties of constrained angle-ply laminates with lay-ups similar to those that might be used in a high-pressure composite pipeline application. For this objective three different laminates were examined. These consisted of $(0/\pm\theta_4/0)$ laminates where θ was 25, 45, and 75 degrees. By producing fatigue life curves for the initiation of cracking, the onset of delimitation, and the saturation of matrix cracking in the specimens, an idea of the variance in damage with respect to θ could be determined.

2   Test Methodology

This chapter contains all procedures implemented in the manufacture and testing of the composite specimens. Described below are the types of specimens examined, preparation of the specimens, aspects of the testing machine and testing parameters used, the testing procedure, and methods of examining and recording the damage growth in the composite specimens.

2.1   Test Specimens

Various test geometries were fabricated for this study. For the first objective (Chapter 3) cross-ply and multi-ply laminates with a configuration of $(0_2/90_3)_s$ and $(\pm45/90_3)_s$ were examined. These specimens each had six 90° layers which produced highly visible through-width cracks when the specimen was loaded. The only variance between these two types of specimens was the constraining plies. In the $(0_2/90_3)_s$ specimen the 0° layers, which have the fibres in the direction of loading, produce a very strong and elastic constraint. This specimen is sometimes referred to as a fibre-dominated specimen. In the $(\pm45/90_3)_s$ specimen the load in the 45° layers was carried by both the matrix and the fibres. Because the matrix is the weaker of the two materials, it fails first. For this reason these specimens are sometimes called matrix-dominated specimens.

In the second objective (Chapter 4) three constrained angle ply specimens were prepared. These consisted of laminates with a geometry of $(0/\pm25_4/0)_T$, $(0/\pm45_4/0)_T$, and $(0/\pm75_4/0)_T$.

The geometry of all of the specimens examined was approximately 2.0-2.5 mm thick (depending on the number of plies) by 22 mm wide by 200 mm long.

2.2   Specimen Preparation

A large part of the validity of experimental testing can be attributed to quality control during fabrication of the test specimens. Factors that go into the specimen fabrication must be kept constant to ensure that all specimens have similar properties. These factors include specimen cure time, curing pressure, type of material, method of laying up the laminae, the cutting method, end-tab application, and storage of the specimens. By keeping these parameters the same between different tests, the results are more repeatable and any comparisons made between them can be deemed valid.

2.2.1   Material Examined

The type of material used in all tests consisted of 3M type 1003 (Scotchply) E-glass-fibre/epoxy resin. Pre-impregnated uni-directional tape rolls 0.3m wide by 66m long were acquired and pieces were cut into individual laminae. Each individual laminae was 0.2 mm thick. The hand lay-up techniques were used to produce a laminate sheet.

A complete set of material properties have been compiled by Hoover [26] for the 3M type 1003 E-glass-fibre/epoxy resin material and are presented in Table 2.1. These

values were used in the classical laminate theory calculations to determine the initial

stiffness of the specimens.   Since these results were compiled for specimens

manufactured with the same fabrication techniques used in this study, they are considered

the most repeatable.

Engineering Constant	Value
Longitudinal Modulus, E_1	43.2 GPa
Transverse Modulus, E_2	10.0 GPa
In-plane Shear Modulus, G_{12}	4.49 GPa
Out-of-plane Shear Modulus, G_{23}	4.17 GPa
In-plane Poisson ratio, v_{12}	0.31
Out-of-plane Poisson ratio, v_{23}	0.44
Co-efficient of linear expansion, α_1	8.6×10^{-6} per °C
Co-efficient of linear expansion, α_2	22.1×10^{-6} per °C
Temperature drop from stress-free temperature, ΔT	-125 °C
Specific Fracture Energy, γ_f	201 J/m^2
Average Ply Thickness	0.210 mm
Fibre Volume Fraction (After cure), v_f	52%

Table 2.1: Material properties of 3M type 1003 E-glass-fibre/epoxy resin composite as
manufactured at the University of Alberta (Courtesy of Hoover [26])

2.2.2 Laminate Manufacturing Method

Manufacture of the composite laminate was performed by first cutting individual

laminae from a tape roll of Scotchply pre-preg. The pre-preg roll was stored below 0°C

to ensure that no curing occurred in the epoxy before manufacturing the laminates. To

ensure that no condensation formed on the pre-preg, it was stored in a plastic bag while it

warmed up to room temperature. Laminae sheets approximately 200 mm by 153 mm

were cut by hand at varying angles relative to the fibre, so as to produce the required lay-

up. A sheet of release film was placed over the pre-preg, then a metal plate was placed

on the sheet to act as a cutting guide. A sharp utility knife was used to cut the sheets.

The method for cutting these individual plies of different orientations is shown in figures

2.1 and 2,2.
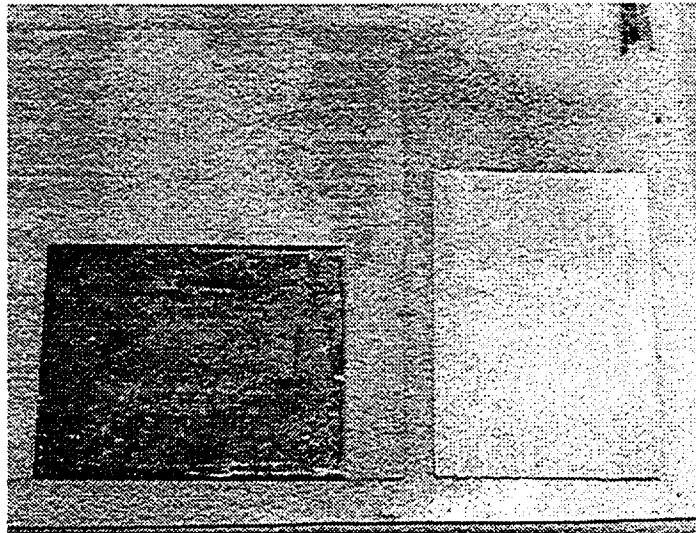
Figure 2.1: Cutting process for an individual 0° laminae ply
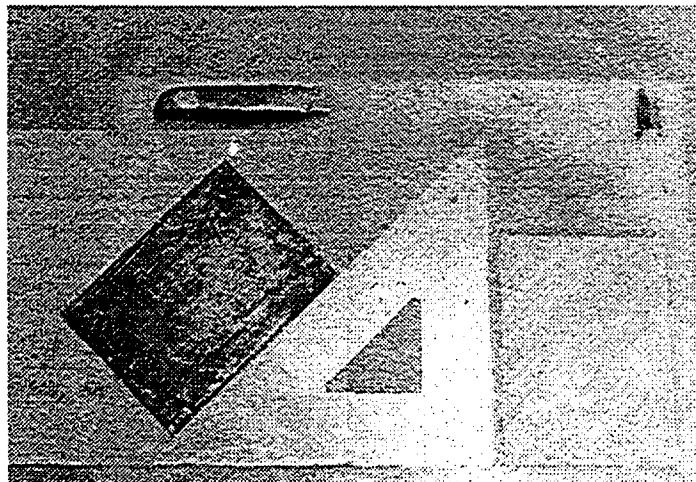
Figure 2.2: Cutting process for an individual 45° laminae ply

The individual laminae sheets were then pressed tightly together in a mold to get

as many voids out as possible. Figure 2.3 shows the process of cutting the pre-preg in

different orientations and constructing a laminate.
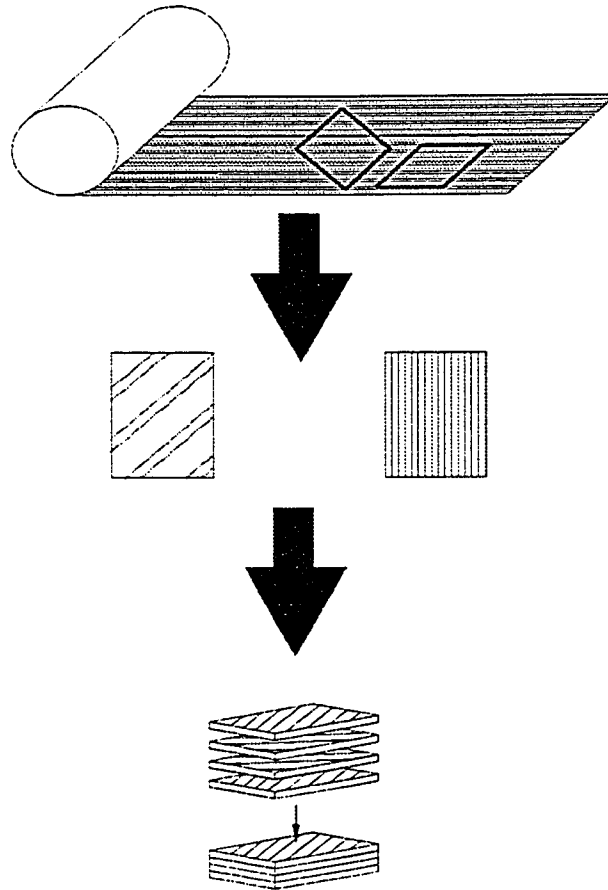
Figure 2.3: Manufacture of composite laminate sheet (Courtesy of Wolodko [29])

2.2.3   Vacuuming and Curing of the Laminate

After the laminae had been grouped into the laminate, the stack was placed in a vacuum chamber with a maximum pressure of 133 Pa for approximately 12 hours. This step was performed to reduce as much trapped air as possible from the specimen. Figure 2.4 shows a sketch of the specimen in the vacuum chamber apparatus.
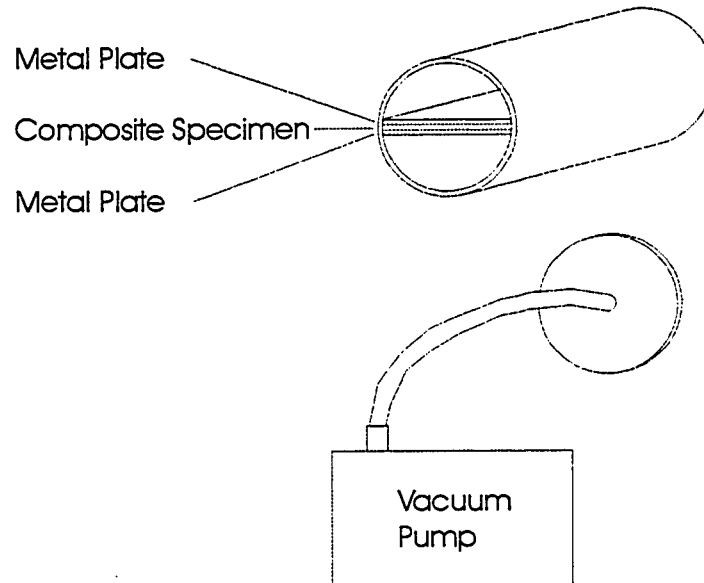
Figure 2.4: Vacuum chamber apparatus

After the laminate had been in the vacuum chamber, it was placed in a mold and cured in an oven at 150 °C under a bladder pressure of 25 psi for 12 hours. A schematic of the mold set-up is shown in Figure 2.5:

In the curing mold the metal plates are inserted to ensure that the specimen remains flat and uniform during curing. They also protect the specimen from pits and scratches that may be present on the mold.. The pressure bladder is used to push excess resin out of the composite laminate as it cures. The absorbent cloth is inserted to soak up resin that leaks from the mold during curing. Anti-cling film is placed on both sides of the specimen for ease of release after the curing process. Figure 2.6 shows the oven used in the curing process of the laminates. The pressure line was hooked up and run out through a hole in the oven wall.

This method produces a composite sheet of uniform thickness and fibre volume throughout the length and width of the specimen.

Upper layer of Mold

Pressure Bladder

Absorbent Cloth

Upper Metal Plate

Anti-Cling Film

Composite Specimen

Anti-Cling Film

Lower Metal Plate

Lower layer of Mold
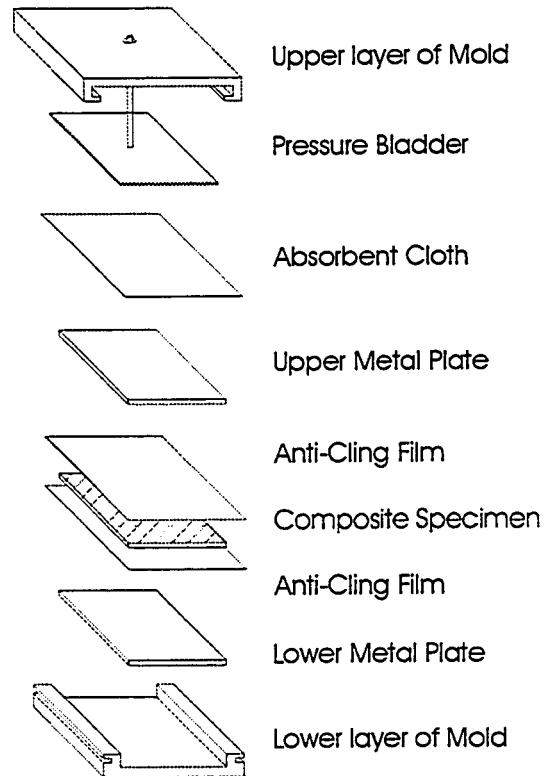
Figure 2.5: Schematic of composite curing mold
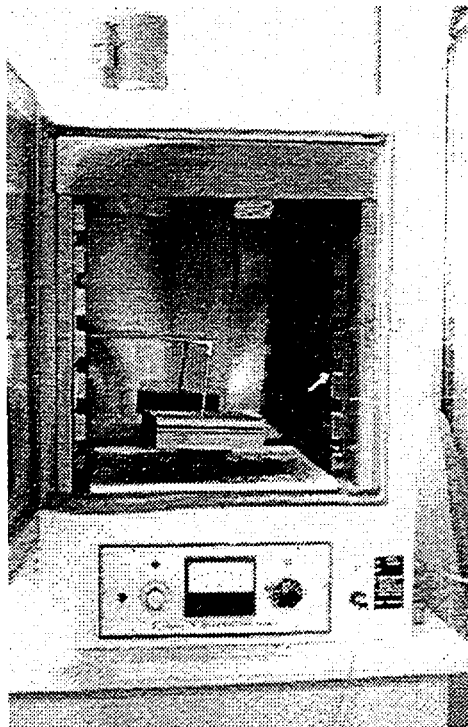
Figure 2.6: Specimen curing oven with pressure bladder attached to a mold

2.2.4 Cutting of Laminate into Individual Specimens

After the laminate is produced, it is cut into individual specimens. Six specimens can be cut from each composite sheet. A low RPM diamond blade saw fabricated at the University of Alberta is used to cut the specimens. This saw has been shown to reduce the number of edge defects when compared to conventional cutting techniques. Figures 2.7 and 2.8 show a typical specimen being cut using the diamond-blade saw.
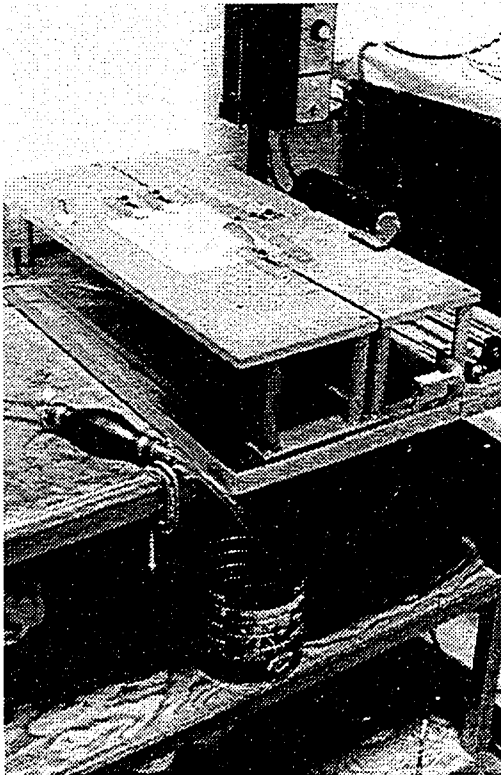
Figure 2.7: Diamond blade saw apparatus
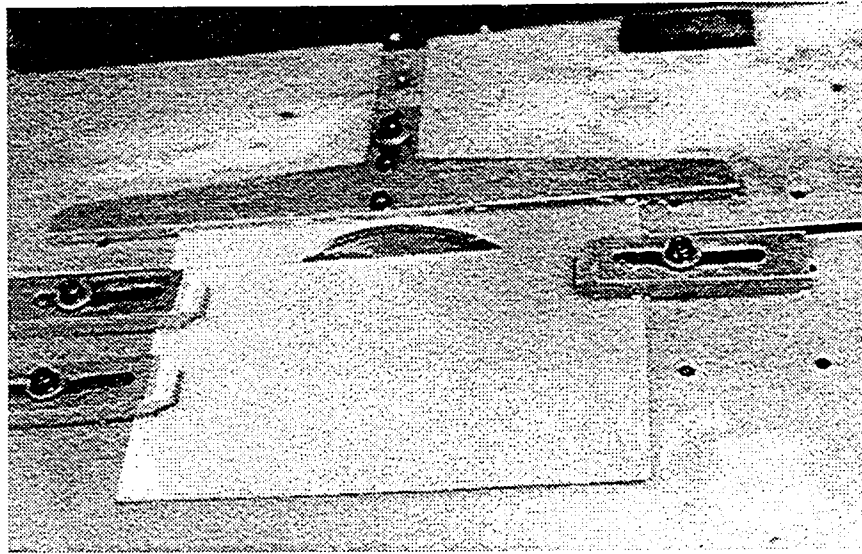
Figure 2.8: Specimen being cut using the diamond blade saw

2.2.5   Polishing of Specimens

To further ensure that edge effects are reduced, a systematic method of polishing

each individual specimen was developed. Each specimen was sanded using a Handimet

grinder in 240, 320, 400, and 600 grit sandpaper respectively. The specimens were

sanded for 30 seconds per side, for each of the different sandpaper grits. Afterwards the

polished surfaces were checked for abrasions and if any were found, the procedure was

repeated. Figures 2.9 and 2.10 show two scanning electron microscope images of

sections of the same specimen, the latter of which was polished using the above

procedure. In the first figure large areas of pitting and scratching are present, mainly

between the two plies of differing orientation. The second figure, under the same

magnification shows a much smoother surface. These defect areas can act as nucleation

sites that can affect the crack density, stiffness, and ultimate failure strength of the specimens.

Figure 2.9: Unpolished section of cross-ply laminate showing pitted areas between plies
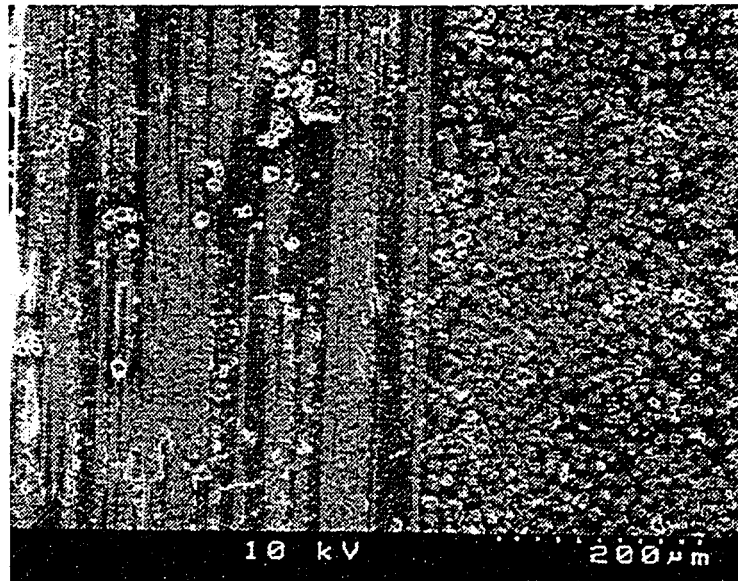
Figure 2.10: Similar specimen polished as specified, showing a cleaner surface

2.2.6 Measurement of Specimens

To determine the exact cross-sectional area of the specimens, measurements of the width and thickness were systematically taken and recorded. Measurements were taken at three different locations along the length of the specimen and an average of these three measurements was recorded. These values were used to calculate stress by dividing the load measured by the load cell by the cross-sectional area of the specimens.

2.2.7 Application of End Tabs

End tabs were applied to the specimens using 3M 12-hour epoxy adhesive. Earlier specimens had the end tabs applied with Loctite 380 but it was found that this didn't provide enough strength when the composite plies were oriented in the 0° direction. Failure in the tabs and slippage out of the tabs was observed in these specimens.

2.2.8 Marking Specimens for Image Processing

A marking system was used for each specimen so that the imaging system (Described in section 2.6.1) employed could track a constant area of the specimen between different images. This consisted of marking 'X's with permanent marker in the upper left and lower right hand corners of the specimens. As in-situ measurements were taken, the length between these markings increased, yet the final crack density could be calculated over the same initial area of the test.

2.2.9 Storage of Laminates and Completed Specimens

Previous work has shown that moisture can affect the material properties of a composite specimen [27]. Although the effects require a long time period and a significant amount of humidity on the surface, they could still affect the outcome of a test. To alleviate this problem, finished specimens were stored in a dessicator until they were taken for testing. The dessicator effectively removes any humidity from the environment of the specimens and leaves them in their original state.

2.3 Uniaxial Testing Machine

All specimen tests were performed on the same uniaxial testing machine. This consisted of a 100 kN MTS machine that was servo-controlled under a closed-loop. Coupled with the testing machine was a computer that controlled the loading conditions and also acquired data during the tests.

2.3.1 Data Acquisition System and Controlling Software

The Data acquisition system collected load and strain data throughout the life of the cyclic test. Measurements of stress were calculated using a 2000 lb load cell. These loads were converted into voltages for the data acquisition system where 1V was the equivalent to 2000 lbs. Measurements of strain were taken over a 75mm section of the specimen using an extensometer. Measurements of the strain were converted into voltages for the data acquisition system where 1V was the equivalent of an increase in strain of 1%.

Over the span of this investigation, three different data collection systems were employed.

The initial method consisted of simply hooking up a voltmeter to the testing machine and recording the output load and strain voltages over time. Any adjustments to achieve a set span and amplitude of the tests were done manually. It was impossible to obtain hysteresis loops of the specimens with this system. Another problem was that adjustments to achieve the required amplitude of load or strain had to be performed after the test had started. This resulted in it being very difficult to get accurate crack density measurements during the first 500 cycles of the test, when the amplitude of the test was being increased to that required. It was in this initial period that much of the damage took place in the highly stressed specimens.

The second method used a data acquisition card in conjunction with the testing machine. This was an older data acquisition system and all span and set point adjustments were still made manually. This again resulted in difficulty in data acquisition during the first 500 cycles, as well as the problem of keeping the set point and span at constant values. The system recorded data points so hysteresis loops could be examined throughout the life of the specimen. This data collection system was used when looking at the cross-ply and multi-ply specimens, specifically the $(0_2/90_3)_s$ and $(\pm45/90_3)_s$ specimens.

The third and best method of control and data acquisition was achieved through using a data acquisition software program called MTM301 developed in-house at the University of Alberta by Wolodko [29]. This program consisted of controlling software

that would automatically ramp to the set point and span of the cyclic tests instantly. It was able to stop the test at regularly scheduled intervals so that damage detection methods could be implemented. Accurate stiffness reduction information and crack growth data could be found for the initial cycles of the test. This software was used mainly with the $(0/\pm25_4/0)$, $(0/\pm45_4/0)$, and $(0/\pm75_4/0)$ specimens.

2.4   Testing Parameters

2.4.1   Frequency and R-ratio

The tests were performed at a frequency of 3.0 Hz. A sinusoidal waveform was used for all tests. The R-ratio (R=Pmin/Pmax) throughout all tests was chosen to be 0.1.

2.4.2   Load Control

Load control tests were performed on the multi-ply $(\pm45/90_3)_s$ and cross-ply $(0_2/90_3)_s$ specimens. It was found that under load control the specimens failed at lower initial loading conditions than under strain control. This is because during cyclic loading damage initiates and propagates with increased number of cycles. To maintain the same maximum and minimum load amplitude, the strain amplitude and maximum strain must increase. This results in more damage, which then results in even larger strains. This process of a continuous increase in strain is called cyclic creep. Eventually the strains increase to the point of ultimate failure of the specimen. Figure 2.11 shows typical hysteresis loops for a load-controlled test.
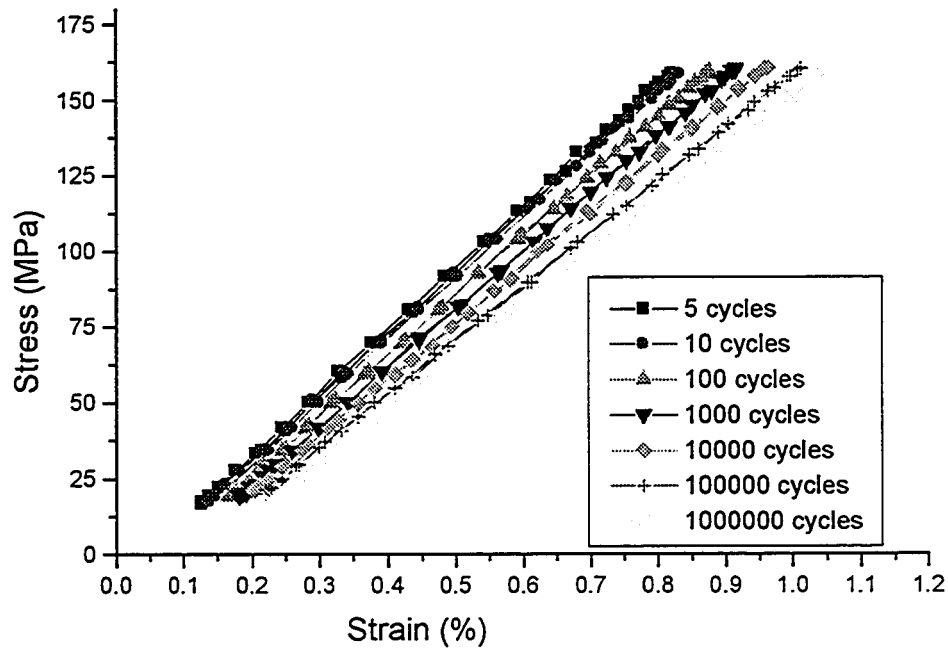
Figure 2.11: Hysteresis loops for a $(0_2/90_3)_s$ specimen tested under load control
showing ratcheting effect

2.4.3   Strain Control

Strain control tests were performed on a set of $(\pm45/90_3)_s$ multi-ply specimens as
well as on the $(0/\pm25_4/0)_T$, $(0/\pm45_4/0)_T$, and $(0/\pm75_4/0)_T$ constrained angle-ply specimens.
Under strain control, a mean stress relaxation occurs. The reason for this is that as
damage propagates in the specimen, lower loads are required to achieve the same level
of strain. This then results in specimens taking a long time to fail. Figure 2.12 shows
typical hysteresis loops for a strain controlled test.

Strain control was essential for examining crack initiation in the constrained angle
ply composites. In strain controlled tests, the strain acting on each undamaged ply

remains the same. Since the strains in the undamaged plies remain the same, the load

distribution must therefore vary. In a strain control test, the variance between the global

and localized strains is very small. This constrasts with a load controlled test, where the

variance between the local and global loads can be very high. For this reason a strain

controlled test gives a better understanding of the conditions experienced by individual

plies.
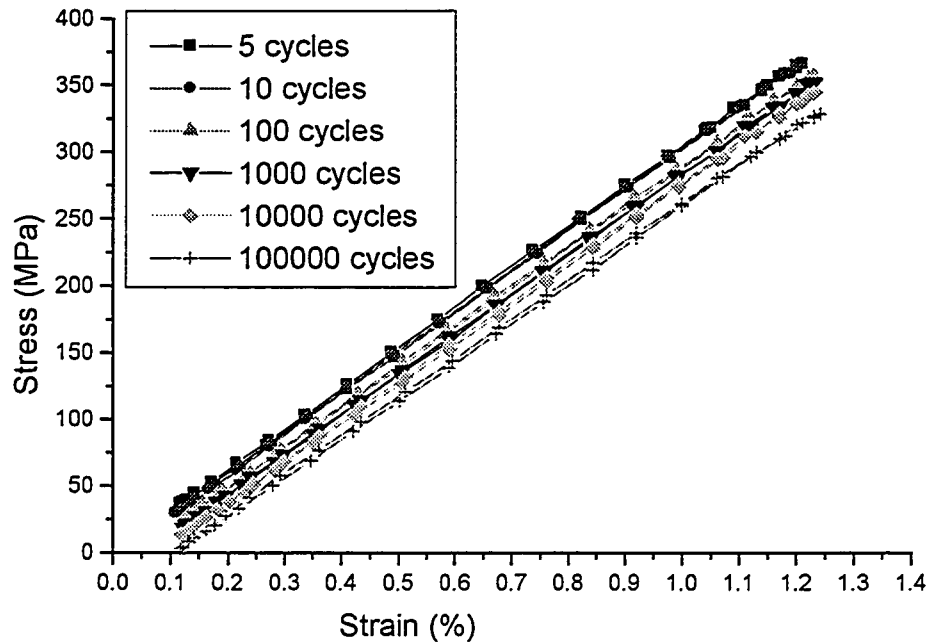
Figure 2.12: Hysteresis loops for $(0/\pm25_4/0)_T$ specimen tested under strain control
showing stress relaxation

Some efforts were made to test $(0_2/90_3)_s$ specimens under strain control at strains

high enough for failure. Unfortunately, as the specimens are cycled, it becomes hard for

the extensometer to remain on the test specimen. Large longitudinal delaminations cause

the extensometer to slip off in these specimens. When the extensometer slips off, the

controlling software sees a large decrease in strain, which is compensated for with a large load increase. This pulls the specimen apart instantaneously. This problem was best resolved by performing the tests on the $(0_2/90_3)_s$ specimens under load control.

2.5   Testing Procedure

To maintain repeatability of the tests, a specific set of procedures were adhered to for all different laminate geometries.

For tests of the $(0_2/90_3)_s$ and $(\pm 45/90_3)_s$ specimens, damage examination consisted of analysis of the hysteresis loops, and visual recording of matrix crack growth. Recordings of the hysteresis loops were taken at regular intervals throughout all tests so as to develop stiffness reduction plots. The image processor was used to determine the crack density throughout the test life. For both the recording of the hysteresis loops and the imaging of the cracks, collection of data was recorded at exponentially decreasing intervals during the life of the specimen. This was done because most of the cracking and stiffness reduction occurs early on, when the primary mode of damage growth is matrix cracking. As damage growth slowed, there was less need for frequent recording of data. To examine the effect of control mode (load control vs. strain control) on the life of the specimen, some tests were performed in both load and strain control modes for the $(\pm 45/90_3)_s$ specimens.

For the constrained angle-ply tests of the $(0/\pm 25_4/0)_T$, $(0/\pm 45_4/0)_T$, and $(0/\pm 75_4/0)_T$ specimens, damage examination was more extensive. Two visual damage detection methods were used in conjunction with analysis of the hysteresis loops. Analysis of the

edge crack growth was done with the aid of visual penetrant and a binocular microscope. The image processor was used to record damage growth through the sides of the specimen. When examining these specimens, the test was momentarily stopped at $5,10,50,100,500$,etc. up to $1x10^6$ cycles. At each stoppage, visual penetrant was applied, an edge crack count was performed, and a video image was captured. All of the constrained angle ply tests were performed under strain control for easier comparison.

2.6 Damage Examination Techniques

Included in this section is a complete listing and explanation of damage examination techniques that were used in this study. The examination techniques varied for different specimen configurations. Early tests of the $(\pm45/90_3)_s$ and $(0_2/90_3)_s$ specimens utilized only the image processor system and stiffness reduction measurements. In the tests of the $(0/\pm25_4/0)_T$, $(0/\pm45_4/0)_T$, and $(0/\pm75_4/0)_T$ specimens damage growth was not easily visible, therefore the microscopic examination method of crack growth, delamination, and crack saturation was used along with of the image processor and stiffness reduction techniques. In addition to the examination methods used herein and described below, a listing of other damage examination techniques is presented in Appendix 1.

2.6.1 Image Processor

Optical imaging consists of using a video camera to digitally capture images of the specimen as it sustains damage at various stages of its life. The method used here

was developed at the University of Alberta by Wolodko, Hoover, and Ellyin [28]. After

the images for a test have been captured, they are analyzed by a computer program to

determine the damage growth. Figure 2.13 illustrates the method by which images of the

damaged coupon specimen are captured.
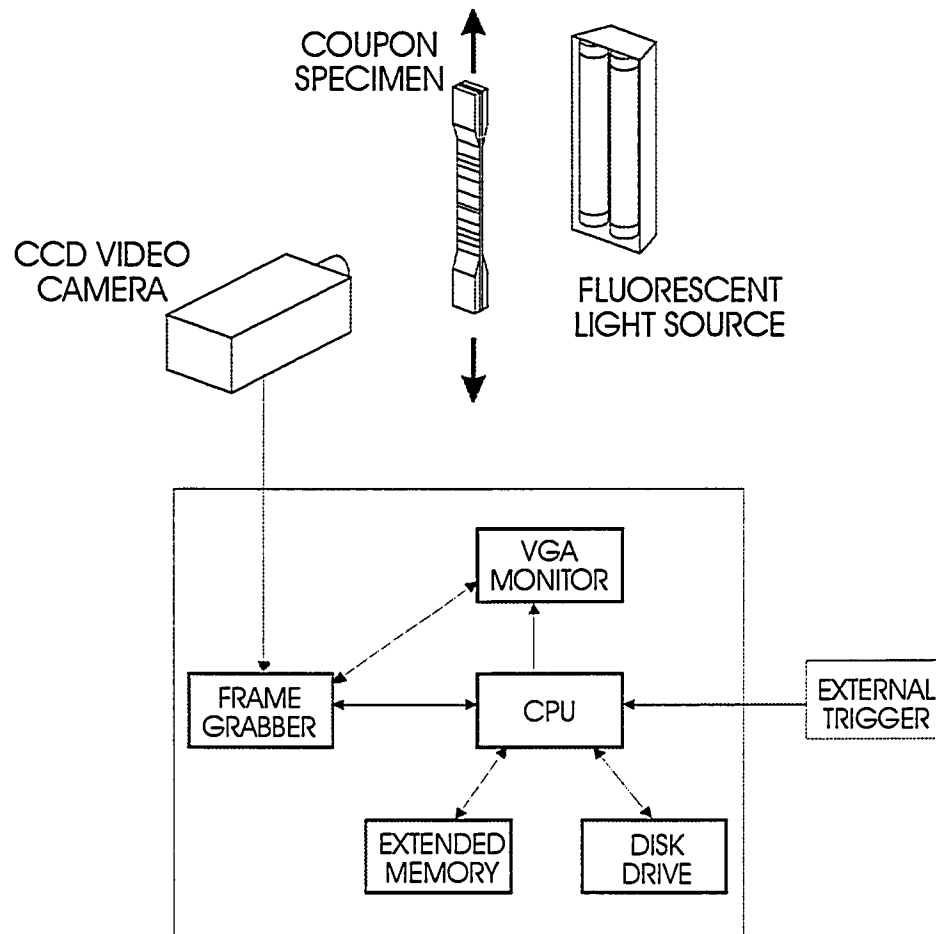
Figure 2.13: Schematic of crack detection apparatus (Courtesy of Wolodko [28])

The optical imaging system operates by first directing a strong light through the semi-transparent composite specimen, and then capturing an image on the opposite side of the specimen using a digital video camera. Any damage in the specimen can be seen as a darker region in the specimen where the damage has reduced the intensity of light that can travel through the composite.

For the $(0_2/90_3)_s$ and $(\pm45/90_3)_s$ specimens, crack growth in the 90° plies is in the form of through-width cracks perpendicular to the direction of loading. Images are analyzed by the computer by summing the intensity of light in bands parallel to the direction of the matrix cracks. Large spikes in the intensity are determined by the program to be matrix cracks. Figure 2.14 illustrates the process that the software employs to determine the transverse crack damage information.
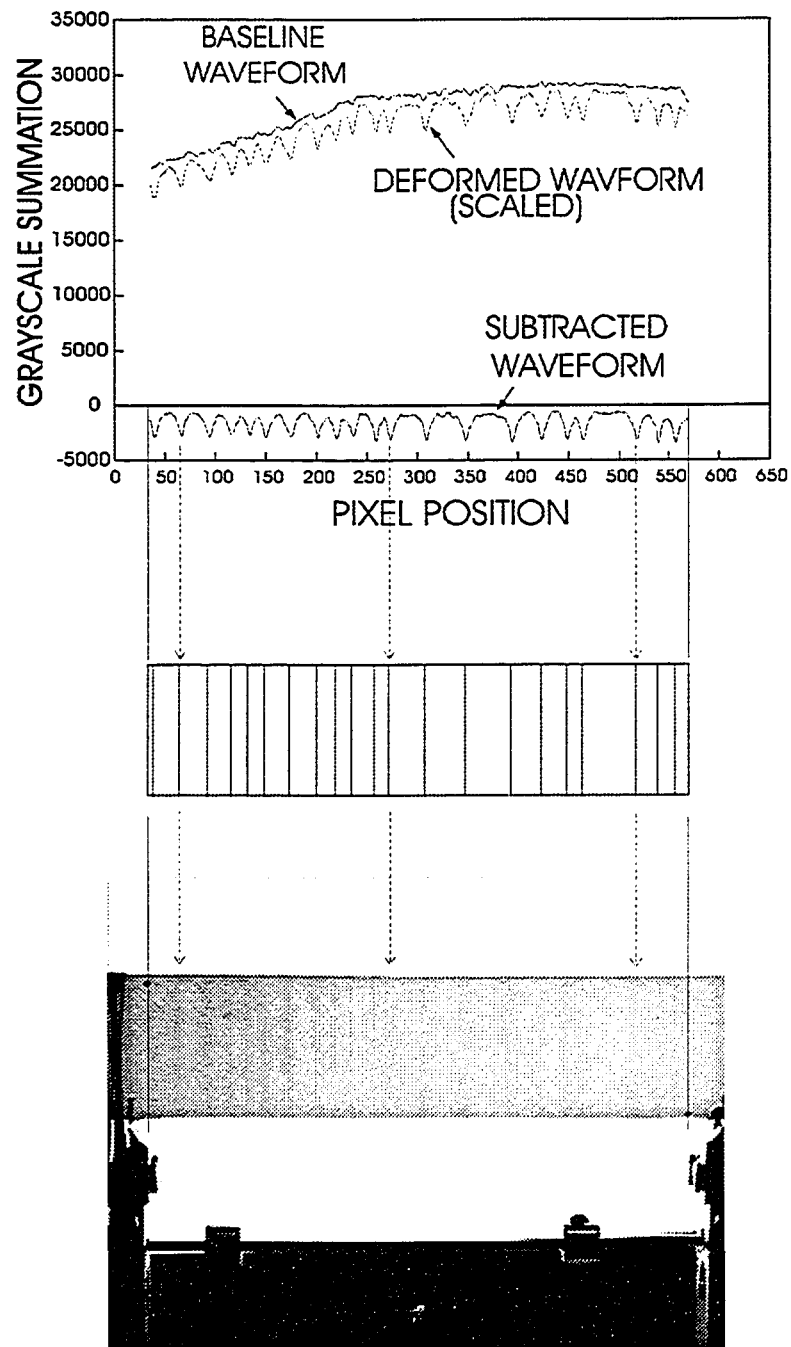
Figure 2.14: Light intensity summation technique for in-situ transverse crack information
(Courtesy of Wolodko [28])

In later angle-ply specimens, such as the $(0/\pm75_4/0)_T$ specimens, the optical imaging system was used to find the saturation state of matrix cracking. Images were recorded throughout the test and then afterward viewed in reverse order until changes in the crack density could be noticed. The image that first showed the entire crack pattern was taken as the point of crack saturation.

2.6.2 Microscopic Edge Examination

The second method of visual damage detection used was an optical binocular microscope. This device proved very useful in determining the point of edge crack initiation, edge crack saturation, and the onset of delamination in the constrained angle ply specimens. Since almost all damage initiates through edge defects in the specimens, this method is very good at determining points of crack initiation. By applying visual dye penetrant to the edge surface of the specimen, contrast in the edge cracks can be enhanced for easier examination. This microscope also had a camera mount that proved useful in documenting damage along the edge of the specimens. Some of the images from this camera are shown later in Chapter 4. The microscope was kept on a set magnification so that the vertical length of the specimen being examined was always 7.5mm in length. This was useful in determining edge crack densities. A picture of the Optical microscope configuration is show below in figure 2.15.
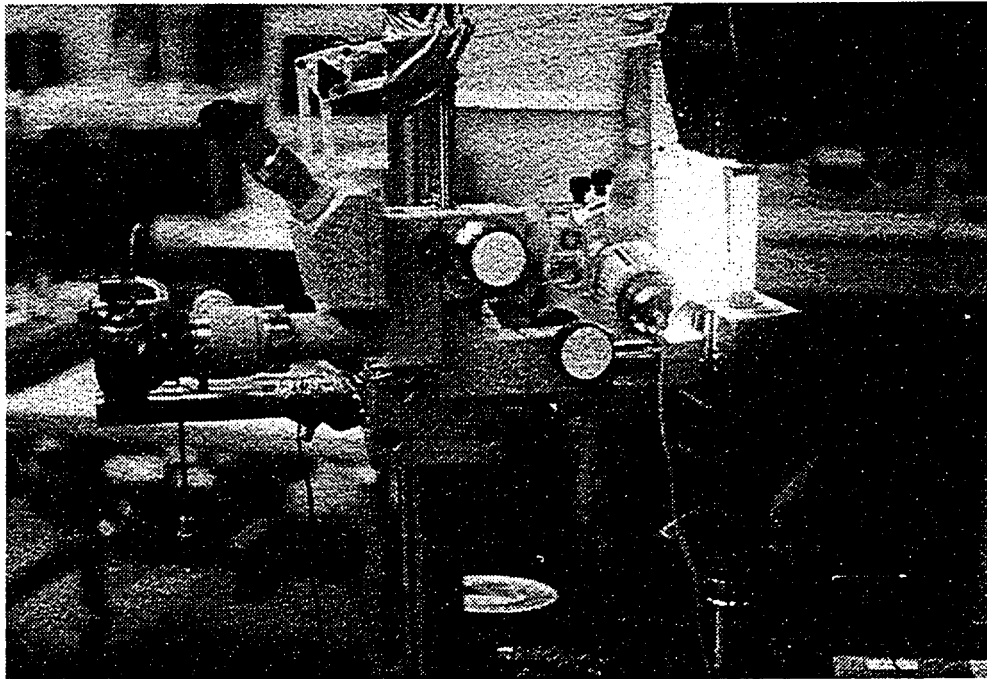
Figure 2.15:   Optical microscope used to examine edge crack growth in composite
laminates

2.6.3   Stiffness Reduction

The measurement of the reduction in stiffness has proved to be a good damage

parameter for cyclic testing of composite specimens [8].   The amount of stiffness

reduction changes depending on the dominant damage mode in a composite.   Stiffness

reduction has also been found to correlate well with matrix crack damage growth.   By

recording the hysteresis loops for individual cycles, and fitting a linear slope to them, an

accurate measurement of the specimen stiffness can be obtained.   Analysis of individual

hysteresis loops for all types of specimens examined showed that the inelastic effects

were small in the specimens.   This made it very easy to determine the stiffness, since the

hysteresis loops were almost linear in shape.

3   Damage Growth During Cyclic Loading of Cross-ply and Multi-ply Coupon Specimens

This chapter has three objectives:

The first is to examine the differences between specimens tested under quasi-static and cyclic loading. By understanding the differences between these, it may be possible to reduce future cyclic testing and use the much simpler method of quasi-static, or even monotonic testing to gain the required information for composite design.

The second objective is to study how damage initiates and propagates in the $(0_2/90_3)_s$ and $(\pm45/90_3)_s$ laminates under cyclic loading. By examining the different damage modes of these specimens, comparisons are made to see how these damage modes differ between the two laminate geometries.

The third objective involves examining differences between tests performed under load control and deformation controlled modes. For this part of the study $(\pm45/90_3)_s$ laminates are tested under both control modes and comparisons are made.

3.1   Summary of Cyclic Tests Performed

Several cyclic tests were performed for the two laminate geometries. Tables 3.1, 3.2, and 3.3 show test data compiled for the various specimens. The tests were divided into groups based on their orientation as well as the control mode (strain or load control).

Table 3.1: ($\pm$45/90$_3$)$_s$ specimens tested under strain control

SPECIMEN: ($\pm$45/90$_3$)$_s$	Loading type : Strain Control
Specimen Number	Maximum Applied Strain
AF-4	0.67%
AF-5	0.30%
AF-6	0.55%
AF-7	0.60%
AF-22	0.33%
AF-24 (I)	0.90 %
AF-33 (I)	1.10 %
AF-34 (I)	1.25 %
AF-35 (I)	0.85 %
AF-41 (I)	0.80 %
AF-178 (I)*	0.80 %
AF-181 (I)*	0.40 %
AF-182 (I)*	0.30 %
* Performed with new software, (I) indicates image processor used.	

Table 3.2: ($\pm$45/90$_3$)$_s$ specimens tested under load control

SPECIMEN: ($\pm$45/90$_3$)$_s$	Loading type: Load Control
Specimen Number	Maximum Applied Load
AF-26 (I)	71.00 MPa
AF-36 (I)	60.00 MPa
AF-43	59.00 MPa
AF-44 (I)	61.00 MPa
AF-45 (I)	55.00 MPa
AF-46 (I)	50.00 MPa
AF-179 (I)*	40.00 MPa
AF-180 (I)*	45.00 MPa
* Performed with new software, (I) indicates image processor used.	

Table 3.3: $(0_2/90_3)_s$ specimens tested under load control.

SPECIMEN: $(0_2/90_3)s$	Loading type: Load Control
Specimen Number	Maximum Applied Load
AF-12 (I)	300 MPa
AF-14 (I)	210 MPa
AF-15	237 MPa
AF-16	257 MPa
AF-19	275 MPa
AF-20 (I)	245 MPa
AF-117	230 MPa
AF-184 (I)*	290 MPa
AF-185 (I)*	240 MPa
AF-186 (I)*	160 MPa
AF-187 (I)*	80 MPa
AF-188 (I)*	90 MPa
AF-189 (I)*	70 MPa
AF-190 (I)*	60 MPa
AF-191 (I)*	50 MPa
* Performed with new software, (I) indicates image processor used.	

3.2   Quasi-Static Test Results

Quasi-static test data was obtained for comparison with cyclic tests. The sources

of this data were: a) tests performed by the author, and b) those from a previous

investigation at the University of Alberta by Hoover [30].   Stiffness and crack density

data was obtained so that crack density vs. specimen stiffness plots could be produced.

Quasi-static tests by the author were performed under strain control on both

$(\pm 45/90_3)_s$ and $(0_2/90_3)_s$ specimens. The test procedure consisted of the following:

Initially the specimen was loaded at a rate of $1 \times 10^{-4} s^{-1}$. Loading ramps started at

0% strain and increased by 0.2% strain for each successive ramp. After loading to the set

strain increment the load was ramped to zero at the same rate, and upon reaching zero an image was captured using the image processor.   A five minute hold time was implemented with the strain at 0% before reloading to the next highest increment.   This procedure was performed until failure of the specimen.

3.2.1   Damage Propagation and Failure of Specimens Under Quasi-Static Loading

For the two types of specimens examined under quasi-static loading $((0_2/90_3)_s$ and $(\pm45/90_3)_s)$, ultimate failure occurred in different ways.   Both specimens experienced a similar initiation of through-width matrix cracking at 0.6% applied strain.   In these quasi-static loading tests, neither specimen type developed a true saturation state of matrix cracks.   Instead, due to the constantly increasing strain, new matrix cracking continued up until the ultimate failure of the specimen.

Delamination growth was different between the $(0_2/90_3)_s$ and $(\pm45/90_3)_s$ specimens.   The $(\pm45/90_3)_s$ specimens first experienced small triangular delaminations at approximately 1.8% applied strain.   These delaminations then continued to grow at a constant rate up until the failure of the specimen.   No delaminations were observed for the $(0_2/90_3)_s$ specimen until very close to ultimate failure of the cross-ply laminate at a strain of approximately 2.1%.   When these delaminations did occur, they were in long strips that were the result of fibre-breakage underneath the tabs of the specimen, and they propagated very quickly along the length of the specimen.

Ultimate failure of the ($\pm45/90_3$)$_s$ specimens took place at an applied strain of 2.33%, whereby the delamination within the 45° plies grew across the width of the specimen

The ($0_2/90_3$)$_s$ laminate has a much different ultimate failure than the ($\pm45/90_3$)$_s$ one. In this specimen, there was very little forewarning of failure. Since the outer constraining plies are oriented in the direction of loading, the fibres sustain most of the load. When some of the 0° fibres fracture, the cross sectional load is redistributed to the other fibres that fail instantaneously under the increased load. The end result is a very quick brush-like failure throughout the entire gauge length of the specimen. Ultimate failure of this specimen occurred at a strain of 2.2%, not long after the initial delaminations were observed.

3.2.2   Quasi-Static Stress-Strain Curves

Stress-strain curves were produced for the quasi-static tests performed and are shown in Figures 3.1 and 3.2. On these plots the light lines under the darkened bold line each represent consecutive loading ramps with increased strain of 0.2%. In both of these figures there is a definite change in the slope of the specimen at approximately 0.6% strain. This change in slope is at the same point of crack initiation in the specimen. This knee-point is indicative of load redistribution to the undamaged constraining plies. These outer plies then undergo larger strains due to the increased load. In both plots, the successive ramps fall into a compressive stress regime near 0% strain. This is due to the

strain control of the tests, whereby after damage has occurred in the specimen, compressive stresses are required to reach 0% strain.

Of interest when comparing the two specimens is the difference in strength of the specimens. The $(0_2/90_3)_s$ specimen has an ultimate failure strength of approximately 350 MPa, while the $(\pm45/90_3)_s$ specimen has an ultimate failure strength of only 100 MPa. The difference between these two specimens again lies in the constraining plies. The $0°$ plies with the fibres oriented in the direction of loading produce the maximum strength and stiffness possible. On the other hand, in the $(\pm45/90_3)_s$ specimens, the constraining plies are oriented at $45°$ to the direction of loading, and they rely heavily on the matrix component for the strength characteristics.
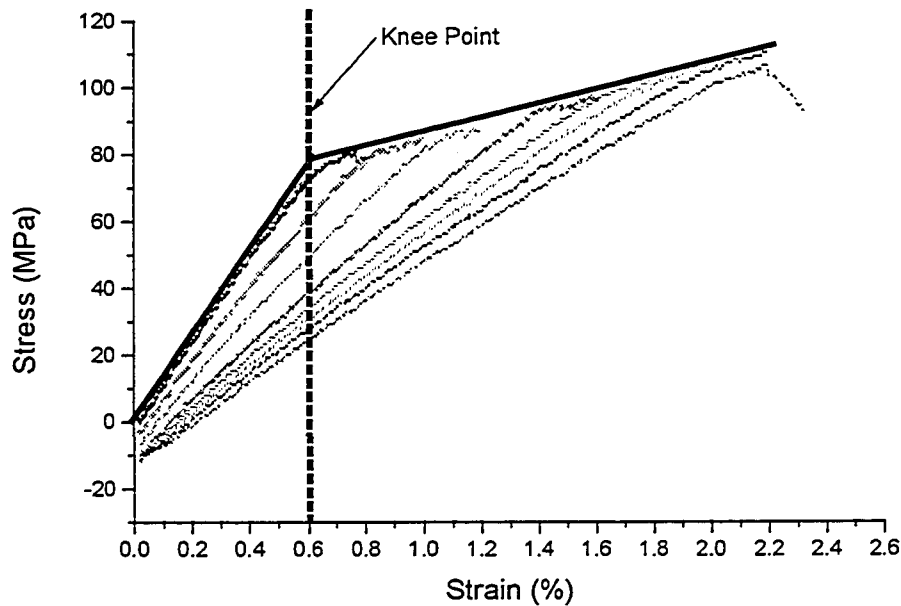
Figure 3.1: Stress-strain curve for $(\pm45/90_3)_s$ specimen loaded quasi-statically under strain control (Each line represents a subsequent loading ramp)
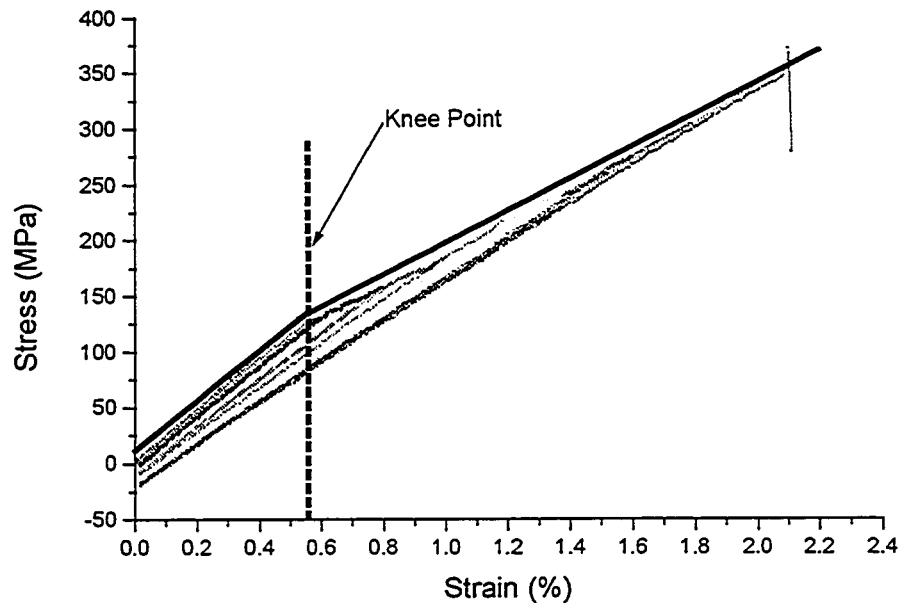
Figure 3.2: Stress-strain curve for $(0_2/90_3)_s$ specimen loaded quasi-statically under strain
control (Each line represents a subsequent loading ramp)

3.2.3 Crack Density Curves

Crack density vs. strain curves were produced for both specimen types examined

and are shown in Figure 3.3. Crack initiation for both orientations was at 0.6% strain, the

same strain where large stiffness reductions were first seen. Both types of specimens

followed similar crack density curves throughout their lives, although the $(0_2/90_3)_s$

specimen produced slightly more cracks as the strain increased. This is due to larger

stress gradients between the 0° plies and the 90° plies than that seen between the 45°

plies and the 90° plies, resulting in more load transfer and more matrix cracking.
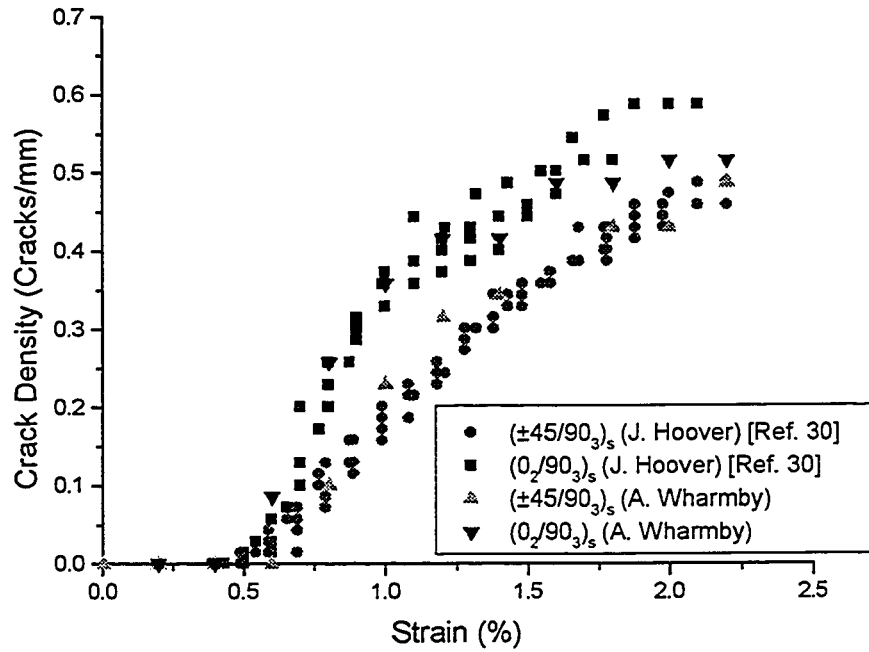
Figure 3.3:   Crack density vs. strain for (±45/90₃)ₛ and (0₂/90₃)ₛ specimens under quasi-static strain controlled loading (Courtesy of Hoover [30])

3.2.4   Crack Density vs. Stiffness Curves

Crack density vs. stiffness curves were produced for the quasi-static tests and are shown in Figure 3.4. By plotting both the (±45/90₃)ₛ and (0₂/90₃)ₛ curves on the same figure, their slopes can be compared.

The slopes of both specimen geometries were found by fitting linear curves to the test data. For the (0₂/90₃)ₛ specimens, the slope was –9.21 GPa/(crack/mm). For the (±45/90₃)ₛ specimens, the slope was –11.62 GPa/(crack/mm). These are quite close, although there is more change in slope for the matrix dominated specimen. This is due to two possible effects that occur in the (±45/90₃)ₛ, but not in the (0₂/90₃)ₛ specimens. The

first effect is increased stiffness reduction due to visco-elasticity in the constraining ply

matrix in the ($\pm45/90_3$)$_s$ specimens. The second reason for the larger stiffness drop could

be that there is extra matrix cracking in the constraining plies of the ($\pm45/90_3$)$_s$ specimens

which is not accounted for in the crack density measurements.
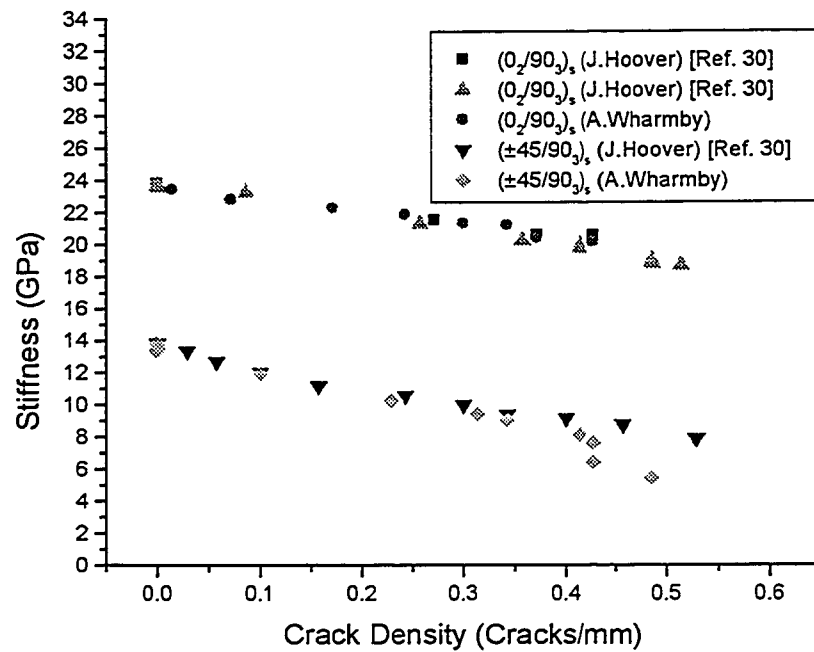
Figure 3.4: Stiffness reduction vs. crack density for ($0_2/90_3$)$_s$ and ($\pm45/90_3$)$_s$ coupon
specimens under quasi-static loading

3.3   Cyclic Test Results

3.3.1   Description of Damage Growth and Specimen Failure under Cyclic Loading

Failure of specimens under cyclic loading had some distinct differences from that of quasi-static loading. A number of extra factors are present in the cyclic tests including frequency, R-ratio, the number of cycles a specimen undergoes, as well as any effects of the cyclic waveform.

Presented in this section are consecutive images of typical specimens as damage initiates and propagates through them over their cyclic life. In these figures the life of the specimen was normalized with respect to the number of cycles at failure. When normalized in this manner, specimens of the same geometry have comparable damage growth at these points in the specimens life irrespective of the loading level, so these figures can be assumed to be general. The damage growth with respect to the normalized data will be discussed further in 3.3.3 and 3.3.4.

The systematic damage growth and failure of an $(0_2/90_3)_s$ specimen subjected to cyclic loading is outlined in the Figures 3.5 and 3.6. These show the damage growth in specimen AF-14, which underwent a maximum applied load of 210 MPa.

The first damage mode seen was matrix cracking which appear in the 90° layers as dark vertical bands. These matrix cracks occur very early in the overall life of the specimen (earlier than $N/Nf = 0.0006$). They immediately propagate through the width. Very little, if any, partial cracking can be seen with this type of specimen lay-up. Cracking continues until a saturation state of matrix cracks is achieved. Near the

saturation state a new damage mode begins. Matrix cracks propagate to the constraining plies where they grow perpendicular to the original crack direction, along the lengths of the 0° fibres. These are termed longitudinal matrix cracks, and are first seen at N/Nf = 0.006 in the form of dark horizontal lines. When damage growth in this form is nearly exhausted, the damage mode changes once again. From these longitudinal matrix cracks, and from the edges of the specimen, delaminations grow (First seen at N/Nf=0.012). These delaminations grow in long lengthwise strips. They slowly progress inwards until there is almost complete separation between the 0° and 90° plies. This damage mode comprises the largest portion of the specimen life. The damage mode doesn't change again until N/Nf=0.98, when fibre failure becomes the dominant damage mode. A quick and instantaneous failure of the specimen follows soon thereafter.
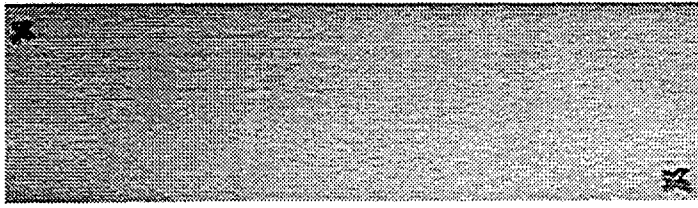
N/Nf=0
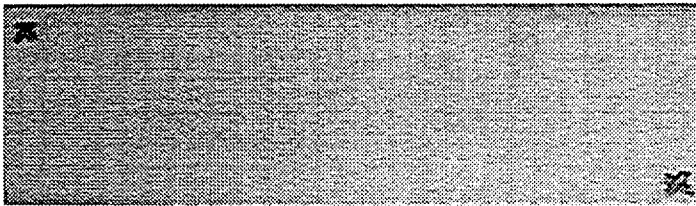
N/Nf=0.0006
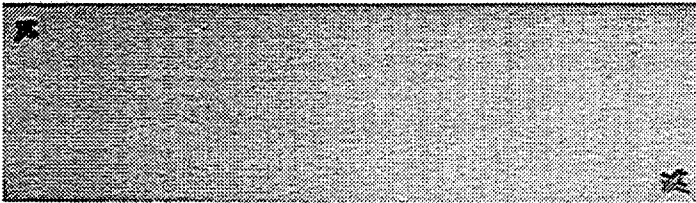
N/Nf=0.0012

N/Nf=0.006
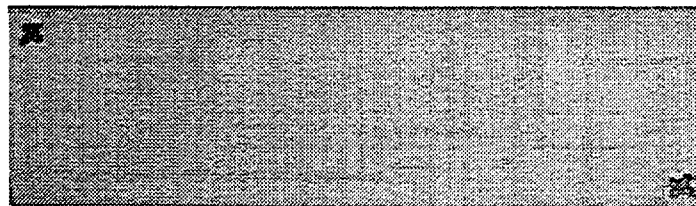
N/Nf=0.012

Figure 3.5: Damage progression of a typical $(0_2/90_3)_s$ composite laminate, cycles 0 through 10,000
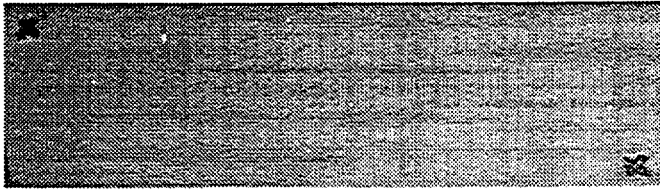
N/Nf=0.12
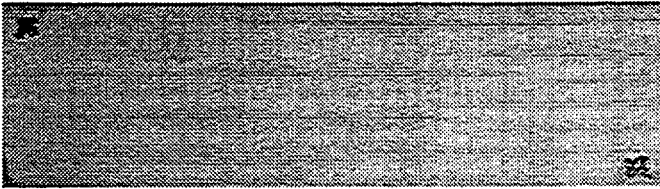
N/Nf=0.35
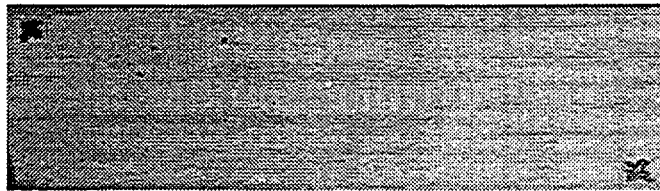
N/Nf=0.75
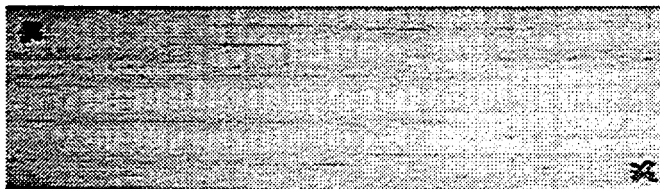
N/Nf=0.98

Failed Specimen
at N/Nf=1.0

Figure 3.6: Damage progression of a typical $(0_2/90_3)_s$ composite laminate, cycles
100,000 through to failure at 865,000 cycles

A different damage growth is described below for the $(\pm 45/90_3)_s$ specimens.

Figured 3.7 and 3.8 show the damage progression throughout the fatigue life of a $(\pm 45/90_3)_s$ specimen. This is specimen AF-36, with a maximum applied load of 60 MPa. In the $(\pm 45/90_3)_s$ specimen the crack initiation is at $N/Nf=0.012$. Initially the matrix cracking in the $(\pm 45/90_3)_s$ specimen follows the same pattern as the $(0_2/90_3)_s$ specimen. Differences begin only when the damage propagates into the constraining plies of the specimen. In the $(\pm 45/90_3)_s$ specimens, matrix cracking is seen in the constraining plies at $45°$ angles from the direction of loading. This constraining ply matrix cracking is first seen at $N/Nf = 0.06$, and is mostly present where transverse cracks from the $90°$ layers have propagated into the constraining plies. These cracks begin as small partial cracks and propagate until they span the length of the $45°$ fibres.

Differences are apparent between the cracks in the $90°$ layers and those in the $45°$ layers. The $45°$ layer cracks start out as partial cracks, and appear to have a higher crack density. Previous work had found that when the thickness of the similarly oriented plies decreases, the crack density in that section increases, and more partial cracks appear [21]. In Figure 3.8, delaminations can be seen to propagate and grow near the point of matrix crack saturation. These small triangular delaminations begin at approximately $N/Nf=0.29$. They initiate in the $45°$ layers at the outer edges where the localized strain is the greatest. While delaminations propagate longitudinally in the $(0_2/90_3)_s$ specimens, in the $(\pm 45/90_3)_s$ specimens they grow at $45°$ angles from the edges. This delamination growth along the direction of the $45°$ layers continues until it is across the width of the

specimen.   At N/Nf=0.98 the triangular delaminations have grown across half of the width of the specimen.   The remaining delamination growth occurs in the last 2% of the specimens life.   When the delamination has spread across the entire width, only the matrix in the 45° layers holds the specimen together, and this matrix fails under shear loading parallel to the fibres.   Ultimate failure in this specimen is dominated by the strength of the matrix, as is seen when N/Nf = 1.0.   There is no fibre failure present in this final failed state.

Visual differences in damage growth between the two specimens are most apparent in the constraining plies.   It is here that the different fibre orientations produce the distinct delamination and ultimate failure patterns for each specimen.
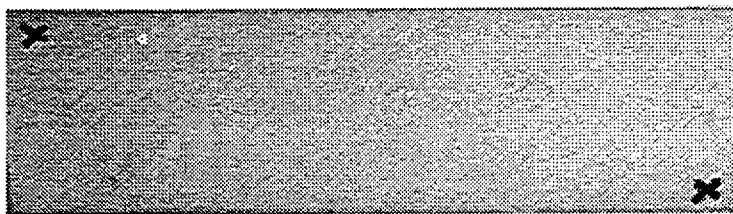
N/Nf=0
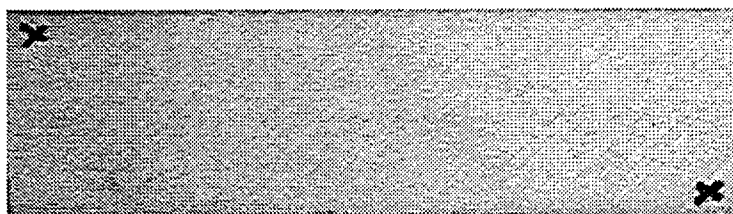
N/Nf=0.006
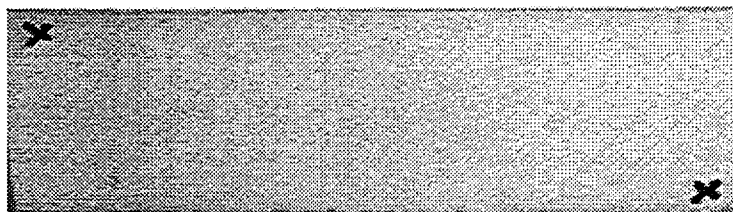
N/Nf=0.012
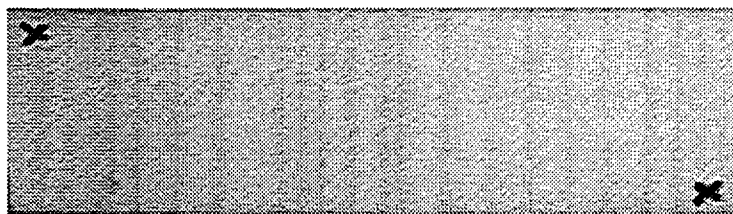
N/Nf=0.06
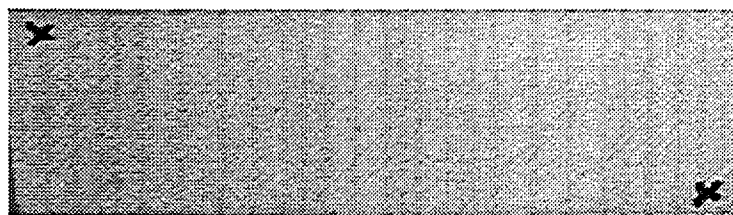
N/Nf=0.12

Figure 3.7: Damage progression of a typical $(\pm 45/90_3)_s$ composite laminate, cycles 0 through to 10,000 cycles
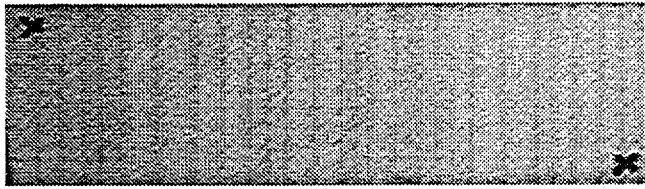
N/Nf=0.29
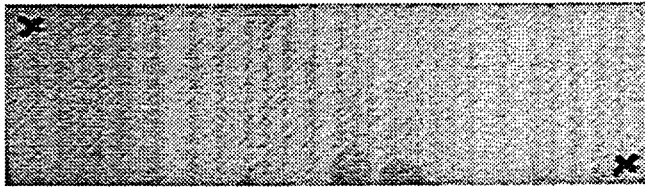
N/Nf=0.59
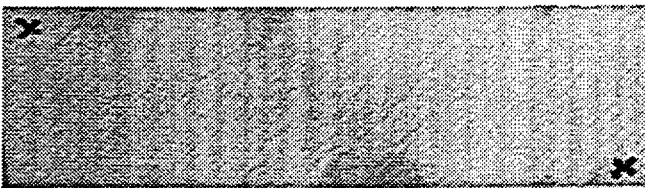
N/Nf=0.88
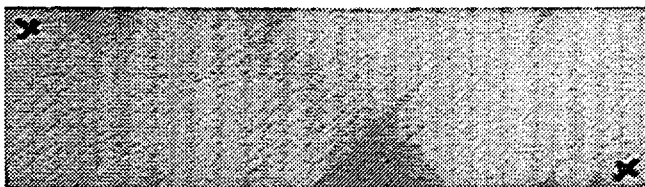
N/Nf=0.98
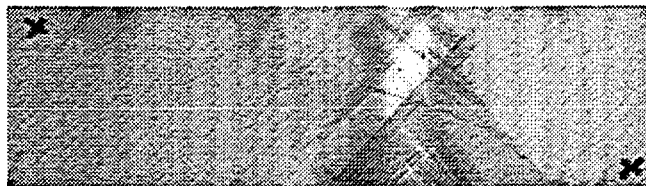
Failed Specimen
at N/Nf=1.0

Figure 3.8: Damage progression of a typical (±45/90₃)ₛ composite laminate, cycles
25,000 through to failure at 84,900 cycles

3.3.2 Damage Mode Curves

Damage mode curves were produced for the $(\pm 45/90_3)_s$ specimens under strain control and for the $(\pm 45/90_3)_s$ and $(0_2/90_3)_s$ specimens under load control. ε-N curves for the $(\pm 45/90_3)_s$ specimens are shown in Figure 3.9. S-N curves for the $(\pm 45/90_3)_s$ and $(0_2/90_3)_s$ specimens are shown in Figures 3.10 and 3.11, respectively. In all cases, points for crack initiation, the onset of delamination, and ultimate failure of the specimen were recorded.

Figure 3.9 shows the damage mode curves for the $(\pm 45/90_3)_s$ specimens under strain control in which the maximum applied strain is plotted against the log of the number of cycles. All of the damage modes appear to follow fairly linear lines in the range of the applied strains.
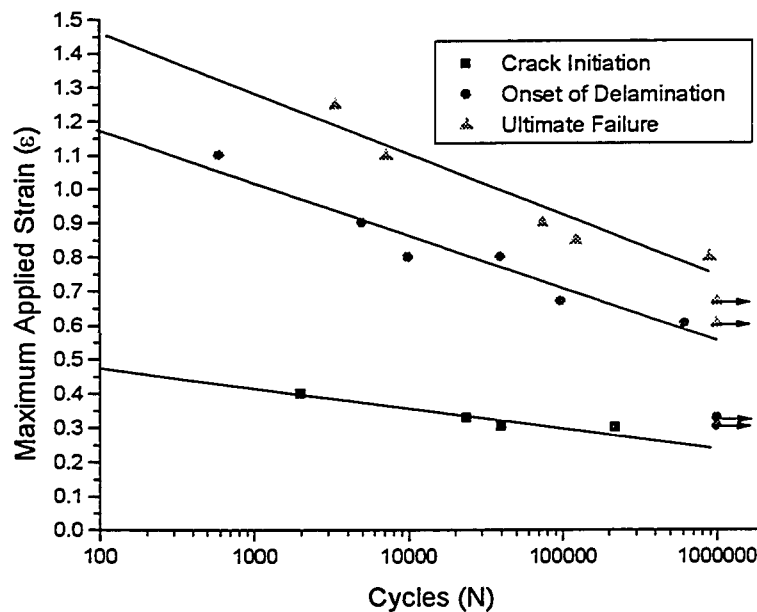
Figure 3.9: ε-N Curve for $(\pm 45/90_3)_s$ composite coupon specimens under strain control

Figure 3.10 shows the damage mode curves for the $(\pm45/90_3)_s$ specimens tested under load control. The curves follow a similar trend as those under the strain control (Fig. 3.9). The $(\pm45/90_3)_s$ specimens tested under load control had the shortest lives of all specimens examined. At a maximum applied stress of 40 MPa, crack initiation was not observed prior to 1×10^6 cycles. This may indicate a possible crack initiation stress limit between 40 and 45 MPa. However, to verify this hypothesis, several long term tests need to be performed. This was beyond the scope of this study.
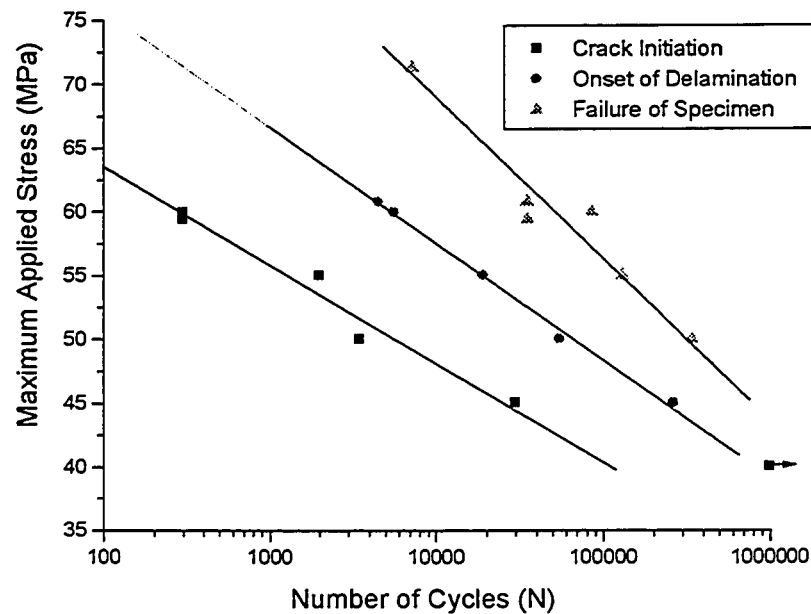
Figure 3.10: S-N fatigue curve for $(\pm45/90_3)_s$ specimens under load control

The damage curves for the $(0_2/90_3)_s$ specimens under load control are displayed in Figures 3.11 and 3.12. In the case of the $(0_2/90_3)_s$ specimens, the range in life between the onset of cracking and ultimate failure of the specimen is very wide. This is because the matrix in the 90° layers is very weak in relation to the fibres in the 0° layers.

Specimens which developed crack initiation points, such as those shown in Figure 3.12, required much more than 1×10^6 cycles to reach ultimate failure. For this reason two sets of specimens were tested, one set for the initiation of cracking in the 90° layers, and the other set to obtain points for the remaining damage modes. Compared with the applied loads to fail the $(\pm45/90_3)_s$ specimens, the $(0_2/90_3)_s$ specimens loads were much higher. The loads required for cracks to initiate were also higher. This is because the 0° constraining plies contribute to a higher global stiffness, so that for a prescribed strain, a larger load would be required.

Of note in Figure 3.12 is a point that does not fall on the crack initiation curve. This is similar to that observed in Figure 3.10 and may be attributed to the existence of a crack initiation stress limit.
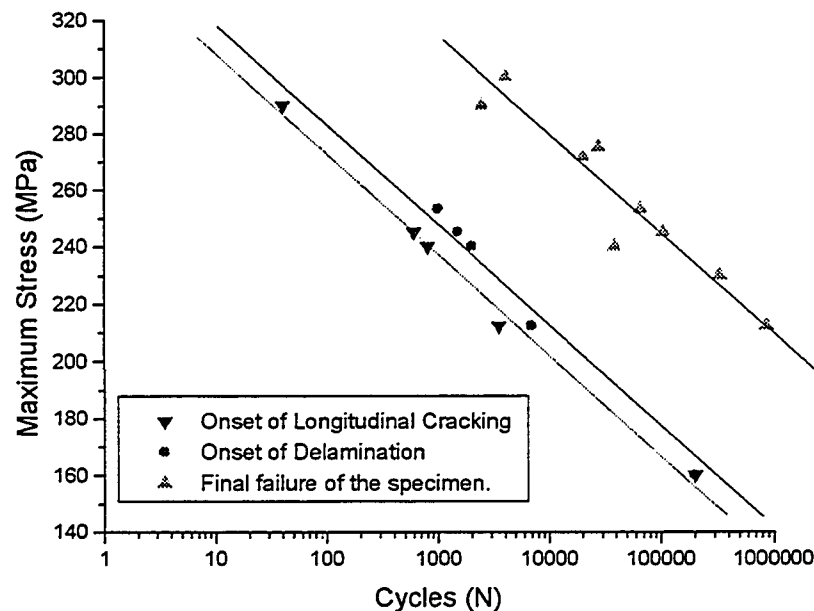
Figure 3.11: S-N fatigue curve for $(0_2/90_3)_s$ composite coupon specimens under load control
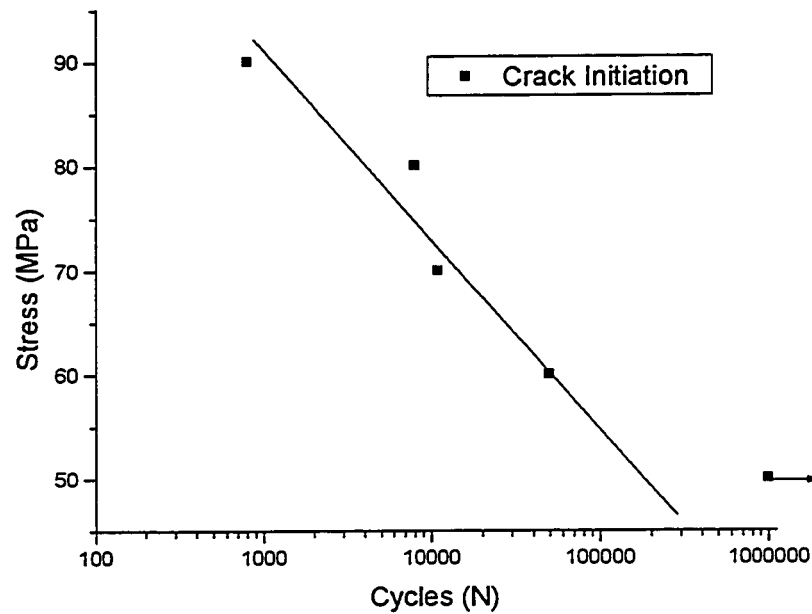
Figure 3.12: S-N fatigue curve for crack initiation in $(0_2/90_3)_s$ composite coupon specimens under load control

A check was performed to see how reliable were the crack initiation curves shown in Figures 3.9, 3.10 and 3.12. Since there is virtually no change in the global specimen stiffness prior to crack initiation, the strains at which cracking initiates should be similar irrespective of the imposed control mode (strain or load control). For tests performed under load control, the maximum strain at the crack initiation was determined by using a stiffness value found from the classical laminate theory calculations. A plot of the maximum strain vs. cycles for crack initiation is shown in Figure 3.13. There is a clear band of ±0.06% strain that all specimens fall within. This then confirms the accuracy of the crack initiation data plotted in Figures 3.9, 3.10, and 3.12.
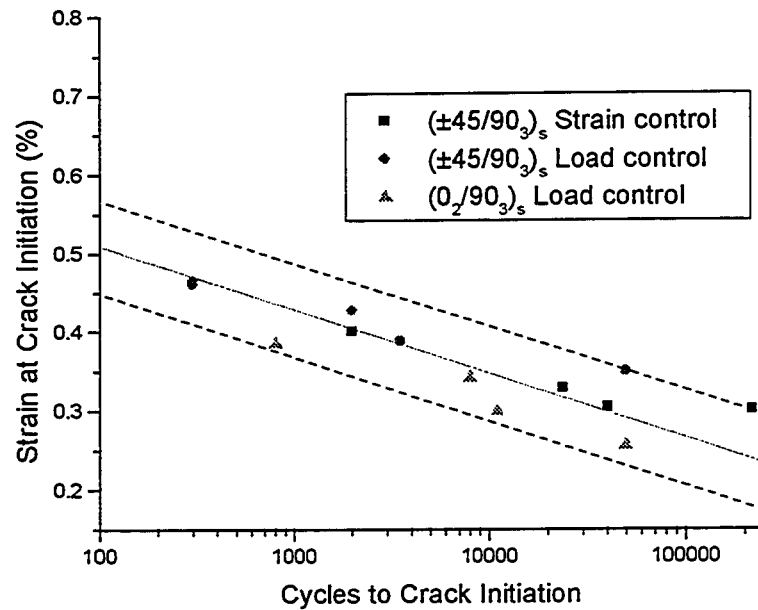
Figure 3.13: Strain vs. crack initiation for cross-ply and multi-ply specimens investigated

3.3.3   Damage Examination Technique I: Crack Density Curves

Crack density vs. life curves were produced for the three scenarios examined. Data was plotted in two forms: the first was crack density vs. cycles, and the second was crack density vs. the normalized cycles. In the second plot the cycles were normalized with the cycles to failure to examine how well all test data correlated. In some cases logarithmic plots were produced for easier investigation of damage growth near the start of the test. In all cases, the 90° matrix crack data was recorded using the image processor described in Chapter 2, section 2.6.1.

Crack density vs. life curves are presented in Figures 3.14-3.15, 3.16-3.18, and 3.19-3.20 for the $(\pm 45/90_3)_s$ specimens under strain control, $(\pm 45/90_3)_s$ specimens under load control, and the $(0_2/90_3)_s$ specimens under load control, respectively.

A table was developed outlining some of the interesting points from these figures, and are presented in Table 3.4:

Table 3.4: Details of crack density figures for the three scenarios examined

SPECIMEN	FINAL CRACK DENSITY (CRACKS/MM)	SATURATION STATE REACHED?	CRACK ONSET DELAY SEEN
$(\pm 45/90_3)_s$ Strain Control	0.45	YES	NO
$(\pm 45/90_3)_s$ Load Control	0.35-0.48	NO	YES (~1% of life)
$(0_2/90_3)_s$ Load Control	0.65	YES	NO

The final crack densities for all specimens were seen to vary with the laminate orientation. Higher crack densities were seen in the $(0_2/90_3)_s$ specimens due to higher interlaminar stresses present between the 0° plies and the 90° plies than is present between the 45° plies and 90° plies. A higher stress gradient in the $(0_2/90_3)_s$ specimens results in more load transfer. This then results in a higher crack density.

In these specimens a level of transverse crack saturation is seen in the $(\pm 45/90_3)_s$ specimens under strain control, and in the $(0_2/90_3)_s$ specimens under load control, similar to what was seen by other researchers [8]. In the $(\pm 45/90_3)_s$ specimens this is due to stress relaxation as the test progresses. As damage propagates, the same strain produces a smaller load , resulting in less new damage growth. Finally, at some point in the life of

the specimen the stress relaxes sufficiently so that no new damage growth takes place. In the $(0_2/90_3)_s$ specimens tested under load control, the strain required to reach the desired maximum loads in the constraining plies was fully elastic, so the overall strain that the specimen underwent throughout the test remained fairly constant, resulting in a saturation state of matrix cracks.

In the $(\pm45/90_3)_s$ specimens under load control the final crack density varied between 0.35 and 0.475 cracks/mm. No saturation state of cracking was observed. The strain in the constraining plies of these specimens constantly increases due to the ratcheting effect. This causes the crack density to increase up until the point of ultimate failure, resulting in no distinguishable saturation state.

A crack onset delay was seen in the $(\pm45/90_3)_s$ specimens under load control and are seen as the points before any crack growth in Figure 3.17. The crack onset delay for this specimen was approximately 1% of the specimen life. This onset delay is a result of the loading scenario, whereby the load control test constantly increases the strain as new damage grows. In this initial region, visco-plastic effects and microdamage may be leading to increases in strain, which eventually result in matrix crack growth. This crack onset delay is most likely present in the $(0_2/90_3)_s$ specimens tested under load control as well, although it is hard to detect. In these specimens the large differences in load capacity between the inner plies and constraining plies lead to matrix cracking occurring very early compared to the life of the constraining plies. This makes the crack onset delay a very small part of the overall specimen life, much less than 1%.

Other interesting findings from these figures was that for higher loads and strains, damage growth took fewer cycles. The initial slope of crack growth was steeper for specimens with larger loads and strains.

By normalizing the lives of the specimens, as shown in Figures 3.15, 3.17, 3.18, and 3.20, it could be seen that a correlation between crack densities at different loading levels occurred in the specimens which achieved a saturation state of matrix cracking. The data was more scattered for the $(\pm45/90_3)_s$ specimens under load control, where no saturation state was reached.
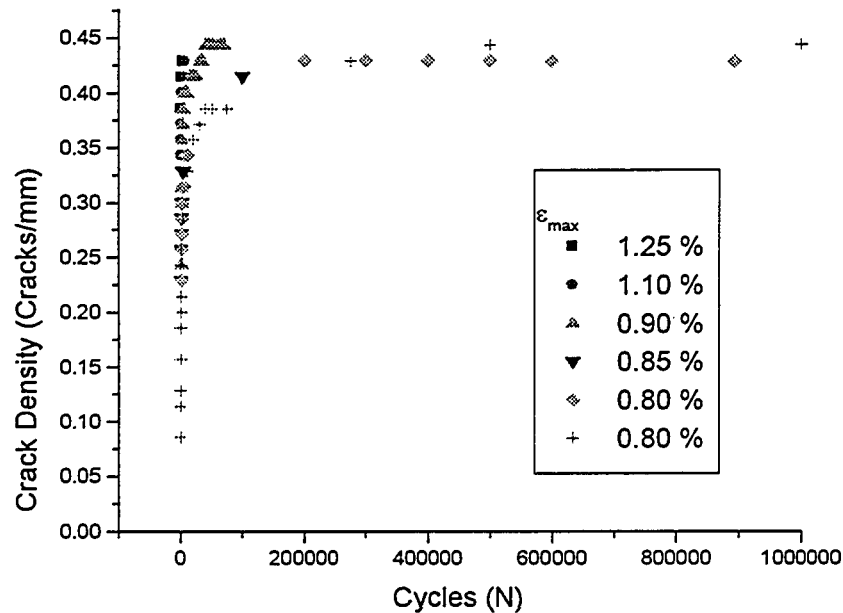
Figure 3.14: Crack density vs. cycles (linear scale) for $(\pm45/90_3)_s$ specimens under strain control, showing a saturated state of matrix cracking
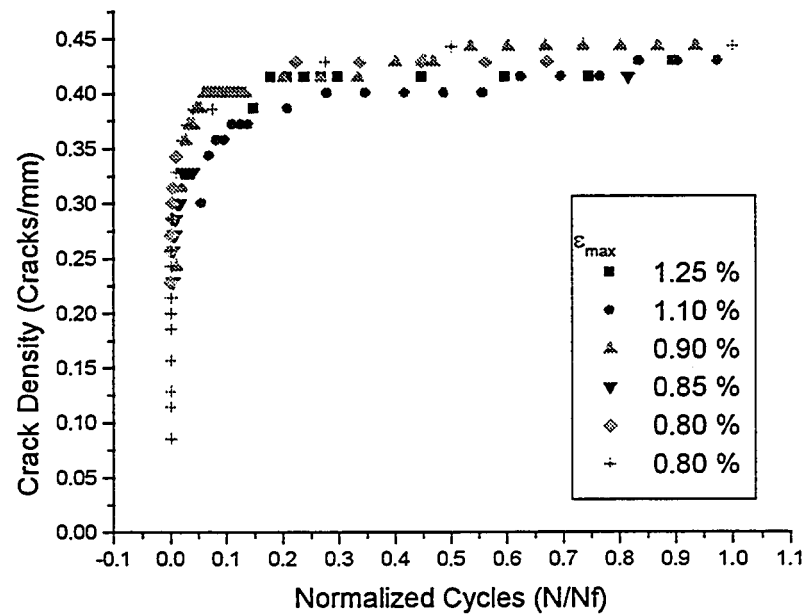
Figure 3.15: Crack density vs. normalized cycles (linear scale) for (±45/90₃)ₛ specimens under strain control
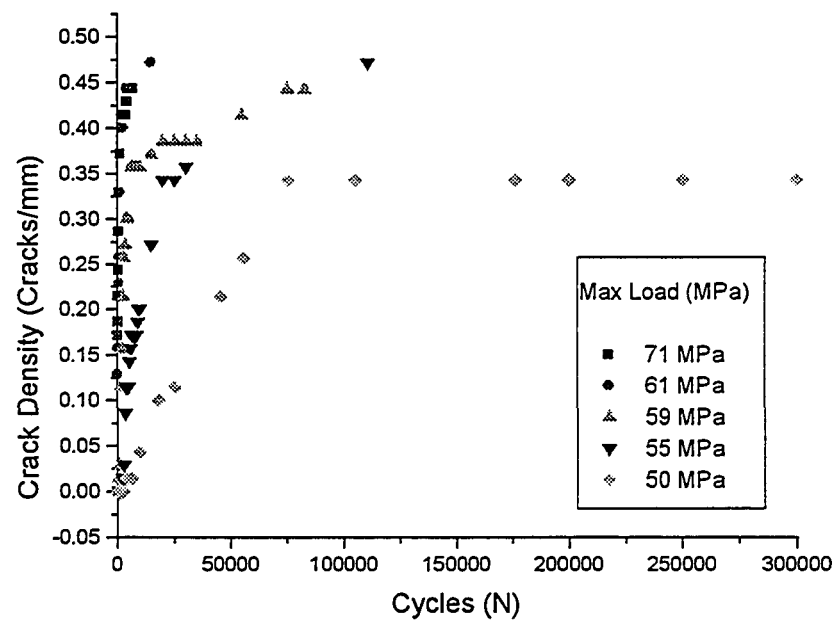
Figure 3.16: Crack density vs. cycles (linear scale) for (±45/90₃)ₛ specimens under load control
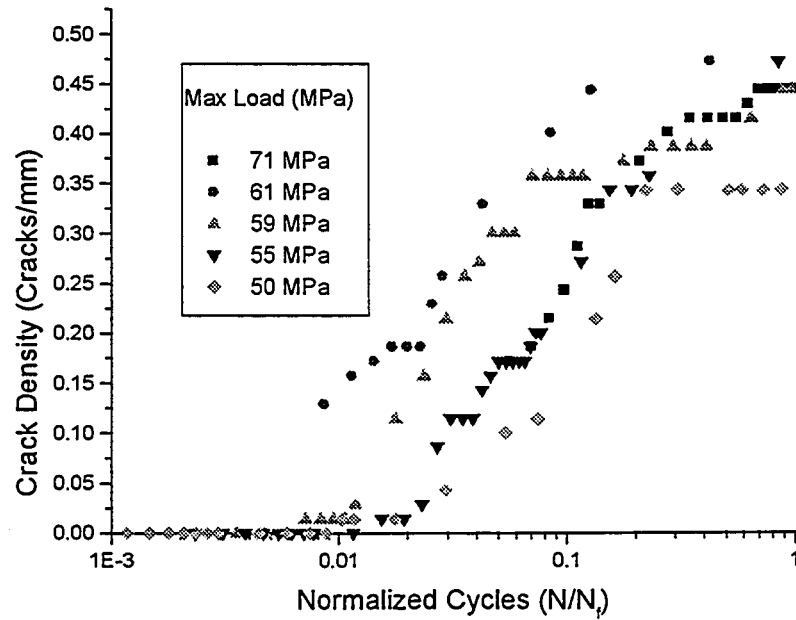
Figure 3.17: Crack density vs. normalized cycles (log scale) for $(\pm45/90_3)_s$ specimens
under load control
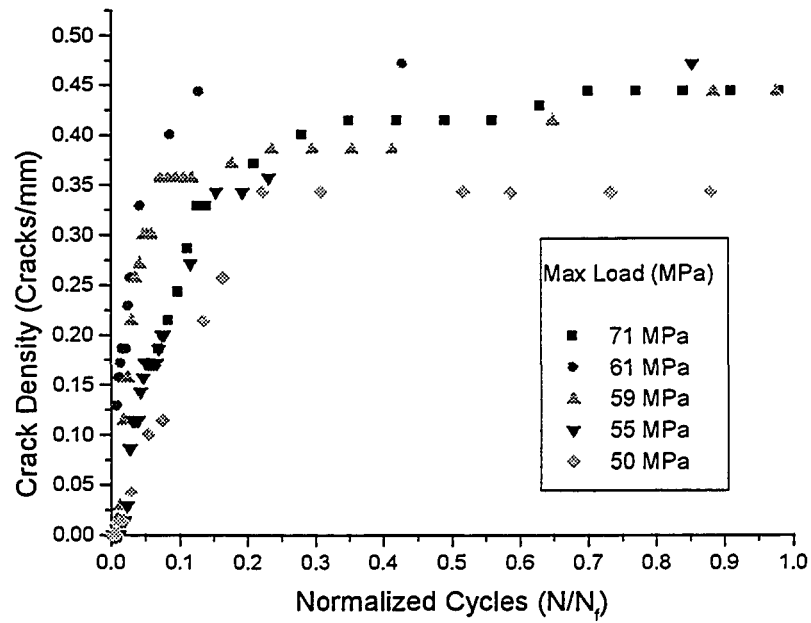
Figure 3.18: Crack density vs. normalized cycles (linear scale) for $(\pm45/90_3)_s$ specimens
under load control
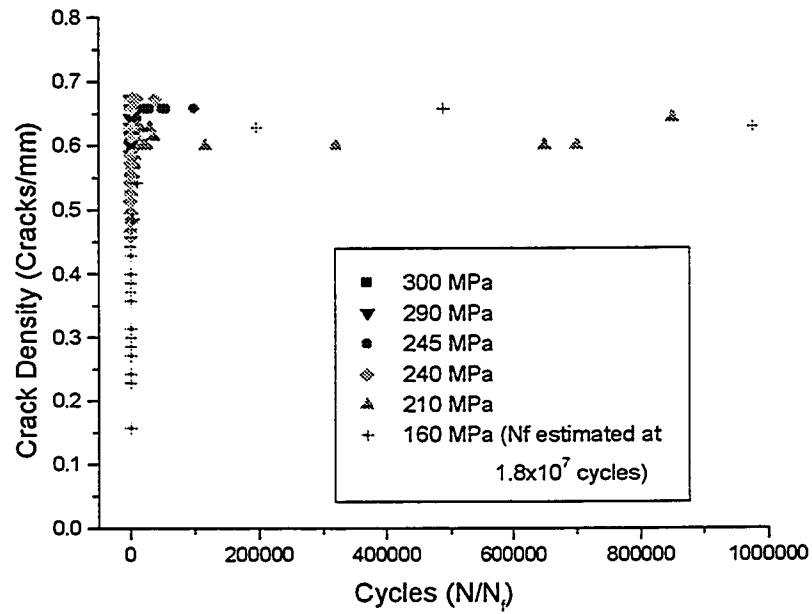
Figure 3.19: Crack density vs. number of cycles (linear scale) for $(O_2/90_3)_s$ specimens
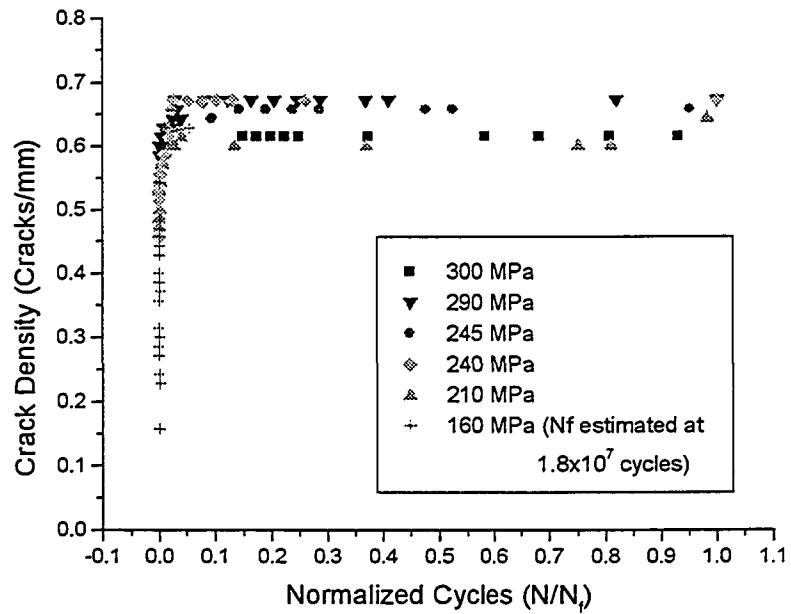
Figure 3.20: Crack density vs. normalized cycles (linear scale) for $(O_2/90_3)_s$ specimens

3.3.4   Damage Examination Technique II: Stiffness Reduction Curves

For all of the cyclic tests performed, stiffness measurements were determined from the stress-strain hysteresis loops of the specimens. These stiffness measurements were used to produce stiffness reduction curves of similar fashion to the crack density curves produced in the previous section. The stiffness reduction data is presented in two forms. In the first form, the data is plotted against the cycles on both linear and logarithmic plots. In the second form, plots are normalized with respect to the initial stiffness (E/Eo), and the failure cycles of the specimen (N/N$_f$). Figures 3.21-3.22, 3.23-3.25, and 3.26-3.27 show the stiffness reduction plots for the ($\pm$45/90$_3$)$_s$ specimens under strain control, the ($\pm$45/90$_3$)$_s$ specimens under load control, and the (0$_2$/90$_3$)$_s$ specimens under load control respectively.

Similar to the last section, a table was developed to outline the interesting differences between the specimens examined:

Table 3.5: Details of stiffness reduction figures for the three scenarios examined

SPECIMEN	STIFFNESS REDUCTION			
	TOTAL (GPA)	TOTAL (%)	DUE TO MATRIX CRACKING. (GPA)	DUE TO DELAMINATION (GPA)
($\pm$45/90$_3$)$_s$ (S.C)	8	58	6	2
($\pm$45/90$_3$)$_s$ (L.C)	7-10	50-65	5-8	2-3
(0$_2$/90$_3$)$_s$ (L.C)	6	20	6	Negligible

All of the plots show that there are two distinct sections of stiffness reduction. The first section is quite steep, and is the result of matrix cracking. The second section follows a flatter slope and is the result of stiffness reduction due to delamination. The

($\pm45/90_3$)$_s$ specimens experienced a much larger stiffness reduction from delamination due to the orientation of the constraining plies. As delamination grew through these 45° plies, less of the cross-section took up the load, resulting in increased strain and reduced stiffness. In the ($0_2/90_3$)$_s$ specimens there is negligible stiffness reduction due to delamination, although it is largely present as shown in Figures 3.5 and 3.6. In this laminate the 0° fibre angle prevents any increase in strain in the constraining plies over the life. This results in little stiffness reduction after the saturation state is reached, even though delamination occurs.

Stiffness reduction curves matched up well with crack density data examined in section 3.3.3. When the data was normalized with respect to the specimen life, all loading magnitudes followed similar curves for the ($\pm45/90_3$)$_s$ specimens under strain control and the ($0_2/90_3$)$_s$ specimens under load control. More scatter in stiffness reduction was seen for the ($\pm45/90_3$)$_s$ specimens under load control, which matched with findings in the crack density plots. The ($\pm45/90_3$)$_s$ specimens under load control had a stiffness reduction onset delay of approximately 1% of the specimens life, as shown in Figure 3.25, similar to the crack onset delay seen earlier for the same specimen.

Although ($0_2/90_3$)$_s$ laminates undergo a stiffness reduction of similar magnitude to the ($\pm45/90_3$)$_s$ specimens, the decrease relative to the total stiffness is only 20%. This is due to the much higher global stiffness of these specimens because of the fibres in the constraining plies being oriented in the loading direction.
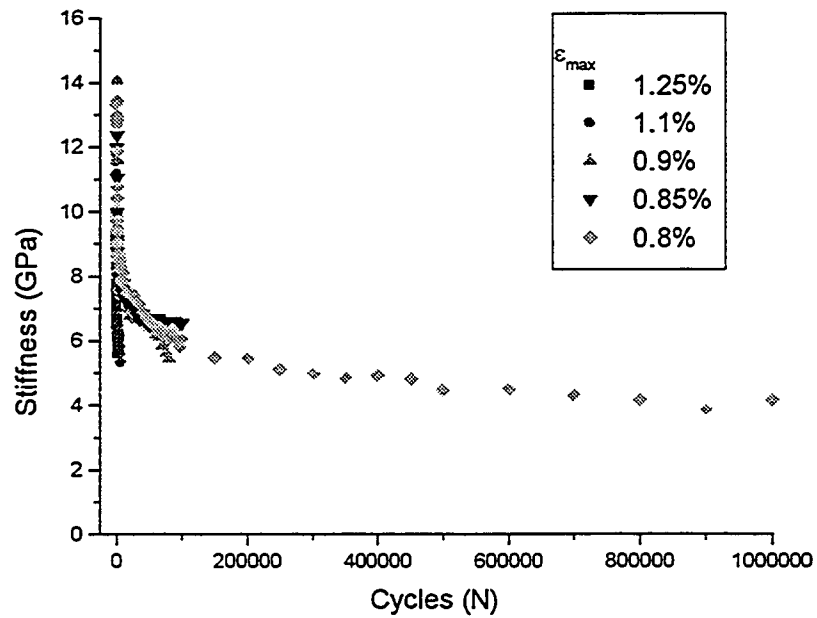
Figure 3.21: Stiffness vs. cycles (linear scale) for (±45/90₃)ₛ specimens under strain control loading
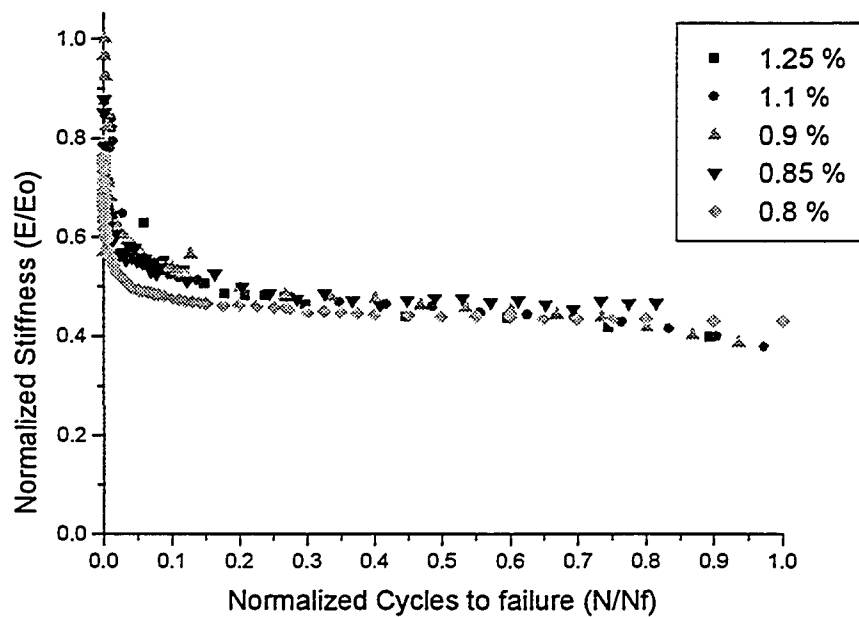
Figure 3.22: Normalized stiffness vs. normalized cycles (linear scale) for (±45/90₃)ₛ specimens under strain control loading
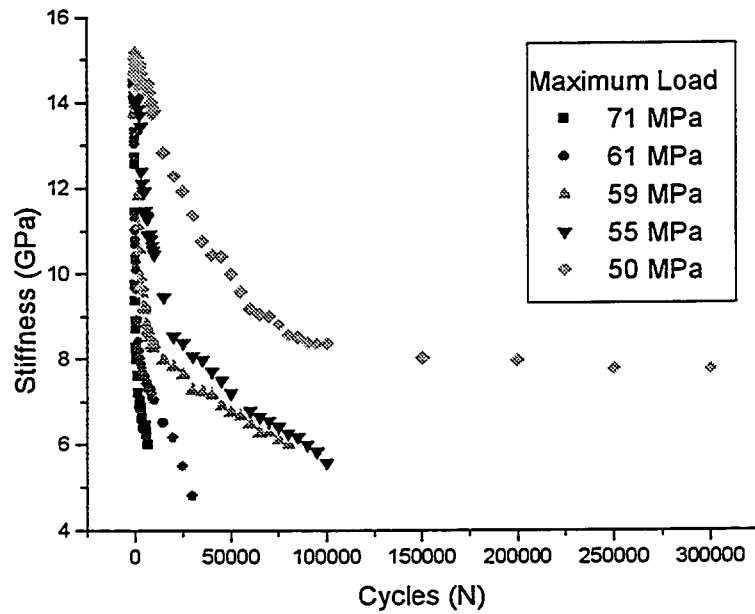
Figure 3.23:   Stiffness vs cycles (linear scale) for ($\pm$45/90$_3$)$_s$ coupon specimens under load control
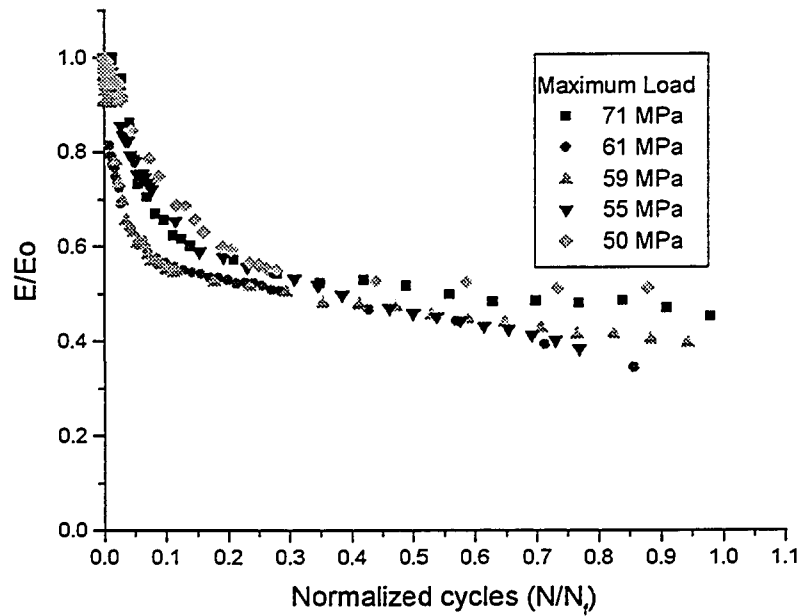
Figure 3.24: Normalized stiffness vs. normalized cycles (linear scale) for ($\pm$45/90$_3$)$_s$ coupon specimens under load control
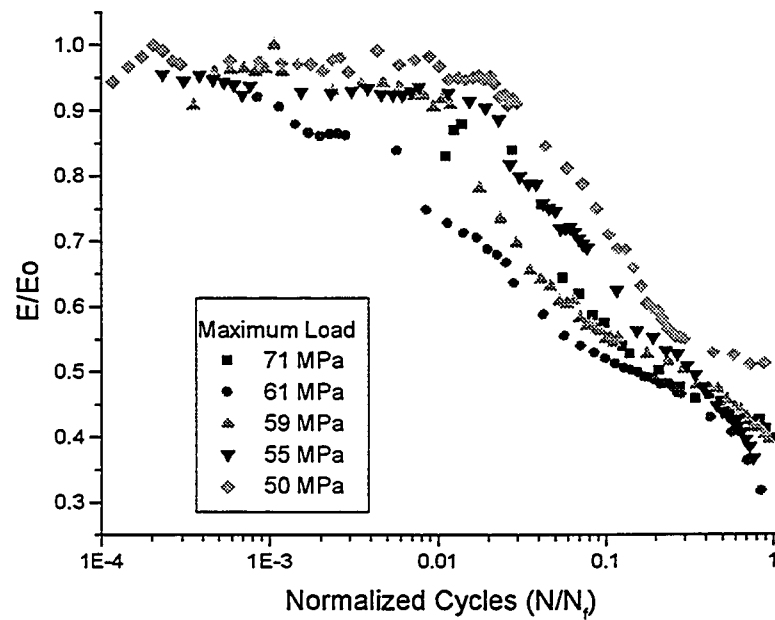
Figure 3.25: Normalized stiffness vs. normalized cycles (log scale) for $(\pm 45/90_3)_s$ specimens under load control where Eo is maximum stiffness found from all tests
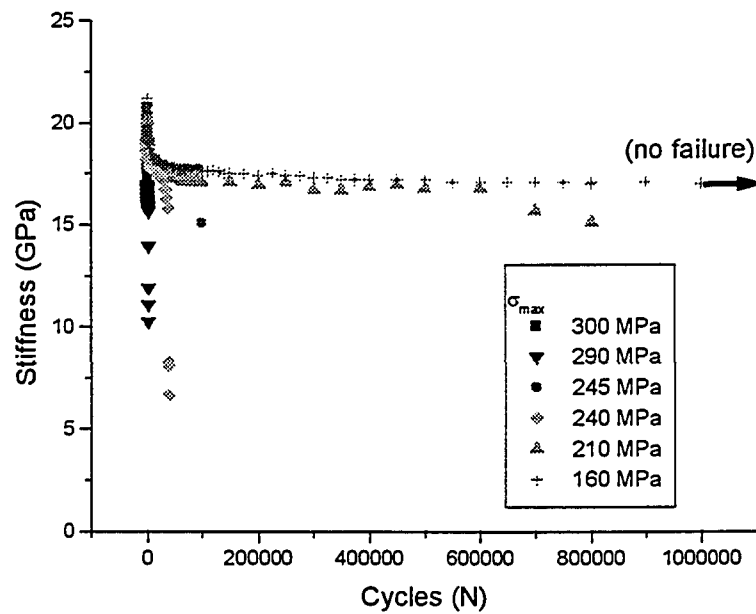
Figure 3.26: Stiffness vs. cycles (linear scale) for $(0_2/90_3)_s$ specimens
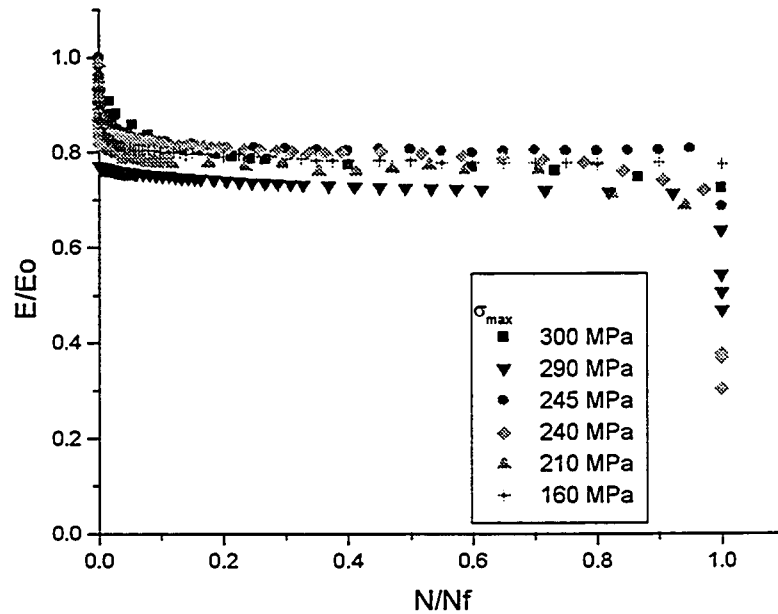
Figure 3.27: Normalized stiffness vs. normalized cycles (linear scale) for $(0_2/90_3)_s$ cross-ply specimens

3.4 Crack Density vs. Stiffness Reduction Curves

The graphs shown so far indicate that most of the stiffness loss in laminates can be attributed to transverse matrix cracking in the 90° plies of the tested specimens. To examine this further stiffness reductions were correlated with crack densities. Plots for the various specimens are shown in Figures 3.28-3.30. The slopes of these plots, as well as the quasi-static plots, were found using a linear fit and are displayed in Table 3.6.

Table 3.6: Slopes of crack density vs. stiffness curves for various laminates

	$(0_2/90_3)_s$	$(\pm45/90_3)_s$
Quasi-static tests	-9.2122 GPa/(crack/mm)	-11.623 GPa/(crack/mm)
Cyclic (load control)	-9.5101 GPa/(crack/mm)	-16.871 GPa/(crack/mm)
Cyclic (strain control)	No Data.	-14.696 GPa/(crack/mm)

Table 3.4 shows that there is a higher stiffness reduction per 90° matrix crack in the $(\pm 45/90_3)_s$ specimens when compared with the $(0_2/90_3)_s$ specimens. This may be attributed to matrix cracking in the constraining plies of the $(\pm 45/90_3)_s$ specimens that is unaccounted for in the crack density measurements. It may also be due to visco-plastic effects in the matrix of the 45° constraining plies which is not present in the 0° constraining plies. Also of interest is the steeper slope in the cyclic tests compared to the quasi-static ones. This is due to a higher rate of crack propagation in the constraining plies under cyclic loading. When the cracks are very small, as in the constraining plies, their propagation rate is also slower. In the quasi-static loading cases this results in a lower constraining ply crack density, and less stiffness reduction. Since the $(0_2/90_3)_s$ specimens do not have crack growth in the constraining plies which results in stiffness losses, these specimens do not have large differences between the quasi-static and cyclic tests.

In all of the crack density vs. stiffness curves the largest deviations from linearity occur near the start and the end of the curve. This is due to stiffness reduction from damage modes other than matrix cracking. At the start of the test the non-linearity may be due to microdamage, viscous effects, or some unknown effects which cause changes in stiffness. Near the end of the test the non-linearity is more likely from delamination growth which causes further stiffness reduction.
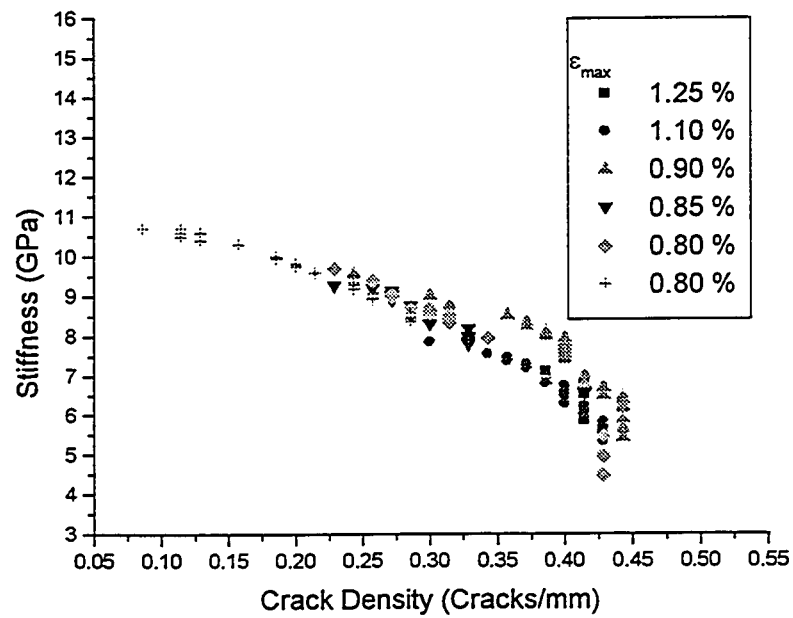
Figure 3.28: Stiffness vs. crack density for ($\pm45/90_3$)$_s$ specimens under strain control
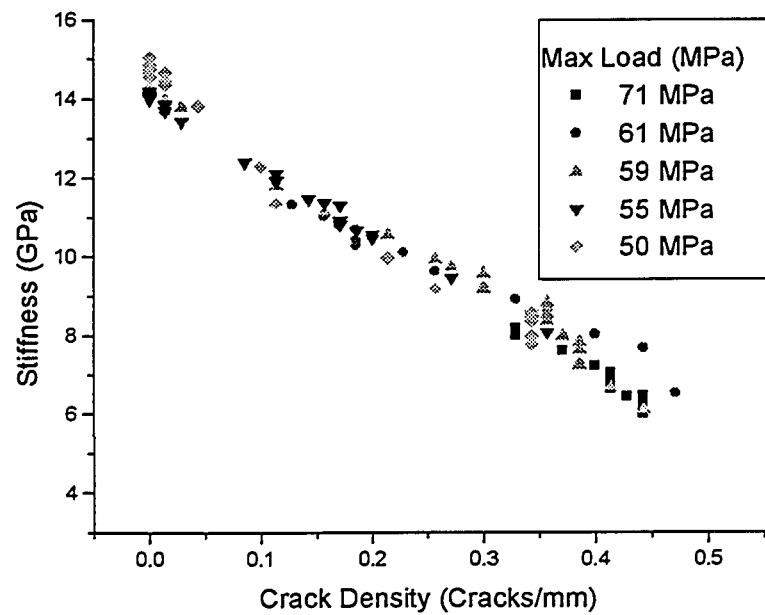
Figure 3.29: Stiffness vs. crack density for ($\pm45/90_3$)$_s$ specimens under load control
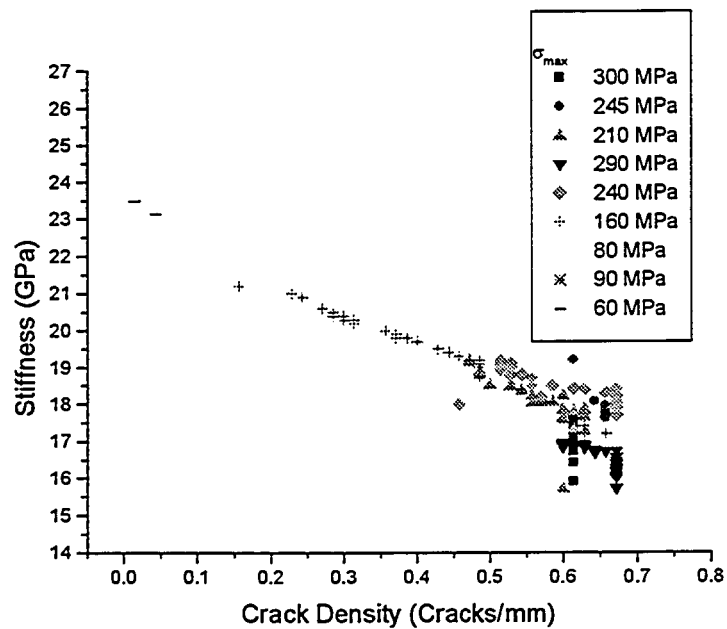
Figure 3.30: Stiffness vs. crack density for $(0_2/90_3)_s$ cross-ply laminates

3.5   Comparisons Between Quasi-Static And Cyclic Tests

Comparisons between cyclic and quasi-static tests of composites can be difficult. In this study, three variables were compared: the crack densities, the stiffness reductions, and the failure modes of the specimens.

To compare the crack growth between the quasi-static and cyclic loads, the common axis of maximum stress or strain and crack densities were plotted. The quasi-static results were plotted on the same figures as the cyclic results under the assumption that they were a cyclic test of one cycle in duration. By plotting this data against cyclic plots a good comparison could be made. The cyclic tests were stopped at 10, 100, 1000, etc. cycles and the crack density was counted. These values were then plotted against the

maximum applied load or strain. A variety of tests were performed over a range of stress

values so that isocycle lines could be produced. These curved lines represent a constant

number of cycles. These plots are shown in Figures 3.31,3.32,and 3.33 for the $(\pm45/90_3)_s$

specimens under strain control, the $(\pm45/90_3)_s$ specimens under load control, and the

$(0_2/90_3)_s$ specimens under load control respectively.
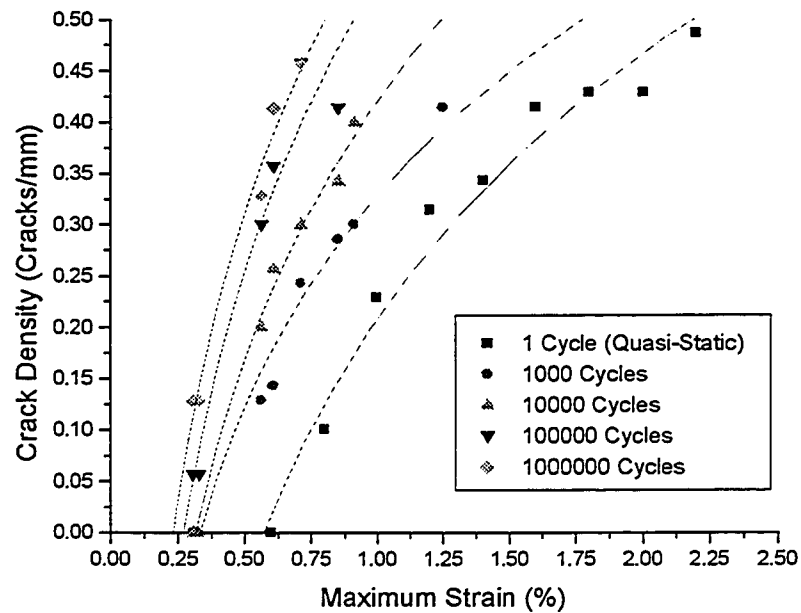
Figure 3.31: Relationship between maximum strain and crack density at N cycles for
$(\pm45/90_3)_s$ specimens under strain control
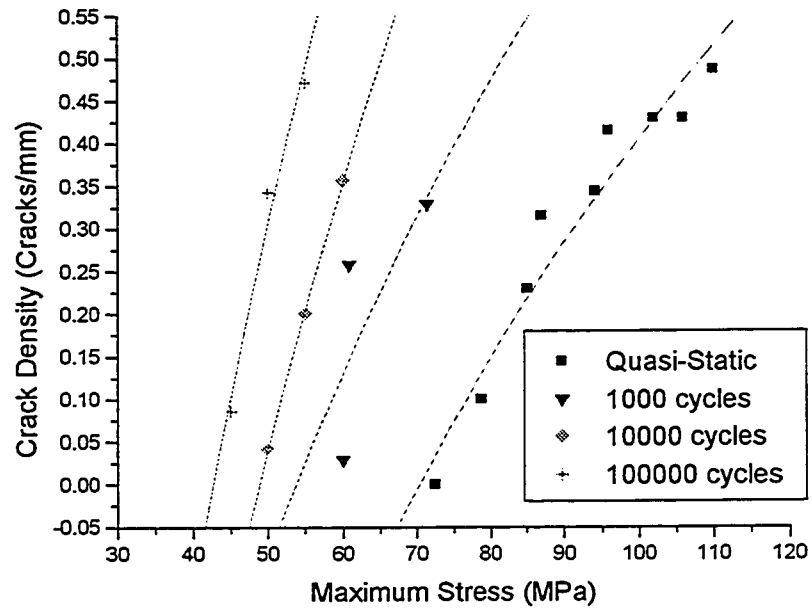
Figure 3.32: Relationship between maximum stress and crack density at N cycles for
$(\pm 45/90_3)_s$ specimens under load control
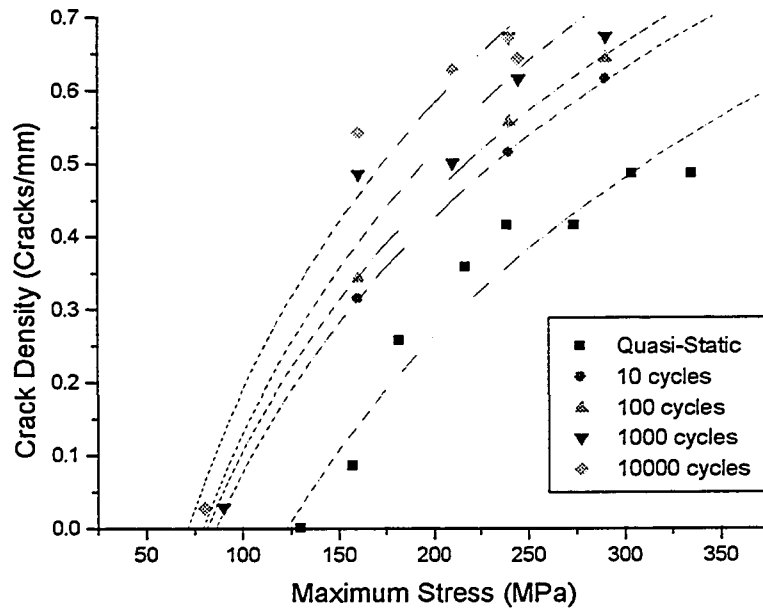
Figure 3.33: Relationship between maximum stress and crack density at N cycles for
$(0_2/90_3)_s$ specimens under load control

In these figures the abscissa reflects the control mode: strain control tests have the x-axis as strain, while load control tests have the x-axis as stress. Several important findings come from these figures. In all of the plots, matrix cracks initiate at lower loads and strains under cyclic loading than under quasi-static loading. As well in all cases, for a given maximum stress or strain, a larger number of cracks occur under cyclic loading.

For the $(\pm45/90_3)_s$ specimens under strain control cracking is seen to initiate at as low as 0.3% strain under the cyclic tests compared to an initiation point of 0.6% strain in the quasi-static tests. Both the quasi-static and cyclic loading reach a similar final crack density of 0.45 cracks/mm in this case.

The $(\pm45/90_3)_s$ specimens under load control initiate cracks at applied maximum stresses as low as 50 MPa for the cyclic tests compared to about 70 MPa for the quasi-static tests. A final crack density of approximately 0.45 cracks/mm was seen in both the quasi-static and cyclic tests.

For the $(0_2/90_3)_s$ specimens under load control the cracks initiate at loads as low as 75 MPa compared with 125 MPa for the quasi-static tests. In the case of this specimen a higher final crack density is achieved under cyclic loading (0.65 cracks/mm) than is achieved under quasi-static loading (0.45 cracks/mm).

The isocycle curves appear to converge towards a single line for the $(\pm45/90_3)_s$ specimens under strain control and the $(0_2/90_3)_s$ specimens under load control. These are the same specimens that reached saturation states of matrix cracks. Also of note is that in these two specimens, none of the curves fall lower than 0.25% strain for the $(\pm45/90_3)_s$

laminates, or below 75 MPa for the $(0_2/90_3)_s$ laminates, suggesting that there is a level below which no cracks will initiate.

Another comparison between the quasi-static and cyclic loading is the stiffness drop per crack density, as outlined in section 3.4.5. Of particular note is the data from Table 3.6 which shows that there is a larger stiffness drop per 90° matrix crack under cyclic loading than that of quasi-static loading. This extra reduction in stiffness is due to increased crack growth in the constraining plies, which is not as prominent in the quasi-static test specimens. The constraining ply cracks have a slower propagation rate than the 90° cracks, which propagate through the width immediately under both quasi-static and cyclic loading. These constraining ply cracks are seen in the cyclic test specimens, but do not grow in the quasi-static specimens because of the short duration of loading. Consequently, a higher rate of stiffness reduction per 90° cracks is observed in cyclically loaded specimens.

There exist several differences between the failure modes of the specimens under the different test conditions. As mentioned, matrix cracking begins at lower loading rates in the cyclic specimens. Delamination growth also varies quite substantially between the two loading cases. In the $(\pm45/90_3)_s$ specimens under cyclic loading delaminations grow in many areas and one main delamination propagates to cause the ultimate failure of the specimen. The delamination growth differences are even more pronounced for the $(0_2/90_3)_s$ specimens. In the quasi-static tests the delamination growth is purely an effect of fibre failure just before the specimen failure. There is little redistribution of load to the outer plies, instead the load is increased until the outer constraining ply fibres break. In

the cyclic tests a substantial amount of the delamination growth is seen to propagate out of longitudinal matrix cracks and from the edges. When the delaminations have progressed to the point where the redistributed load is sufficient to cause fibre failure, an instantaneous failure results.

The ultimate failure modes for both quasi-static and cyclic loading are the same. In the $(\pm 45/90_3)_s$ specimens failure is due to shear failure of the matrix in the constraining plies. In the $(0_2/90_3)_s$ specimens ultimate failure is due to fibre failure in the constraining plies.

3.6   Comparisons of Matrix Dominated and Fibre Dominated Laminates Under Cyclic Loading

Comparisons between matrix dominated $(\pm 45/90_3)_s$ and fibre dominated $(0_2/90_3)_s$ specimens is useful in determining the effects of the fibres and the matrix on the overall composite laminates. It was found that although both of these types of specimens undergo the same modes of damage throughout their cyclic lives, there are some distinct differences in how the damage initiates and propagates throughout the specimens. Comparisons of the test cases under load control were performed.

Damage growth for the $(0_2/90_3)_s$ and $(\pm 45/90_3)_s$ specimens was described in section 3.3.1. Any differences between these two types of laminates began when damage propagated into the constraining plies. Here damage growth in the form of matrix cracking and delamination varied with respect to the fibre orientation. In the $(\pm 45/90_3)_s$ specimens matrix cracking was seen in the constraining plies at $45°$ angles from the

direction of loading. The $(0_2/90_3)_s$ specimens produced longitudinal matrix cracking at $0°$

angles with respect to the direction of loading.

Delamination growth resulted in different ultimate failure modes between the two

laminates. In the $(\pm45/90_3)_s$ specimens triangular delaminations grew across the width of

the specimen until only the matrix in the constraining plies remained to carry the load.

When the specimen reached this stage, ultimate failure occurred due to shear failure of

the matrix in the constraining plies. The $(0_2/90_3)_s$ specimens failed under cyclic loading

when delaminations had grown throughout the length of the specimen. When sufficient

load had been transferred to the constraining plies due to the delamination growth, fibre

failure in the $0°$ plies began. An instantaneous failure was the result.

The fatigue-life curves, shown in Figures 3.9 and 3.10 for both of these specimens

also were different. Damage growth initiated and propagated at lower global loads in the

$(\pm45/90_3)_s$ specimens. This was due to the difference in stiffness of the constraining plies

between the two specimens.

Stiffness reduction curves (Figures 3.23-3.25 and 3.26-3.27) showed that there

was a much more significant reduction in stiffness for the $(\pm45/90_3)_s$ than that for the

$(0_2/90_3)_s$ specimens. Another difference of note was that the reduction in stiffness in

$(\pm45/90_3)_s$ specimens continued well after most of the matrix cracking in the $90°$ had

been exhausted. This extra stiffness reduction was due to matrix cracking in the $45°$

constraining plies, delamination growth, and viscoplastic effects in the matrix. This type

of response was not present in the $0°$ plies of the $(0_2/90_3)_s$ specimens since the elastic

fibres took the entire load, and matrix cracking in these plies resulted in only a slight decrease in stiffness.

Crack density plots also showed differences. The $(0_2/90_3)_s$ specimens were seen to reach a saturation state, whereas the $(\pm45/90_3)_s$ specimens did not. This was due to continuously increasing strain in the inner plies of the $(\pm45/90_3)_s$ specimens as the strain in the constraining plies increased (A combination of elastic and plastic strains). This allowed new cracks to form, hence no saturation state was achieved. In the $(0_2/90_3)_s$ specimens the strain in the constraining plies was fully elastic, so the overall strain that the specimen underwent throughout the test remained fairly constant, resulting in a saturation state of matrix cracks.

The crack density at failure for the $(0_2/90_3)_s$ specimens was ~0.65 cracks/mm, while the $(\pm45/90_3)_s$ produced a crack density of ~0.45 cracks/mm. This is due to higher stress gradients between the $0°$ and $90°$ fibres than between the $45°$ and $90°$ fibres.

The stiffness reduction vs. crack density plots for the two types of specimens (See Figures 3.29-3.30) showed a variance in stiffness reduction per crack. As outlined in Table 3.6, the stiffness reduction for a given crack density was much higher for the $(\pm45/90_3)_s$ specimens than it was for the $(0_2/90_3)_s$ specimens. The reason for such a large difference is that crack propagation in the $45°$ constraining plies results in a larger stiffness loss. This constrained ply cracking is unaccounted for as only the inner plies were considered in the stiffness reduction calculations. The result is a higher stiffness per inner ply crack density.

3.7   Comparisons Between (±45/90₃)ₛ Specimens Tested Under Load Control And Strain Control

Different control modes can have an effect on damage growth in composites. To determine the effect of the load control mode, the $(\pm45/90_3)_s$ laminates were tested under both load control and strain control.

Visual damage examination found that specimens tested under load control had an accelerated rate of damage growth when compared to the strain control tests. In a load controlled test, the global load remains constant, while the local loads carried by individual plies varies. As matrix cracks propagate through the 90° plies, the load is largely redistributed to the outer plies. This results in an accelerated damage growth in the constraining plies, resulting in quicker ultimate failure of the specimen.

In the strain control tests the global strain remains the same. As damage grows in these specimens, a stress relaxation takes place. As a result of this relaxation, less damage initiates and propagates which leads to an increased life compared with the load controlled tests.

When comparing the stresses and strains for the initiation of cracking, both the load control and strain control tests had the initiation points fall on similar lines (See Figure 3.13). This is because it is the growth of damage that causes differences between the two control modes. To determine the point of initiation of damage in a composite specimen either control mode will give similar stress and strain results.

3.8   Summary

The analysis of the cross-ply and multi-ply specimens under cyclic loading produced some interesting results. Comparisons of the cyclic tests with quasi-static loading cases showed a number of differences. By testing the $(\pm 45/90_3)_s$ specimens under both load and strain control, differences in these loading conditions could be found.

By examining the visual damage growth, different damage modes were observed. In these laminates damage initiated in the form of matrix cracking in the 90° plies. It was followed by matrix cracking in the constraining plies, which then progressed to delamination between the inner plies and the constraining plies. Ultimate failure came in the form of shear failure of the matrix in the $(\pm 45/90_3)_s$ specimens, and brittle fibre failure in the $(0_2/90_3)_s$ specimens.

Damage curves developed for the specimens showed trends regarding how the damage modes initiated in the specimens. The trends showed that over the range of loads examined, all of the damage modes happened in a systematic and predictable way except at very low loads. On a logarithmic scale the damage curves all fell on straight lines, suggesting that the cycles between the different damage modes increased logarithmically. Figures 3.10 and 3.12 showed that at very low loads crack initiation points did not follow the damage curve. This could suggest that at low loads the crack initiation behaviour may change. Further testing at these low loads is required to substantiate this finding.

By examining the transverse crack growth the loading rate required for damage initiation, and trends of damage propagation could be seen. Transverse cracks grew

rapidly after initiation of cracking, and slowed as the stress in the inner plies relaxed. In the $(0_2/90_3)_s$ specimens under load control and the $(\pm45/90_3)_s$ specimens under strain control, a saturation state of matrix cracking was seen. In the $(0_2/90_3)_s$ specimens this was due to the high load carrying capacity of the $0°$ plies which allowed matrix cracking to fully propagate through the inner plies before any change in stiffness began in the constraining plies. In the $(\pm45/90_3)_s$ specimens under strain control the saturation state was achieved because the damage growth is related to the amount of strain applied. Since the strain was kept constant no new transverse cracking initiated after stress relaxation in the specimen. The crack growth curves showed that there was a crack onset delay of approximately 1% of the life of the specimen for the $(\pm45/90_3)_s$ specimens tested under load control.

Stiffness reduction plots showed a bi-linear curve for all of the specimens. This indicated that different damage modes were dominant throughout the life of the specimens. A similar drop in the magnitude of the stiffness was seen due to matrix cracking for both the $(\pm45/90_3)_s$ and $(0_2/90_3)_s$ specimens, although a much higher percentage of the total stiffness was reduced due to matrix cracking in the $(\pm45/90_3)_s$ specimens.

By comparing stiffness vs. crack density plots, a direct correlation between matrix cracking and stiffness losses was observed. The larger stiffness reduction in the $(\pm45/90_3)_s$ specimens was due to unaccounted matrix cracking in the constraining plies.

4   Constrained Angle-Ply Experiments

Angle-ply composites are among the most common lay-ups in service today. In many design cases forces act in a multiplicity of loading directions. This off-axis loading is best compensated for by using angle ply laminate designs.

The purpose of these tests was to produce damage curves for different damage modes (matrix crack initiation, matrix crack saturation, and delamination initiation) of angle ply laminates. In a high-pressure pipe, the functional failure of the pipe is in the form of weepage, where the liquid penetrates out of the composite pipe through minuscule matrix cracks. The onset of weepage is found to correlate with the point of crack saturation in the tubular specimens, well before ultimate failure of the pipe [29]. For this reason the design of the high pressure pipe to contain fluids should be at strain levels lower than that which produces a saturated crack state over the life of the design. In the tests performed here, the angle plies are surrounded on either end by 0° layers, hence the term "constrained angle-plies".

4.1   Summary of Cyclic Specimens Examined

Three angle-ply orientations were examined.   The chosen lay-ups were $(0/\pm25_4/0)_T$, $(0/\pm45_4/0)_T$, and $(0/\pm75_4/0)_T$. These were chosen to study the effect of different angles on the damage development states. Previous research at the University of Alberta found that the optimum fibre angle for a high pressure composite pipeline was approximately 65° relative to the axial direction of the pipe [31]. A composite pipe

oriented at 65° under hoop loading is comparable to the $(0/\pm25_4/0)_T$ coupon specimens

under axial loading. As well, the $(0/\pm75_4/0)_T$ specimen under axial loading is similar to a

65° composite pipe under axial loading. This is a preliminary comparison, since tubular

specimens do not have edge effects and the difference in geometry may effect the

comparisons in damage growth. As well, biaxial loading conditions are not taken into

account. Nevertheless, it is deemed useful to study the behaviour of angle-plies on

coupon specimens to gain an insight into the damage development. An illustration of the

comparable tests is shown in Figure 4.1.
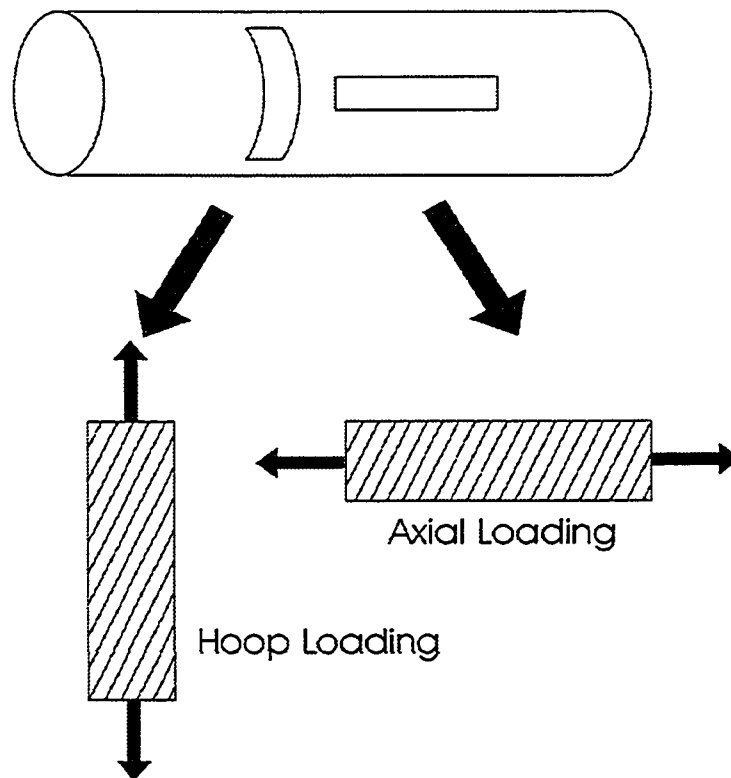
Figure 4.1: Application of coupon specimens to composite pipe design

The 0° layers were introduced to the specimens to act as outer constraining layers

for the composite, as well as to prevent excessive creep in the matrix dominated angle-

ply specimens (45 and 75 degree specimens.) When matrix cracking begins in these specimens, the 0° layers also help to prevent immediate failure of the specimen.

A summary of the constrained angle-ply specimen tests performed was compiled and is shown below in Tables 4.1, 4.2, and 4.3.

Table 4.1: $(0/\pm25_4/0)_T$ specimens tested under strain control

SPECIMEN: $(0/\pm25_4/0)_T$	Loading type : Strain Control
Specimen Name	Maximum Applied Strain
AF-156	1.40%
AF-157	1.50%
AF-158	1.10%
AF-159	0.90%
AF-160	0.70%
AF-161	1.25%
AF-162	1.00%
AF-163	1.325%
AF-164	1.10%

Table 4.2: $(0/\pm45_4/0)_T$ specimens tested under strain control

SPECIMEN: $(0/\pm45_4/0)_T$	Loading type: Strain Control
Specimen Name	Maximum Applied Strain
AF-143	1.20%
AF-144	1.60%
AF-145	1.00%
AF-146	0.80%
AF-147	1.30%
AF-148	1.40%
AF-149	1.50%
AF-150	1.10%
AF-151	1.20%
AF-152	1.20%

Table 4.3: $(0/\pm 75_4/0)_T$ specimens tested under strain control

SPECIMEN: $(0/\pm 75_4/0)_T$	Loading type: Strain Control
Specimen Name	Maximum Applied Strain
AF-166	0.80%
AF-167	0.60%
AF-168	0.40%
AF-169	0.30%
AF-170	0.70%
AF-171	1.00%
AF-172	1.10%

4.2 Testing Procedure

The three different lay-ups were tested in similar fashions. First, monotonic tests were performed to determine the stress-strain characteristics of the specimen. Subsequently, cyclic tests were performed with the maximum strain amplitude being equal or less than the monotonic strain where the matrix cracking first occurred. This was done over a range of amplitudes to develop fatigue-life curves for the different damage modes.

For the monotonic tests, a strain rate of $10^{-4}s^{-1}$ was used in all cases. As the tests were being performed, images of the specimen, hence damage development, were taken at regular strain intervals. For cyclic tests the testing parameters outlined in chapter 2 section 2.5 were followed.

It is noted that to determine the initiation of matrix cracking required very low strains to be applied on the specimens. These loads proved to be too small to cause

ultimate failure of the specimens in a reasonable time period. To provide an upper bound, all tests were stopped after 1×10^6 cycles.

4.2.1 Damage Detection Methods And Testing Software

Two separate apparati were used to visually examine damage growth in the angle-ply coupon specimens. These consisted of the image processor developed by Wolodko, Hoover, and Ellyin [28], and the optical microscope. Coupled with these visual methods were stiffness measurements that were recorded at regular intervals throughout the tests. These damage detection methods are outlined in chapter 2, section 2.6.

The testing software implemented in this series of tests was closed loop controlling software called MTM301 developed in house by Wolodko [29]. Further explanation of this controlling software is discussed in chapter 2, section 2.3.1.

4.3 Monotonic Test Results

Monotonic tests were performed on the three types of constrained angle ply specimens. In this examination only single-ramp monotonic tests were performed, differing from the quasi-static tests performed in the last chapter. Ultimate failure stresses and strains were found, and the onset of the various damage modes were recorded. These tests were used as a guide to determine the magnitude of strains to be applied in the cyclic tests.

4.3.1   Stress-Strain Curves

Monotonic stress-strain curves were produced for each of the different

angle ply laminates and are shown in Figure 4.2.
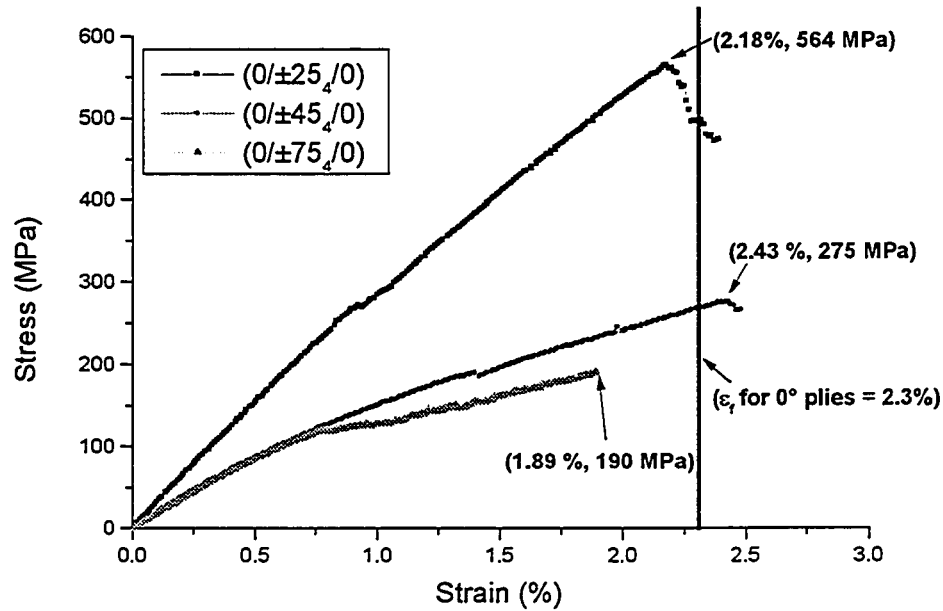
Figure 4.2: Monotonic stress-strain curves for $(0/\pm\theta/0)_T$ coupon specimens where
θ =25,45, and 75 degrees

The stress-strain plot shows that the curves are very different for the various

laminate configurations. The $(0/\pm75_4/0)_T$ specimen produced a bi-linear curve. At 0.75 %

strain, matrix cracking began, and this caused a decrease in the load carrying capacity of

the laminate.   This matrix cracking continued until failure of the specimen at 1.89 %

strain and a stress of 190 MPa.   Matrix cracking could be seen visually in this specimen

and produced a web-like crack pattern, cracking along the $\pm75°$ fibres, shown in Figure

4.3.
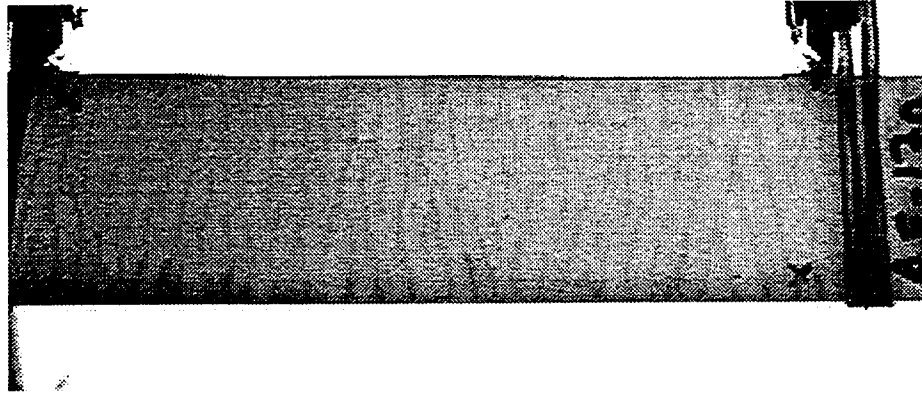
Figure 4.3: Characteristic crack pattern seen in $(0/\pm75_4/0)_T$ specimens

Both the $(0/\pm45_4/0)_T$ and $(0/\pm75_4/0)_T$ specimens followed similar initial curves. At 0.75% strain, the $(0/\pm75_4/0)_T$ specimen developed matrix cracks, while the $(0/\pm45_4/0)_T$ specimen did not. No visual matrix cracking was experienced in these specimens until the point of ultimate failure. The reason for this deviation is that less load is required to fracture the 75° laminae plies than is required to fracture the 45° plies. In the 75° layers, most of the cracking occurs in the form of Mode 1 fracture – most of the load enacted on these layers is in a direction normal to the fibres. For the 45° layers, a mixed mode fracture takes place. Equal shear and normal forces exist in the individual plies, so a higher total load is required to fracture the matrix. More of the load is directed to the fibres in the 45° plies than in the 75° plies. The result is the $(0/\pm45_4/0)_T$ specimens have a stronger load carrying capability of 275 MPa, and a higher failure strain of 2.43%.

The $(0/\pm25_4/0)_T$ specimen produced the steepest stress-strain curve of all with load carrying capabilities of 564 MPa, more than double that of the other laminates. The reason for this is the orientation of the 25° fibres is close to that of the direction of loading. The fibres retain most of the load in these specimens, as opposed to the other

specimens where the matrix retains a larger portion of the load. This specimen produced no matrix cracks or delamination until fibre failure began to appear at a strain of 2.18%. From here the specimen ruptured and failed almost immediately.

The $(0/\pm45_4/0)_T$ and $(0/\pm75_4/0)_T$ specimens followed similar initial stress-strain curves, while the $(0/\pm25_4/0)_T$ specimens followed a steeper slope. The reason for this difference is that in the $(0/\pm45_4/0)_T$ and $(0/\pm75_4/0)_T$ specimens the global stiffness is affected to a larger degree by the stiffness of the matrix in the θ plies, while in the $(0/\pm25_4/0)_T$ specimens the fibres are oriented in such a direction that they contribute to a higher stiffness in this specimen. Classical Laminate theory found stiffness values of 31.69 GPa, 19.79 GPa, and 16.69 GPa for the $(0/\pm25_4/0)_T$, $(0/\pm45_4/0)_T$, and $(0/\pm75_4/0)_T$ specimens respectively. This compares well with the slopes in Figure 4.2.

Another interesting note is the much lower failure strain of the $(0/\pm75_4/0)_T$ specimens. Since much more matrix cracking is present in these specimens, a higher percentage of the load is transferred to the outer $0°$ plies. This extra load transfer results in a much earlier failure strain than in the other two specimens. The other specimens do not develop through width matrix cracks, and thus do not redistribute as much load to the constraining plies.

Previous research by Wolodko [29] found that the failure strain for $0°$ plies alone was approximately 2.3%. This falls within the average of the failure strains for all of these specimens, as indicated by the solid line in Figure 4.2. This suggests that the ultimate failure of the specimen is dominated by the outer $0°$ plies. Since the purpose of

these tests was to determine how damage propagated in the inner angle plies, the ultimate

failure of the specimens was not studied further.

4.3.2 Damage Propagation under Monotonic Loading

Damage propagation in each of the three specimens examined proved to vary with

the changing angles.

It was very hard to determine any damage growth in the $(0/\pm25_4/0)_T$ and

$(0/\pm45_4/0)_T$ specimens at the load levels listed in Tables 4.1 and 4.2. No visual crack

growth or delamination was visible in either of these specimens until very close to the

ultimate failure. Just before the ultimate failure, fibre failure in the 0° plies took place.

Delaminations grew between the constraining plies and the angle plies from these failure

sites. Matrix cracking also resulted at the same time in the angle plies. Fracture of the

matrix in the inner angle plies was in the form of shear failure.

Damage growth in the $(0/\pm75_4/0)_T$ specimen took place in a much more

systematic and steady manner. The first visible damage growth began at 0.75% strain,

when matrix cracking became visible through the width of the specimen. This matrix

cracking continued until the ultimate failure of the specimen. Since cracking continued

until the ultimate failure, it was not possible to determine whether a saturation state of

matrix cracks had formed. Visible delamination growth was not seen until very close to

the failure of the specimen. Similar to the other laminates examined, the delamination

growth occurred very close to the point of fibre failure.

Of the three angles examined, only the $(0/\pm75_4/0)_T$ produced any visual matrix cracking pattern on the image processor. In the $(0/\pm25_4/0)_T$ and $(0/\pm45_4/0)_T$ specimens the only hint of damage came in the form of acoustic emission as the strain increased. Since a microscope was not used to examine these specimens, the amount of edge crack growth for a monotonic test was not determined.

4.3.3 Ultimate Failure of Monotonic Specimens

The failure of the monotonic specimens varied between each specimen. Images of the three failed angle-ply laminates are shown in Figures 4,4, 4.5, and 4.6.

The failure of all specimens took place along the angle of the inner plies. For all of the $(0/\pm\theta_4/0)_T$ specimens the ultimate failure was along the fibre direction at an angle of $\theta°$. Of interest was the fact that although these specimens have an outer $0°$ layer, a large brush failure such as what was seen in earlier cross ply specimens was not experienced (See Chapter 3, Figure 3.6). Instead delamination and fibre failure in the constraining plies took place around the area where the inner plies had failed. This is likely due to lower stress gradients between the constraining plies and the inner plies than is experienced in the cross-ply specimens.
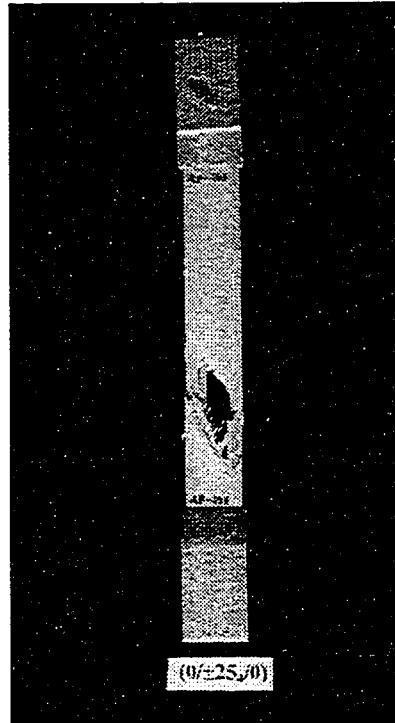
Figure 4.4: A failed $(0/\pm25_4/0)_T$ coupon specimen under monotonic loading
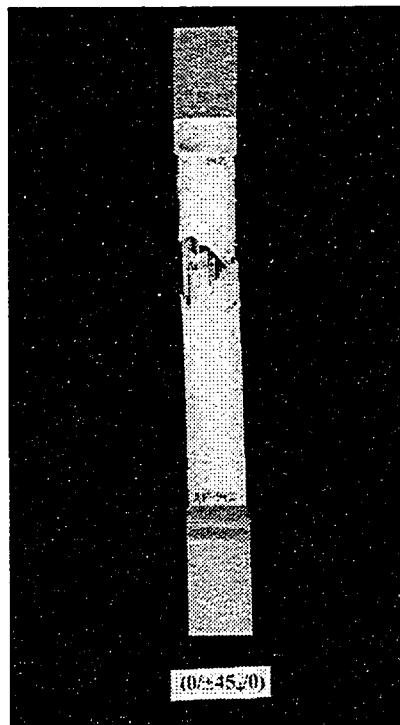
Figure 4.5: A failed $(0/\pm45_4/0)_T$ coupon specimen under monotonic loading
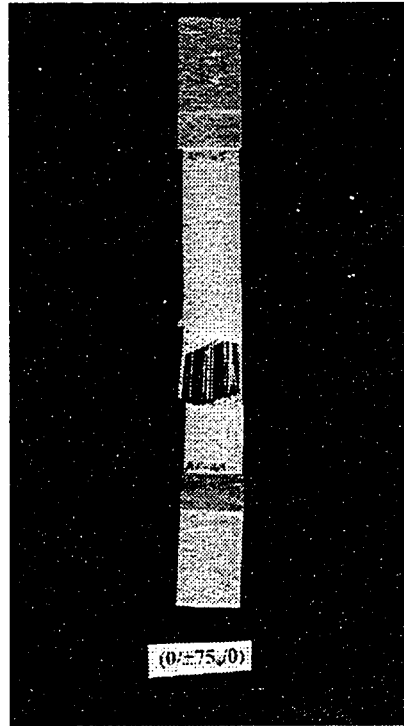
Figure 4.6: A failed $(0/\pm75_4/0)_T$ coupon specimen under monotonic loading

4.4 Cyclic Test Results

4.4.1 Description of Damage Growth During Cyclic Testing

Damage growth throughout all of the three geometries followed predictable patterns irrespective of the loading level. Damage growth in the constrained angle ply composites was much different from that of the cross-ply and multi-ply specimens examined in Chapter 3, testifying to the complexity of damage analysis in composites.

Similar to the monotonic test results, damage growth was very small in the $(0/\pm25_4/0)_T$ and $(0/\pm45_4/0)_T$ specimens. In these geometries damage propagation was only from the edges, with very little damage visible through the width of the specimen.

In contrast, the $(0/\pm75_4/0)_T$ geometries produced a matrix crack pattern throughout the width of the specimens, very similar in form to that seen during monotonic loading.

In all of the specimens, delaminations grew from the edges of the matrix cracks, linking matrix cracks in neighbouring plies. Delaminations also grew along the edges of the constraining plies, where there was a boundary preventing further matrix crack growth.

4.4.2 Damage Curves

Damage curves consisting of crack initiation, crack saturation, and delamination initiation were produced for the three constrained angle ply composites. These are shown in Figures 4.7, 4.8 and 4.9 for the $(0/\pm25_4/0)_T$, $(0/\pm45_4/0)_T$, and $(0/\pm75_4/0)_T$ specimens, respectively. The crack initiation and delamination initiation damage modes were found using the optical microscope. In the $(0/\pm25_4/0)_T$ specimens the onset of delamination was seen to begin at the same time as crack initiation. When the cracks initiated they quickly developed delaminations on either side. This is shown in Figure 4.7. Delamination growth was most difficult to determine in the $(0/\pm45_4/0)_T$ specimens. In these specimens, the delaminations grew from the edges of matrix cracks. It was difficult to determine when the edge of a matrix crack changed into a delamination site. This contributed to a larger scatter for this curve than for the other curves. This is seen in Figure 4.8.

Crack saturation curves were developed for all specimens. In the $(0/\pm25_4/0)_T$ and $(0/\pm45_4/0)_T$ specimens no visual cracking could be seen with the image processor, so edge crack counts were performed. When the rate of cracking levelled off this was taken

as the edge crack saturation state. For the $(0/\pm75_4/0)_T$, specimen, visual damage growth could be seen using the image processor. The saturation state for this specimen was determined by examining images obtained from the image processor.

In both Figures 4.7 and 4.8 saturation states of cracking could not be obtained at higher strain levels. This problem was not seen in the $(0/\pm75_4/0)_T$ specimens due to the lower strains required to produce a saturation state of matrix cracks.
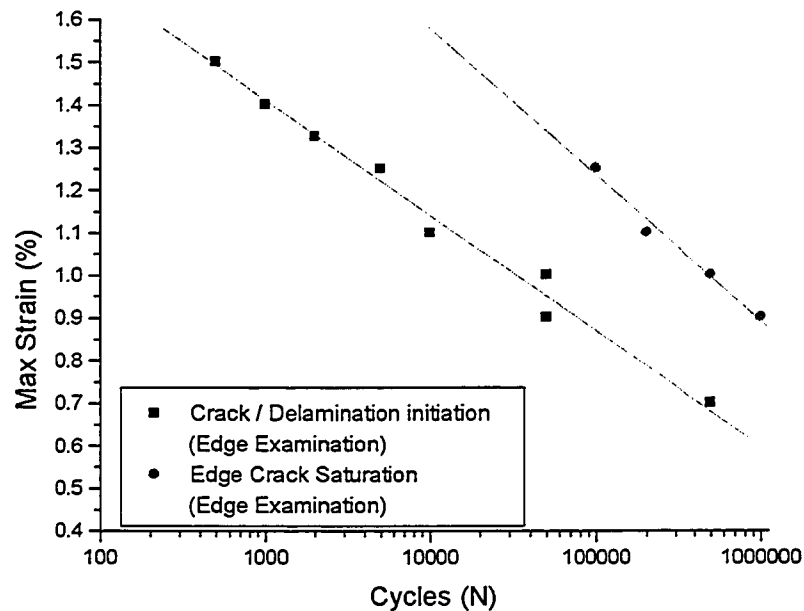
Figure 4.7: Damage curves for $(0/\pm25_4/0)_T$, specimens under strain control
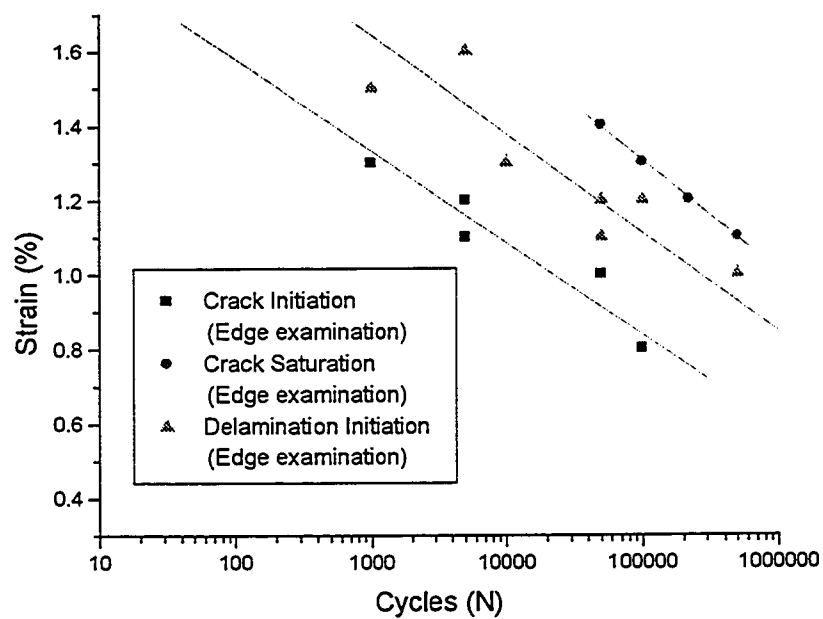
Figure 4.8: Damage curves for $(0/\pm45_4/0)_T$, specimens under strain control
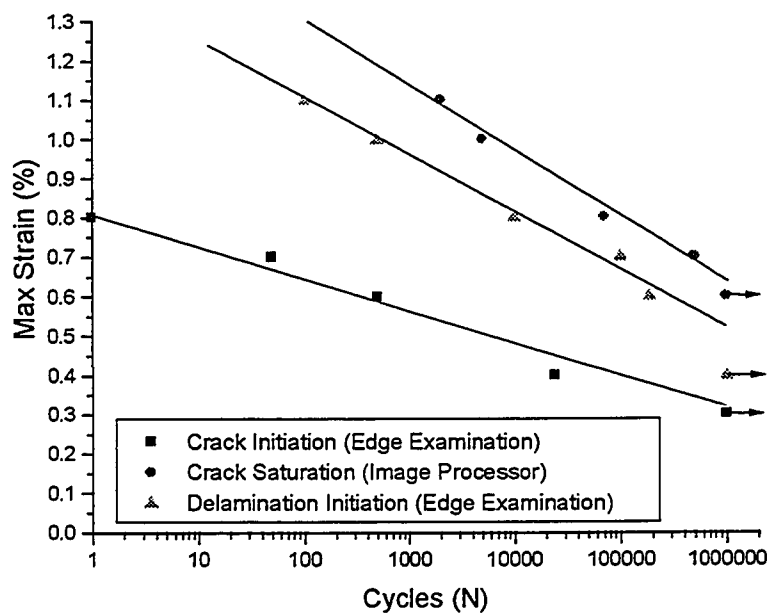
Figure 4.9: Damage curves for $(0/\pm75_4/0)_T$, specimens under strain control

The three damage curves show a systematic method for damage initiation and propagation through the specimens. All of the specimens undergo initiation of matrix cracking, followed by delamination, followed by the achievement of a saturated state of matrix cracks. Interestingly, the matrix cracks reach a saturation state after delamination was initiated, showing that there is an interaction between the different damage modes. Further comparisons between the damage modes in the different specimens are reported in sections 4.4.4 - 4.4.6.

4.4.3 Edge Crack Initiation and Edge Crack Propagation

By using the optical microscope different edge crack states were seen to exist for each of the three different specimens. These are shown in Figures 4.10, 4.11, and 4.12 for the $(0/\pm25_4/0)_T$, $(0/\pm45_4/0)_T$, and $(0/\pm75_4/0)_T$ specimens, respectively. The left image of each figure shows the crack pattern, while the right image shows the same crack pattern enhanced to show the outline of the cracks. There is a definite wavy pattern that all three specimens follow. Delaminations grow between the ply cracks. This pattern of delamination decreases in height as the angle θ of the fibres increases.

It should be noted that the $(0/\pm25_4/0)_T$ and $(0/\pm45_4/0)_T$ specimens produced edge cracks that did not propagate through the width of the specimen. By examining the edge cracks an estimate of how far they penetrated into the specimen was determined. It was assumed that these cracks formed a triangular delamination, similar to that seen in earlier $(\pm45/90_3)_s$ specimens. From the images, measurements of the length of the vertical lines were measured as the height of the delaminations in the specimens, and from these an
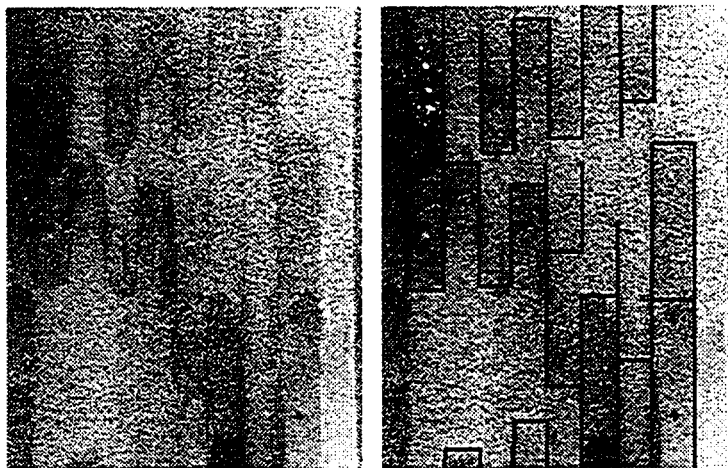
Figure 4.10: Edge crack state in $(0/\pm 25_4/0)_T$ specimen
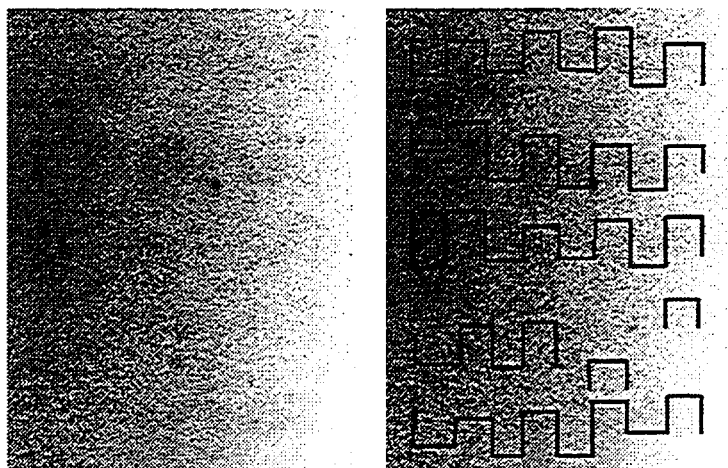
Figure 4.11: Edge crack state in $(0/\pm 45_4/0)_T$ specimen
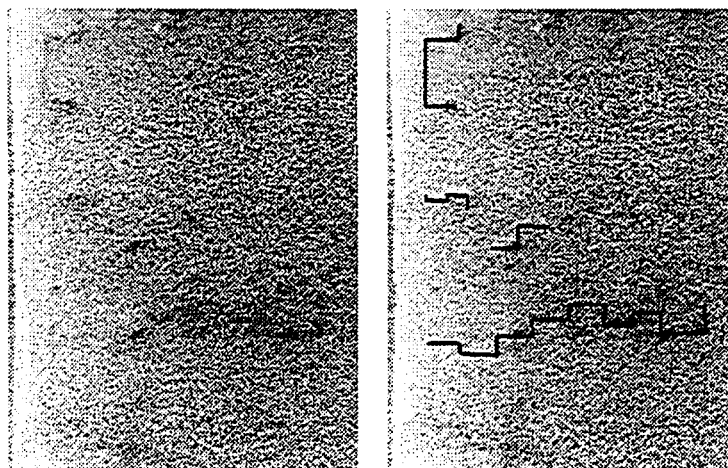
Figure 4.12: Edge crack state in $(0/\pm 75_4/0)_T$ specimen

average height was found. The depth of edge penetration could be found using the equation shown below:

$$\text{Tan}\,(\theta) = \frac{(2 \times \text{Edge Penetration})}{\text{Average Measured Height of Edge Delamination}}$$

The average height of the edge cracks was 0.634 mm for the $(0/\pm25_4/0)_T$ and 0.244 mm for the $(0/\pm45_4/0)_T$ specimens. This led to edge crack penetrations of 0.148 mm for the $(0/\pm25_4/0)_T$ and 0.122 mm for the $(0/\pm45_4/0)_T$ specimens. These values are fairly close to each other, suggesting that the penetration of the cracks into the interior of specimens is similar between angle plies when the fibre angle is less than 45°. A possible explanation for this is that the load required to fracture the matrix increase with the increasing distance from the edge. The fact that there is mixed mode fracture, mostly modes 1 and 2, suggests that very high loads are required for cracks to propagate. This is the same reason why little damage growth is seen before ultimate failure of the monotonic specimens. This suggests that when the θ angle is small, and no crack propagation exists after the initial edge cracking, the cracks can only propagate a certain distance into the specimens. Damage growth and propagation in these specimens can be largely attributed to edge effects.

The matrix cracks in the $(0/\pm75_4/0)_T$ specimens propagate through the width and thickness of the angle-plies very quickly, suggesting that the strains required for the propagation of cracks in fibres at this angle is very low and the mode 1 fracture is dominant. In these specimens the cracks grew until a saturation state throughout the specimen was reached, similar to that shown in Figure 4.3.

4.4.4   Crack Initiation Damage Curves

A plot of the crack initiation curves for all three geometries is shown in Figure 4.13. This plot shows that the strain to produce crack initiation for a given load is much lower for the $(0/\pm75_4/0)_T$ specimens. It is also interesting to note that for the $(0/\pm25_4/0)_T$ and $(0/\pm45_4/0)_T$ specimens the strains to produce crack initiation fall within a relatively narrow band.

The orientation of the plies in the $(0/\pm75_4/0)_T$ specimens results in dominant normal forces acting perpendicular to the fibres. In the $(0/\pm25_4/0)_T$ and $(0/\pm45_4/0)_T$ specimens the shear force component acting on the matrix parallel to the fibres becomes dominant. To fracture the matrix in the $(0/\pm25_4/0)_T$ and $(0/\pm45_4/0)_T$ specimens, a higher load is required.
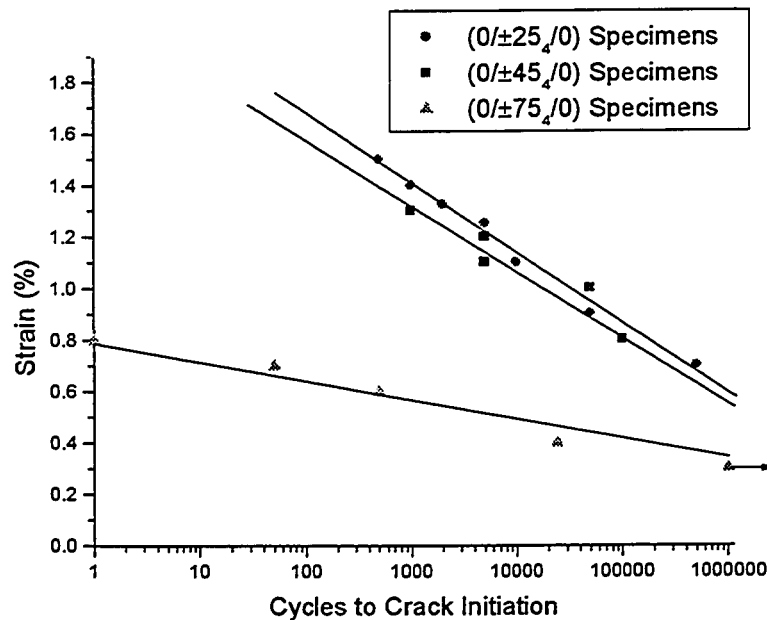
Figure 4.13: Crack initiation curves for the three types of specimens examined

4.4.5 Crack Saturation Damage Curves

Crack saturation curves were developed for all of the specimens. These are plotted in Figure 4.14.
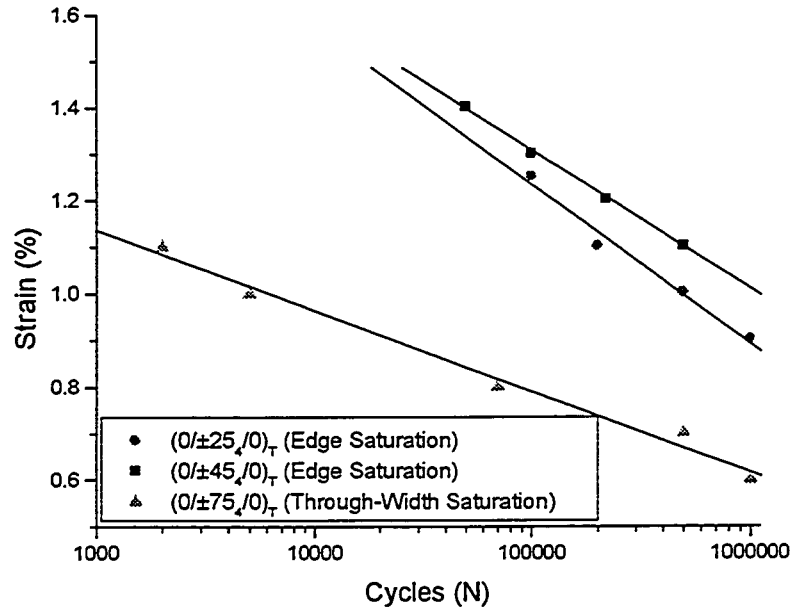
Figure 4.14: Crack saturation curves for $(0/\pm\theta_4/0)_T$ specimens

The saturation state requires a higher strain, as well as a longer life for the $(0/\pm25_4/0)_T$ and $(0/\pm45_4/0)_T$ specimens when compared with the $(0/\pm75_4/0)_T$ specimens. This trend is similar to the crack initiation curves shown in Figure 4.13.

For all three types of specimens a saturation state of edge cracks developed. Only the $(0/\pm75_4/0)_T$ specimen produced a visual state of cracking though the width of the specimen. Since it was known that the length of the specimen that could be viewed by the microscope was 7.5mm, a crack density value could be found by dividing the crack count by this length. Edge cracks were counted for each ply and then averaged to

determine the average crack density per ply vs. the number of cycles. Linear and logarithmic plots of this are shown in Figures 4.15 and 4.16 for the $(0/\pm25_4/0)_T$ specimens, in Figures 4.17 and 4.18 for the $(0/\pm45_4/0)_T$ specimens, and in Figures 4.19 and 4.20 for the $(0/\pm75_4/0)_T$ specimens, respectively.

It is important to remember when viewing these plots that these are only edge crack densities. The large differences in edge crack penetration aren't shown in these plots. There is much more damage growth and penetration in the $(0/\pm75_4/0)_T$ specimens than there is in the other two specimen geometries examined.
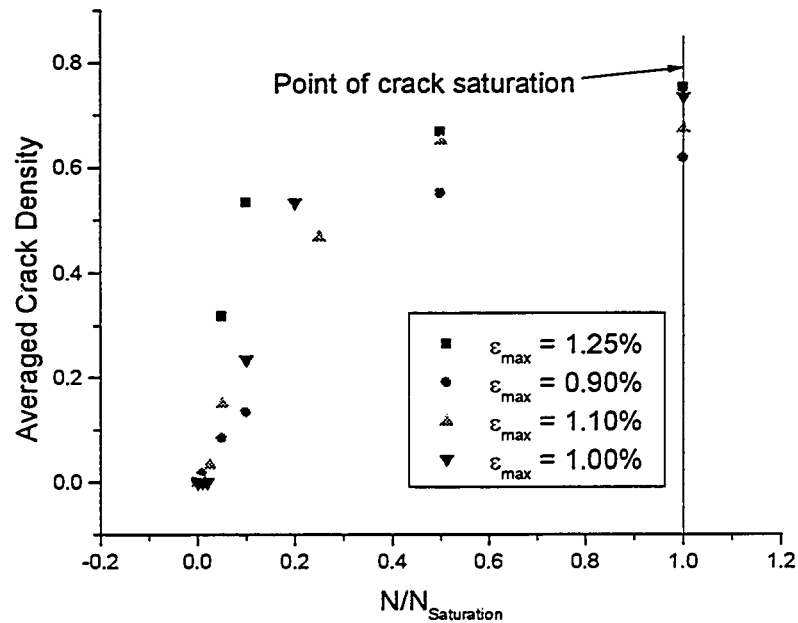
Figure 4.15: Linear plot of averaged edge crack density versus number of cycles normalized with respect to the saturation point for $(0/\pm25_4/0)_T$ specimens
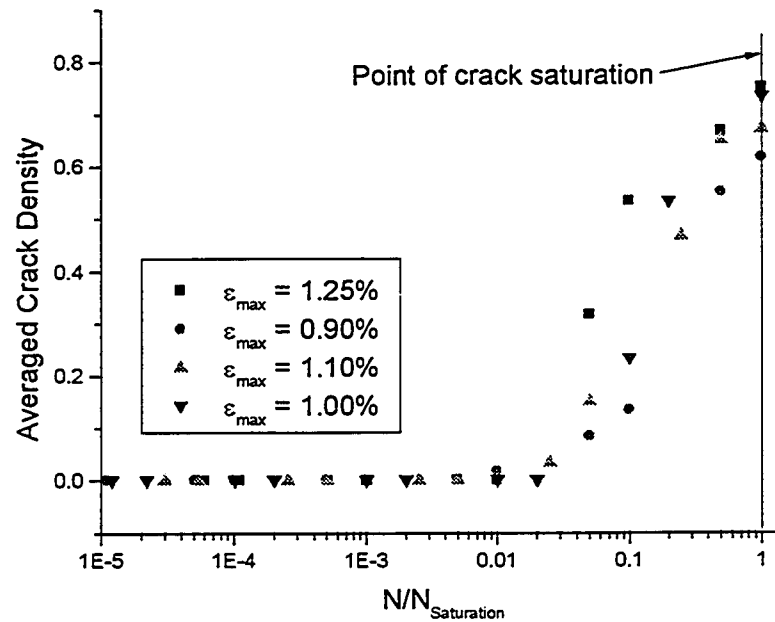
Figure 4.16: Averaged edge crack density versus log of number of cycles normalized
with respect to the saturation point for $(0/\pm25_4/0)_T$ specimens
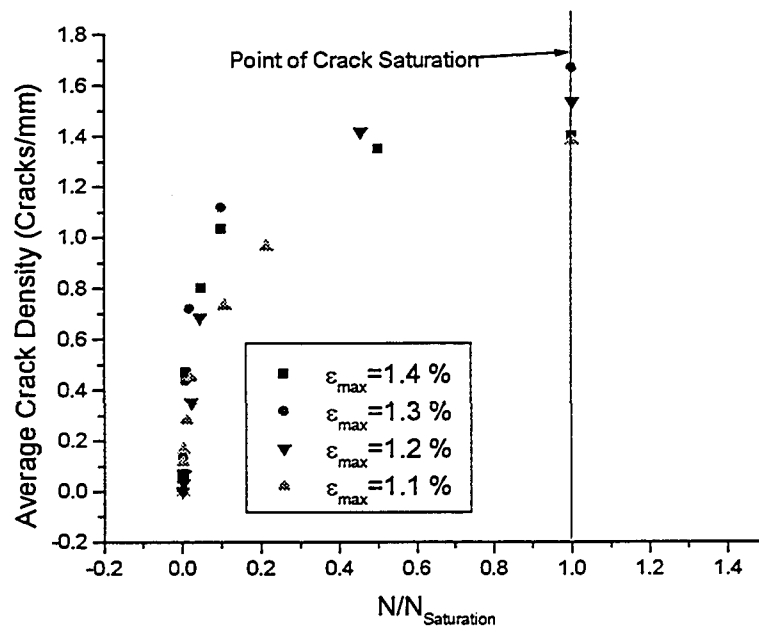
Figure 4.17: Linear plot of averaged edge crack density versus number of cycles
normalized with respect to the saturation point for $(0/\pm45_4/0)_T$ specimens
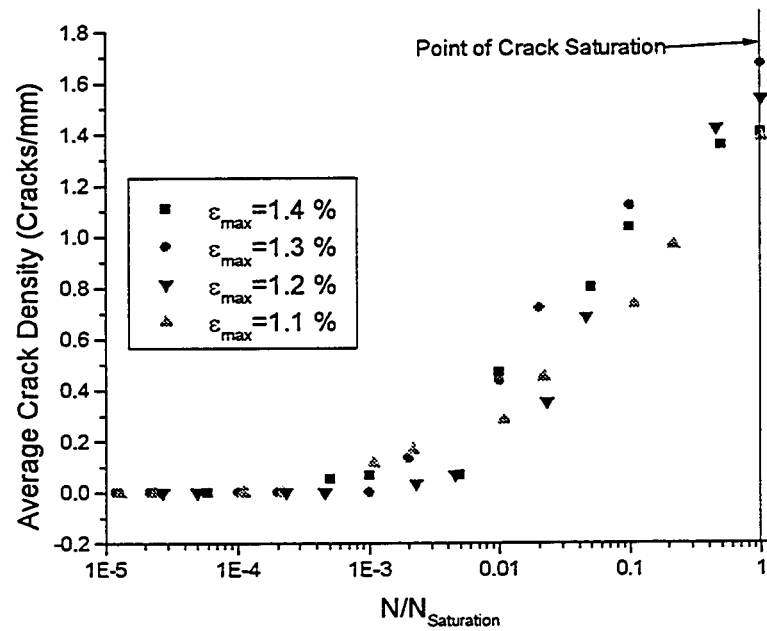
Figure 4.18: Averaged edge crack density versus log of number of cycles normalized with respect to the saturation point for $(0/\pm45_4/0)_T$ specimens
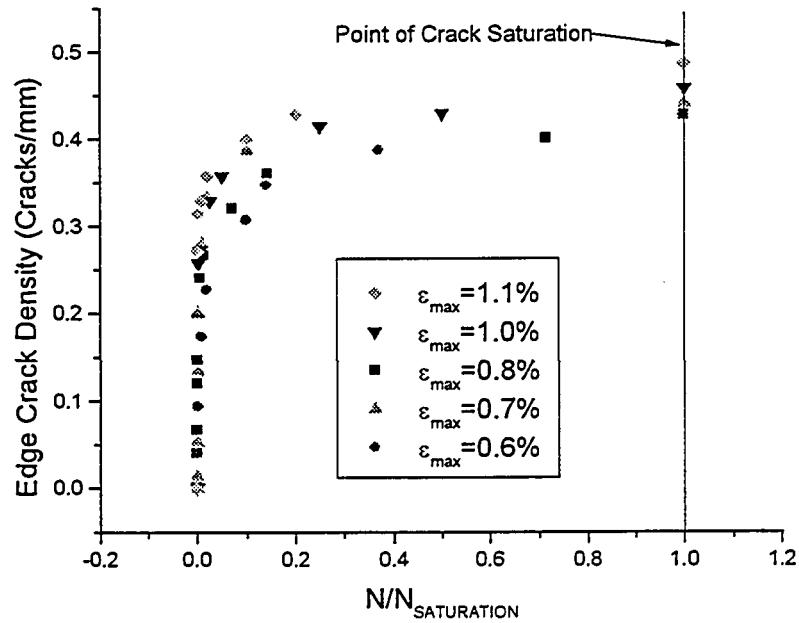
Figure 4.19: Linear plot of averaged edge crack density versus number of cycles normalized with respect to the saturation point for $(0/\pm75_4/0)_T$ specimens
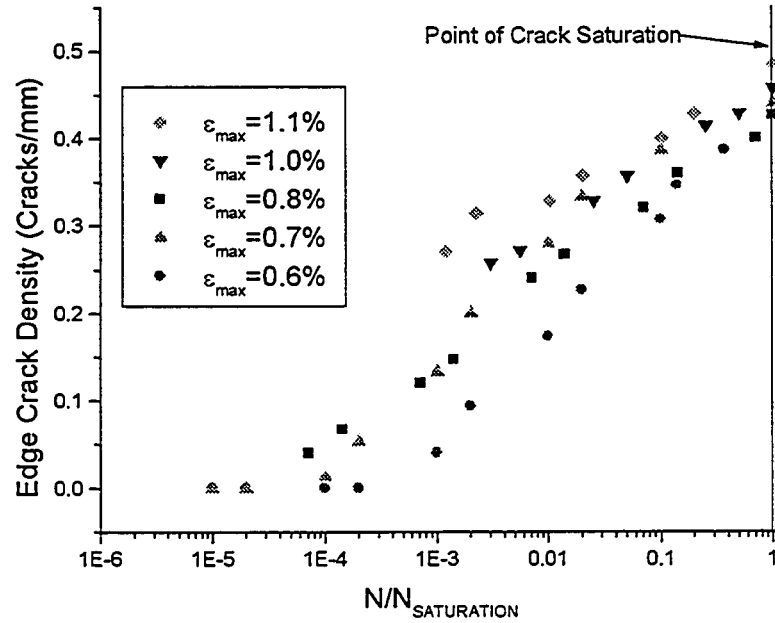
Figure 4.20: Averaged edge crack density versus log number of cycles normalized with respect to the saturation point for $(0/\pm75_4/0)_T$ specimens

All of the edge crack density plots, when plotted logarithmically, follow an S-shaped curve. In the first section there are no matrix cracks, a region before crack initiation. After this, a period of steep crack growth is observed, followed by levelling off and reaching a saturation state. When a specimen reaches its cracking saturation state, the predominant damage mode changes to delamination.

The edge crack density curves show a number of differences between the specimens. A comparison between the different angle plies and their respective crack densities are shown in Table 4.4. The variance in the fibre angles between neighbouring plies ($\Delta\theta$) is also included in the table to show what effect these have.

Table 4.4: Edge crack density comparison between different angle ply specimens

SPECIMEN TYPE	SATURATION EDGE CRACK DENSITY IN ANGLE PLIES. (CRACKS/MM)	$\Delta\theta$ PARALLEL TO DIRECTION OF LOADING. (DEGREES)
$(0/\pm25_4/0)_T$	0.72 ± 0.10	$50°$
$(0/\pm45_4/0)_T$	1.52 ± 0.15	$90°$
$(0/\pm75_4/0)_T$	0.46 ± 0.04	$150°$

For the $(0/\pm25_4/0)_T$ and $(0/\pm45_4/0)_T$ specimens the crack densities were increasing when the $\Delta\theta$ values were also increasing. When the $\Delta\theta$ values are small in the direction relative to the loading direction, the interlaminar stresses are reduced. This results in lower crack densities. These findings are similar to previous work by Hoover [22] for monotonic loading which found that crack densities, and damage in plies was lower for specimens which had neighbouring plies with angles of less than $30°$ between themselves. Although the angles between the neighbouring plies are larger than $30°$ in this study, there is still a marked reduction in crack densities when the angle between two adjacent plies is lower.

This theory applies for the $(0/\pm25_4/0)_T$ and $(0/\pm45_4/0)_T$ specimens, but it can be seen that the crack density in the $(0/\pm75_4/0)_T$ specimens is much lower. In these specimens the cracks propagated immediately through the thickness of the specimens. In these specimens only the outer $0°$ constraining plies enact large shear forces on the inner angle plies, resulting in a lower stress gradient, and less matrix cracking. This is similar to what was seen in $(0_2/90_n)_s$ specimens tested by M.C. Lafarie-Frenot and C. Henaff-Gardin [21]. In these specimens when the 'n' value increased, the crack density

decreased. In effect the angle ply layers in the $(0/\pm75_4/0)_T$ specimens are oriented similar enough to one another so as to act as a thick ply which results in less matrix cracking.

4.4.6 Delamination Initiation Damage Curves

Delamination curves for all of the specimens are shown in Figure 4.21. All examinations of delamination initiation were performed using the optical microscope. The first indication of separation between two plies was taken as the initiation of delamination.
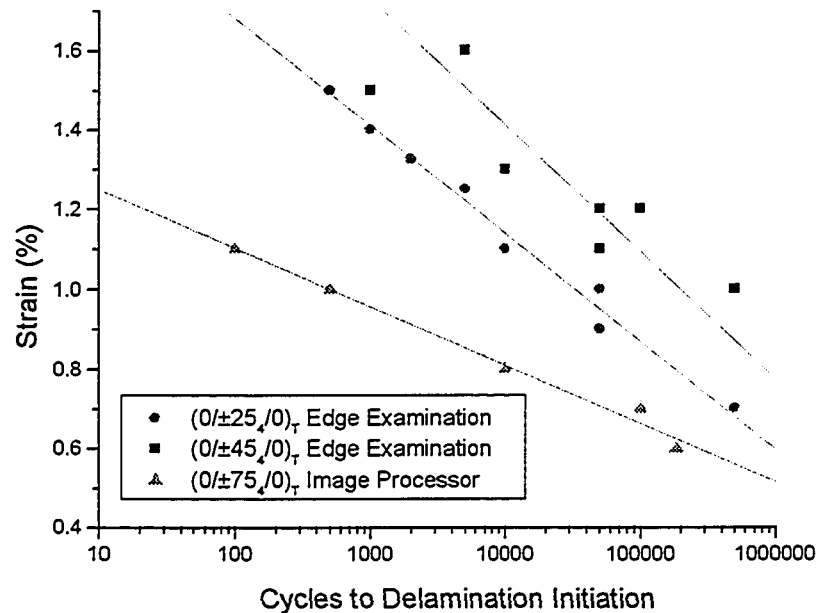
Figure 4.21: Delamination initiation curves for $(0/\pm\theta_4/0)_T$ specimens

Under cyclic loading there are many factors which contribute to delamination initiation and growth. In the tests performed, and in findings by others [11,36] it was found that delaminations initiated most easily along free edges and in the presence of

matrix cracks. The value of the interlaminar shear stress component plays a large role in the growth of the delaminations. There are many complicated factors that contribute to this stress gradient between plies. When the angle of neighbouring plies is similar, the stress gradient between them decreases. Another factor is residual stresses added during the cure cycle when manufacturing the specimen. The fibres and matrix in a composite have different thermal coefficients of expansion. When cooling from the melt temperature of the polymer residual stresses are introduced. The largest residual shear stresses are found between plies with large variance in fibre angles. As mentioned earlier, delamination is seen to initiate first in areas where there are matrix cracks. Once these cracks initiate, more of the load is transferred between plies through the shear stress. This is another factor that contributes to delamination initiation.

4.4.7 Stiffness Reduction Curves

Stiffness reduction curves were generated for all of the cyclic tests. By correlating the visual examination methods with the stiffness reduction curves a check could be used to make sure that the visual observations were consistent between tests.

Plots of the stiffness reduction curves for the $(0/\pm25_4/0)_T$, $(0/\pm45_4/0)_T$, and $(0/\pm75_4/0)_T$ specimens are shown in Figures 4.22, 4.24, and 4.26, respectively. The horizontal arrows indicate that ultimate failure of the specimens did not take place before 1×10^6 cycles. The vertical arrows indicate the point at which the visual examination technique showed the initiation of matrix cracking.

To examine how closely these values correlate with one another the life of the specimens were normalized with respect to the crack initiation life, $N/N_{(Crack\ Initiation)}$. The resulting curves for the three cases are shown in Figures 4.23, 4.25, and 4.27, respectively. In these figures the stiffness was normalized with respect to the initial stiffness found from each test. There is a clear correlation between the onset of matrix cracking and the initiation of stiffness reduction for all three specimens.

The $(0/\pm25_4/0)_T$ specimens showed a slight decrease in stiffness of approximately 2.5-3.0 GPa after the point of crack initiation. This small decrease in stiffness coincides with a small amount of matrix cracking in the specimen. Note that no through width cracking was observed, all cracking was mainly along the edges of the specimen, and they did not penetrate far into the specimen. This small amount of cracking results in a small stiffness reduction.

Figure 4.23 shows the same plot, this time normalized with respect to the crack initiation life. For all but the two specimens that were subjected to the smallest strains, the specimens followed a similar drop in stiffness. Of interest was the fact that specimens with strains lower than 0.9% had crack initiation, yet they had very little stiffness reduction. This suggests that the strains were either too low for enough cracking to take place to show a stiffness reduction, or the test had not progressed long enough to see a visible reduction in stiffness.
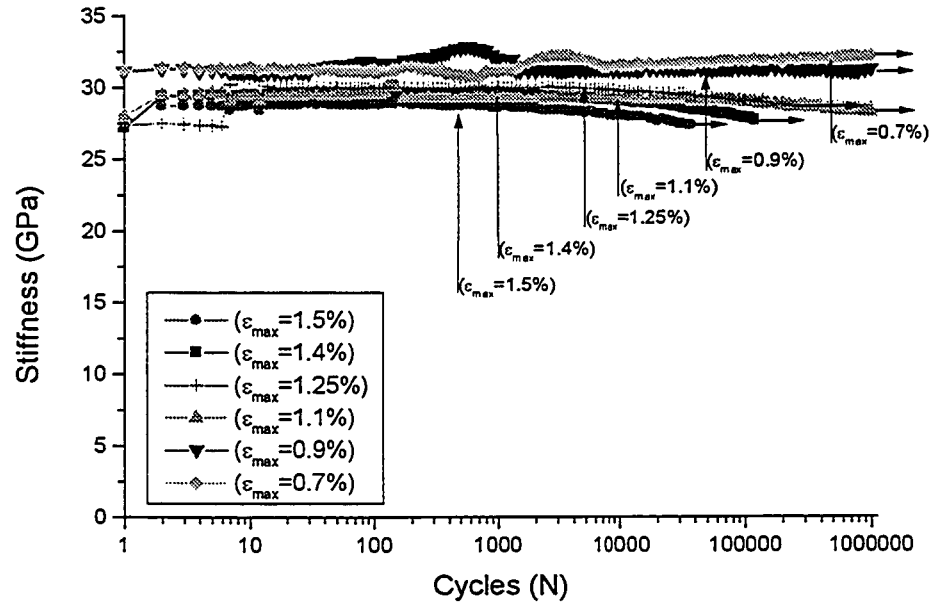
Figure 4.22: Stiffness reduction vs. cycles for $(0/\pm25_4/0)_T$ specimens under strain control
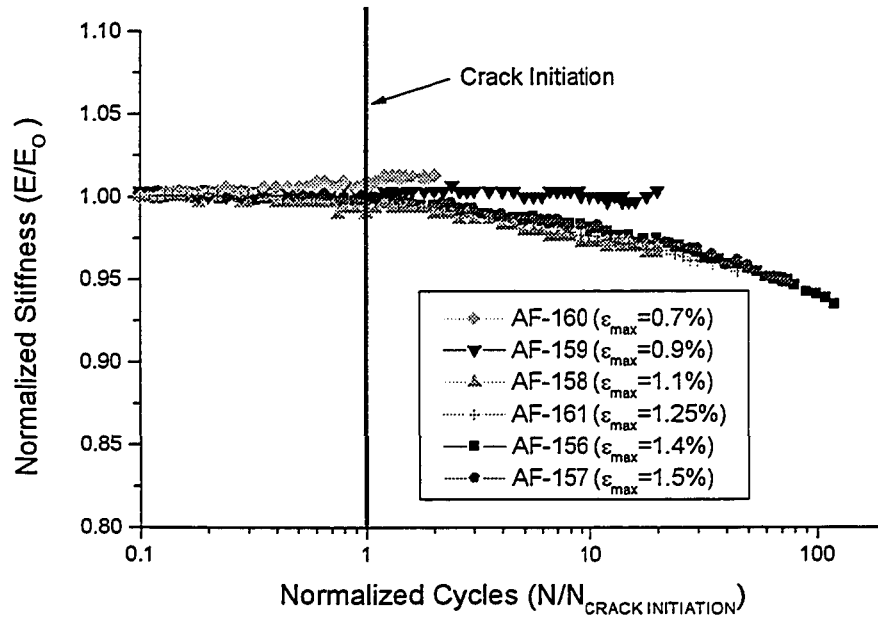
Figure 4.23: Normalized stiffness reduction vs. normalized cycles for $(0/\pm25_4/0)_T$ specimens under strain control

The stiffness reduction curves for the $(0/\pm45_4/0)_T$ specimens produced a larger reduction in stiffness relative to the initial stiffness than the $(0/\pm25_4/0)_T$ specimens. In these specimens the stiffness reduction is approximately 3.0 − 4.0 GPa. Although both geometries do not produce through-width matrix cracking, the larger reduction in stiffness is due to more matrix cracks along the edges of the specimens.

Figure 4.25 shows the normalized stiffness drop of the $(0/\pm45_4/0)_T$ specimens. There is a substantial stiffness drop of approximately 15% of the total stiffness. This drop correlates well between all of the applied strain levels.

Of note in the stiffness reduction plots for both the $(0/\pm25_4/0)_T$ and $(0/\pm45_4/0)_T$ specimens is that the stiffness reduction curves show no signs of levelling off. This suggests that the reduction may continue well after the imposed limit of 1×10^6 cycles. The edge crack saturation state has been shown to exist before 1×10^6 cycles suggesting that there is stiffness reduction due to either further crack propagation into the specimen, or due to delamination growth.

The stiffness reduction curves for the $(0/\pm75_4/0)_T$ specimens show a very significant reduction in stiffness soon after the initiation of matrix cracking. The decrease in stiffness is the largest for this geometry, approximately 6.0 - 7.0 GPa. This is 30-35% of the initial stiffness. This large stiffness reduction is the result of through width matrix cracking. Figure 4.26 shows that with these specimens there appears to be a point where saturation of matrix cracking takes place. The slopes have a distinct point where they level off, whereby there is no more stiffness reduction due to matrix cracking. Instead, a much slower reduction takes place due to delamination growth.
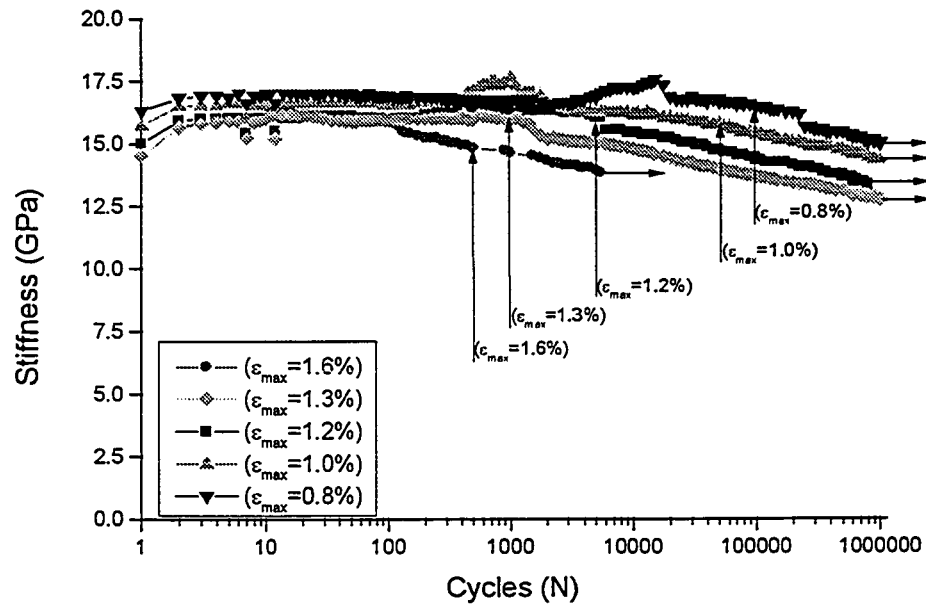
Figure 4.24: Stiffness reduction vs. cycles for $(0/\pm45_4/0)_T$ specimens under strain control
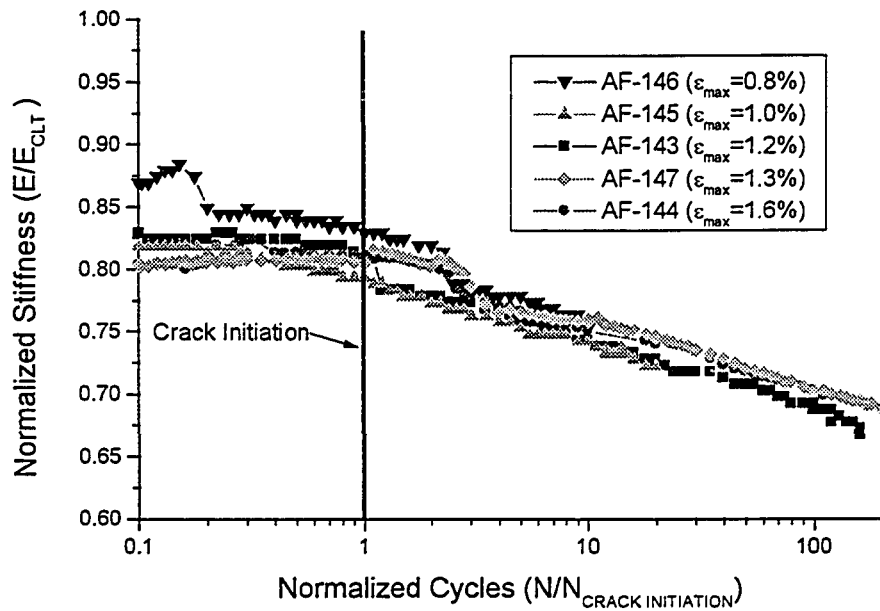
Figure 4.25: Normalized stiffness reduction vs. normalized cycles for $(0/\pm45_4/0)_T$
specimens under strain control
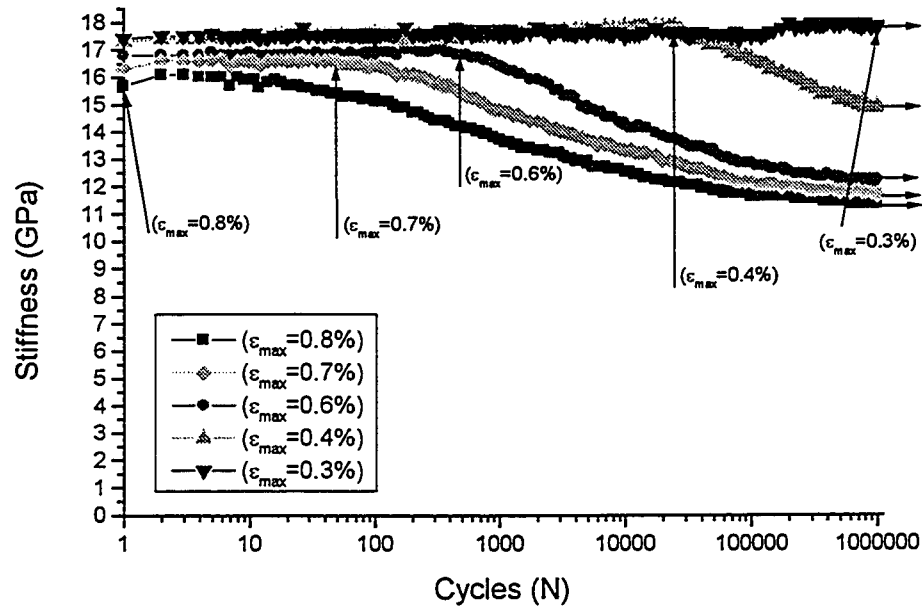
Figure 4.26: Stiffness reduction vs. cycles for $(0/\pm75_4/0)_T$ specimens under strain control
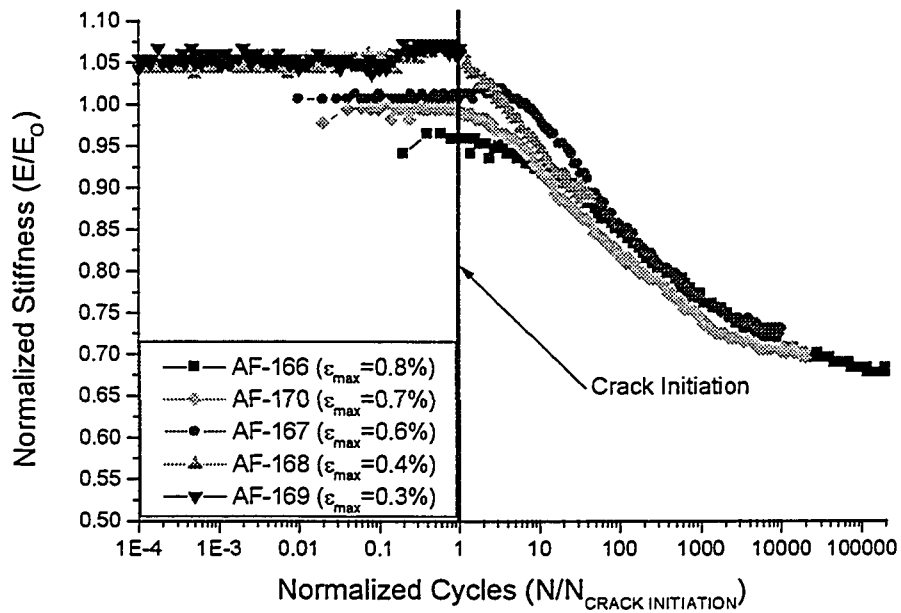
Figure 4.27: Normalized stiffness reduction vs. normalized cycles for $(0/\pm75_4/0)_T$ specimens under strain control

4.5   Summary

The study of constrained angle ply composites shows some very interesting results. By studying and documenting how the damage modes initiate and propagate a good idea of what factors affect damage growth was realized.

Visual damage examination during the life of the specimens found that the $(0/\pm25_4/0)_T$ and $(0/\pm45_4/0)_T$ specimens had damage growth only along the free edges. In contrast the $(0/\pm75_4/0)_T$ specimens produced a web-like crack pattern throughout the test section of the specimen. This was similar to what was seen in the monotonic tests.

Damage curves for crack initiation, crack saturation, and delamination initiation showed that the $(0/\pm75_4/0)_T$ specimens were the weakest orientation. The $(0/\pm25_4/0)_T$ and $(0/\pm45_4/0)_T$ specimens followed relatively similar curves for all of the damage modes investigated.

The overall strength of the specimens, when compared to the damage curves, matched up well with visual damage examination. Visual damage examination showed that only the $(0/\pm75_4/0)_T$ specimens produced any through-width matrix cracking, while the $(0/\pm25_4/0)_T$ and $(0/\pm45_4/0)_T$ specimens only produced visible damage growth along the edges of the specimens. In effect, the weaker specimen, the $(0/\pm75_4/0)_T$ laminate, did indicate larger amounts of damage propagation.

By examining the damage growth along the edges, a wavy pattern consisting of joined delaminations and matrix cracks was observed between the individual plies. The delamination joining the matrix cracks increased in height as the orientation of the angle plies decreased. Measurements of the height of these delaminations were taken for the

$(0/\pm25_4/0)_T$ and $(0/\pm45_4/0)_T$ specimens, and a simple calculation was done to determine the delamination penetration. It was found that the delaminations penetrated 0.148 mm for the $(0/\pm25_4/0)_T$ specimen and 0.122 mm for the $(0/\pm45_4/0)_T$ specimens. These were fairly similar distances suggesting that the crack growth in these specimens were mostly due to edge effects, that decreased as the distance into the specimen increased.

Comparisons of the crack initiation damage curves showed that the curves for the $(0/\pm25_4/0)_T$ and $(0/\pm45_4/0)_T$ specimens followed similar slopes, while the $(0/\pm75_4/0)_T$ specimen had a flatter slope with lower strains. This was due to the nature of the fracture in these specimens. Most of the load acting in the $(0/\pm75_4/0)_T$ specimens was normal to the fibres, resulting in matrix cracking under low loads. In the $(0/\pm25_4/0)_T$ and $(0/\pm45_4/0)_T$ specimens a larger total load was required to develop a similar load acting normal to the fibres.

Crack saturation curves were similar in slope to the crack initiation curves for the three specimens. The crack saturation life could be found by visually examining the edges of the specimens. Crack density plots showed that the final saturation state of cracking was the lowest in the $(0/\pm25_4/0)_T$ and $(0/\pm75_4/0)_T$ laminates. The $(0/\pm25_4/0)_T$ laminate had a low crack density due to 'compatible plies' which had relatively similar fibre orientations. These similarly oriented plies did not induce large variances in stress between neighbouring plies. The $(0/\pm75_4/0)_T$ specimens had a low crack density because the orientation of the 75° plies resulted in the crack immediately propagating through the thickness of the specimen. These plies acted as one very thick ply, where it has been shown that the thicker the ply, the more shear stress can be redistributed, and the lower

the crack density. The $(0/\pm45_4/0)_T$ specimens, which had 90° variances between plies had the largest crack densities.

The delamination initiation curves were amongst the hardest to determine. Delaminations were seen to always begin at free surfaces where matrix cracks had already developed. In the $(0/\pm25_4/0)_T$ specimens, delaminations were seen to initiate at the same time as crack initiation. For this to occur, the interlaminar stresses required to initiate delamination required would have to be of the same magnitude as in-ply stresses that initiated matrix cracks. The $(0/\pm45_4/0)_T$ specimens required the largest loads to initiate delamination, as shown in Figure 4.21. Earliest to initiate delamination were the $(0/\pm75_4/0)_T$ specimens. This is most likely due to high interlaminar stresses between the angle and constraining plies, as well as due to the high number of crack initiation sites where delaminations can grow from. Residual shear stresses during curing of the specimen are another factor that contributes to the growth of delamination in these specimens.

A strong correlation could be seen between visual damage mode examination and stiffness reduction. In all specimens the onset of cracking could be correlated with the initiation of stiffness reduction. Other damage modes such as delamination initiation and crack saturation proved difficult to correlate with changes in the rate of stiffness reduction in the $(0/\pm25_4/0)_T$ and $(0/\pm45_4/0)_T$ specimens. This was mainly due to the fact that the only visible damage growth in these specimens was along the edges, and the changing of damage modes along the edges had negligible effect on the rate of stiffness

reduction. In the $(0/\pm75_4/0)_T$ specimens a change in the dominant damage modes could be seen by a decrease in the slope of the stiffness reduction.

The magnitude of the stiffness drop in the specimens correlated with the amount of damage growth in the specimens. The $(0/\pm25_4/0)_T$ specimens with stiffness reductions of 2.5-3.0 GPa, had the lowest crack density of all three specimens, and didn't produce any visual through-width matrix cracks. The $(0/\pm45_4/0)_T$ specimens, with stiffness reductions of 3.0-4.0 GPa, had a large amount of edge cracks, yet no through width crack growth. Meanwhile the stiffness drop in the $(0/\pm75_4/0)_T$ specimens, which did have through width matrix cracking, produced a stiffness reduction of 6.0-7.0 GPa.

With respect to using angle ply composites in pressurized pipe design the coupon specimen tests performed here have limited use. For the $(0/\pm25_4/0)_T$ and $(0/\pm45_4/0)_T$ specimens the crack initiation and stiffness reduction results will have little applicability, mainly because the damage is largely related to the edge effect of the coupon. On the other hand, the results for the $(0/\pm75_4/0)_T$ specimens are applicable to a tubular specimen, since the initiation and propagation of damage was influenced very little by the edge effects.

5   Conclusions

The preceding chapters clearly show the complexity of damage initiation and propagation in composite laminates under cyclic loading. Damage growth occurs in four different damage modes: microdamage, matrix cracking, delamination, and fibre failure. These damage modes interact to form a complex failure pattern in the composite laminate.

The main purpose of this study was to determine stain/load vs. life curves for the different damage modes present in a composite laminate. By developing these damage curves for the differing geometries, and comparing with global parameters such as stiffness reduction data, a good appreciation was obtained with respect to how the damage spread through the specimens. Depending on the design conditions, certain modes of damage may be avoided, if an understanding of the damage initiation and growth is achieved.

5.1   Damage Initiation and Propagation in Multi-ply and Cross-ply Laminates

Damage growth under quasi-static and cyclic loading was examined for two different laminate geometries: $(0_2/90_3)_s$ and $(\pm45/90_3)_s$ laminates. The salient results from this series of experiments are presented in point form below:

- The initial damage mode in all of these specimens consisted of matrix cracking perpendicular to the direction of loading in the 90° plies. This damage mode

propagated into delamination growth between the inner 90° plies and the outer

constraining plies.

- The load required for the ultimate failure of the specimens was determined by the

  fibre orientations in the constraining plies. In the $(0_2/90_3)_s$ specimens ultimate failure

  was due to fibre failure in the constraining plies. In the $(\pm45/90_3)_s$ specimens ultimate

  failure was due to shear failure of the matrix in the constraining plies.

- Damage curve plots of the laminates indicated the relative life of each damage mode.

  All of the damage modes appeared to follow linear curves over the range of loads

  examined, except at very low loads. The $(0_2/90_3)_s$ specimens were found to require

  larger loads before damage initiated. This was due to the much higher stiffness

  associated with the outer constraining plies in this specimen. The 0° plies in the

  $(0_2/90_3)_s$ specimens contributed to a much higher global stiffness than the 45° plies in

  the $(\pm45/90_3)_s$ specimens. At very low loads the crack initiation points deviated from

  the curves and did not initiate cracks at the expected points. This suggests the

  presence of a crack initiation stress limit.

- A strain vs. cycles damage curve was plotted for the crack initiation points for all of

  the specimens geometries and loading modes examined. It was found that all of the

  points fell on a similar line, suggesting that the initial damage growth in all of these

  specimens occurred at the similar points irrespective of the constraining ply

  geometries or loading control mode (Stress or strain control).

- Examination of transverse crack growth showed that matrix cracks propagated rapidly

  throughout the specimens early on in the life. As the damage mode changed to

delamination, the matrix cracking rate decreased considerably. Any new damage was then seen as delamination.

- Saturation states of transverse matrix cracks were seen in the $(0_2/90_3)_s$ specimens under load control, and the $(\pm 45/90_3)_s$ specimens under strain control. In the $(\pm 45/90_3)_s$ specimens this was due to the control mode. As cracks grew in the plies, stress relaxation between cracks resulted in less new cracks forming, finally resulting in a saturation state of matrix cracks. In the $(0_2/90_3)_s$ specimens the strain that the outer $0°$ plies can withstand before failure is much higher than that of the $90°$ plies. The $90°$ plies produced a saturated state of matrix cracks before any significant damage started in the outer $0°$ plies. The only specimens not to produce a saturation state were the $(\pm 45/90_3)_s$ specimens under load control. The continuous increase in strain throughout the constraining plies led to continued matrix cracking up until ultimate failure in these specimens, and no saturation state resulted.

- All specimens examined were seen to produce bi-linear stiffness reduction curves. In the initial steeper section of the curve, stiffness reduction was due largely to matrix cracking in the $90°$ plies. The slope became less steep when the matrix crack growth slowed and delamination between the $90°$ plies and the constraining plies became the dominant damage mode. Both the $(0_2/90_3)_s$ and $(\pm 45/90_3)_s$ specimens experienced similar drops in the magnitude of the stiffness due to the matrix cracking. (5-7 GPa for the $(0_2/90_3)_s$ specimens and 8-9 GPa for the $(\pm 45/90_3)_s$ specimens. However, in

terms of percentage with respect to the undamaged stiffness, the reduction for $(\pm45/90_3)_s$ was 60% compared to 20% for $(0_2/90_3)_s$ laminates.

- Stiffness reduction vs. crack density plots showed a strong correlation between matrix cracking and any reduction in stiffness. Linear curves existed for all specimens. At either end of the curves the slopes deviated slightly from linearity. This was due to stiffness reductions due to the different damage modes of microdamage and delamination.

- Direct comparisons between the quasi-static and cyclic tests found some interesting differences. Cracks initiated at lower loads, and higher crack density was observed for a given maximum load under cyclic loading. More delamination growth was seen under cyclic loading than under quasi-static loading. For the latter loading, delamination damage growth was seen only at very high strains, very close to the ultimate failure of the specimens. In the cyclic tests the delamination damage mode comprised the largest proportion of the specimen life.

- By comparing the cyclic damage growth between the fibre dominated $(0_2/90_3)_s$ specimens and the matrix dominated $(\pm45/90_3)_s$ specimens, the effect of the fibre angle variation could be found. The two types of specimens showed large differences related to damage growth in their constraining plies. Initial damage growth due to transverse matrix cracking was similar in both specimens. When delamination growth began between the 90° plies and the constraining plies, large differences in delamination growth were seen.

- Comparisons of the $(\pm45/90_3)_s$ specimens under load and strain control found that larger lifespans were achieved under strain control loading, for a given initial stress/strain combination. The strain control tests exhibited stress relaxation as damage grew in the specimen, resulting in less damage growth as the life increased. The stress control tests exhibited ratcheting, resulting in increased strain, and hence increased damage over the life of the specimen.

5.2 Damage Initiation and Propagation in Constrained Angle-ply Laminates

Three constrained angle ply composites were examined. These had geometries of $(0/\pm25_4/0)_T$, $(0/\pm45_4/0)_T$, and $(0/\pm75_4/0)_T$. By varying the inner angles of these similar lay-ups it was possible to determine how the damage growth varied over a range of angles. For each of these laminates damage curves were developed for matrix crack initiation, matrix crack saturation, and delamination initiation. The following are the main results:

- Visual damage inspection of the specimens found that the $(0/\pm25_4/0)_T$ and $(0/\pm45_4/0)_T$ specimens produced visible damage only along the edges of the specimens, suggesting that edge effects played a large role in all damage growth in these specimens. In contrast, a web-like pattern of cracks were seen throughout the width and thickness of the angle-plies in the $(0/\pm75_4/0)_T$ specimens. These cracks were at 75° angles from the edges of the specimens and produced a highly visible saturated state of matrix cracking throughout the specimen.

- By producing damage curves for the specimens, it could be seen that the $(0/\pm75_4/0)_T$ specimens experience damage initiation under the lowest strains for all of the damage modes. This lay-up also required much lower loads for damage to propagate through the specimen.

- Crack initiation damage curves indicate that the $(0/\pm75_4/0)_T$ specimens produced matrix cracking at lower strains than the $(0/\pm25_4/0)_T$ and $(0/\pm45_4/0)_T$ specimens, which followed relatively similar curves. The reason for these differences was that the $(0/\pm75_4/0)_T$ specimens had orientations that exerted largely normal loads perpendicular to the matrix, whereas in the $(0/\pm25_4/0)_T$ and $(0/\pm45_4/0)_T$ specimens the load placed on the specimen was divided into normal and shear components. Therefore a larger total load was required to shear the matrix.

- Crack saturation damage curves produced similar slopes in relation to the crack initiation curves. Edge crack densities were determined at the saturation state. The edge crack densities were 0.72, 1.52, and 0.46 cracks/mm for the $(0/\pm25_4/0)_T$, $(0/\pm45_4/0)_T$, and $(0/\pm75_4/0)_T$ specimens, respectively. Crack densities were seen to be low in the $(0/\pm25_4/0)_T$ due to 'compatible plies' whereby the stress gradient between individual plies was low, resulting in a lower crack density. In the $(0/\pm75_4/0)_T$ specimens a low crack density occurred due to initial through thickness cracking. This resulted in lower stress gradients between individual plies, and a lower crack density.

- Delamination damage curves were developed for the three specimens. It was found in all cases that delaminations initiated at free edges, from the edges of matrix cracks.

The $(0/\pm 45_4/0)_T$ specimens required the largest loads to initiate delamination, suggesting that this lay-up can withstand very large shear forces between the plies. In the $(0/\pm 25_4/0)_T$ specimens the delamination damage initiated at the same point as crack initiation, suggesting that at these large angles the shear force required to initiate delamination, and the normal forces required to initiate matrix cracking are of similar magnitudes.

- Further damage examination showed that there was a wavy pattern of crack growth along the edges of all specimens, where through-ply matrix cracks met up with delaminations. This pattern produced delaminations of the longest length in the $(0/\pm 25_4/0)_T$ specimens, smaller delaminations in the $(0/\pm 45_4/0)_T$ specimens, and the smallest delaminations in the $(0/\pm 75_4/0)_T$ specimens. By measuring the length of these delaminations and knowing the fibre angles, an estimate of how far the damage penetrated into the specimens could be determined. The values found were 0.148mm and 0.122mm for the $(0/\pm 25_4/0)_T$ and $(0/\pm 45_4/0)_T$ specimens respectively, suggesting that there is a definite edge effect that occurs in these specimens.

- Stiffness reduction measurements indicated that there was a strong correlation between the stiffness reduction and the observed visual damage. The $(0/\pm 25_4/0)_T$ specimens which had stiffness drops of 2.5-3.0 GPa only experienced a low crack density of edge cracks. The $(0/\pm 45_4/0)_T$ specimens, with a drop of 3.0-4.0 GPa produced similar edge cracks with a higher crack density. In contrast, the $(0/\pm 75_4/0)_T$ specimens, which had the largest stiffness drop of 6.0-7.0 GPa developed through width cracking. A definite drop in stiffness could be correlated with the initiation of

matrix cracking.   Correlating the onset of other damage modes with the stiffness

reduction proved difficult, since new damage modes interacted with the prior damage

modes.   This interaction made it difficult to determine where one mode started and

another ended.

5.3   Suggested Future Work

The following are a few suggested future directions of research:

An area of pursuit that may prove profitable is comparisons of tubular and coupon

composite specimens.   In the constrained angle ply experiments many of the results

seemed to be largely dominated by edge effects.   With no edge effect the propagation of

damage in these specimens should be reduced, and designs can be further optimized.

This study used visual damage examination methods to examine damage growth

through the width of the $(0_2/90_3)_s$ and $(\pm45/90_3)_s$ specimens, and along the edges of the

$(0/\pm25_4/0)_T$, $(0/\pm45_4/0)_T$, and $(0/\pm75_4/0)_T$ specimens.   This method of damage

examination gives a good idea of the total damage occurring in the specimen, but it is

very hard to quantify the total damage throughout the specimen.   When the thickness of

each separate geometry grows smaller, there is less damage growth, and it becomes much

more difficult to detect the damage.   Unfortunately these thin plies are also the most

realistic in design, since they provide the strongest lay-ups.   Previous researchers have

used x-ray sources to develop images of the damage growth throughout the width and

thickness of the specimens.   By implementing this damage examination technique a

better idea of the damage growth inside the specimens can be determined. This method

of damage examination can be used on both tubular and coupon test specimens. A

description of this examination technique is discussed in Appendix A.

6   Bibliography

[1] H.T. Hahn and R.Y. Kim. Fatigue behaviour of composite laminate. Journal of Composite Materials, 10:156-180, 1976

[2] K.E. Jackson, S Kellas, and J. Morton. Scale effects in the response and failure of fiber reinforced composite laminates loaded in tension and in flexure. Journal of Composite Materials, 26:2674-2705, 1992.

[3] T.K. O'Brien and S. Salpekar. Scale effects on the transverse tensile strength of graphite/epoxy composites. In E.T. Camponeschi, Jr., editor, Composite Materials: Testing and Design (Eleventh Volume), ASTM STP 1206, American Society for Testing and Materials, Philadelphia, PA, pp 23-52, 1993.

[4] C.W. Dill, S.M. Tipton, E.H. Glaessgen, and K.D. Branscum. Fatigue strength reduction imposed by porosity in a fibreglass composite. In Damage Detection in Composite Materials, ASTM STP 1128, American Society for Testing and Materials, Philadelphia, PA., pp 152-162, 1992.

[5] J. Bai, P. Seeleuthner, and P. Bompard. Mechanical behaviour of $\pm 55°$ filament-wound glass-fibre/epoxy-resin tubes: I. Microstructural analysis, mechanical behaviour and damage mechanisms of composite tubes under pure tensile loading, pure internal pressure, and combined loading. Composites Science and Technology, 57:141-153, 1997.

[6] B.D. Harper, G.H. Staab, and R.S. Chen. A note on the effects of voids upon the hygral and mechanical properties of as4/3502 graphite/epoxy. Journal of Composite Materials, 21:280-289, 1987.

[7] M.A. Stone, I.F. Schwartz, and H.D. Chandler. Residual stresses associated with post-curing shrinkage in GRP tubes. Composites Science and Technology, 57:47-54, 1997.

[8] A.L. Highsmith, K.L. Reifsnider. Stiffness-Reduction Mechanisms in Composite Laminates, Damage in Composite Materials, ASTM STP 775, American Society for Testing and Materials, Philadelphia, PA, pp 103-117, 1982.

[9] K.L. Reifsnider. The Mechanics of Fatigue in Composite Laminates, Proceedings of Japan-U.S. Composite Materials conference, K.Kawata and T.Akasaka, Ed.,pp131-144, 1981.

[10] J. Zhang, C. Soutis, and J. Fan. Strain energy release rate associated with local delamination in cracked composite laminates. Composites, 25:851-862, 1994.

[11] S.A.Salpekar, T.K. O'Brien, and K.N. Shivakumar. Analysis of local delamination caused by angle ply matrix cracks. Journal of Composite Materials, 30:418-440, 1996.

[12] C.T. Herakovich. Failure modes and damage accumulation in laminated composites with free edges. Composites Science and Technology, 36:105-119, 1989.

[13] W. Becker and G. Kress. Stiffness reduction in laminate coupons due to the free-edge effect. Composites Science and Technology, 52:109-115, 1994.

[14] K.H. Boller. Fatigue Fundamentals for Composite Materials. Composite Materials: Testing and Design, ASTM STP 460, American Society for Testing and Materials, Philadelphia, PA, pp 217-235, 1969

[15] E.T. Camponeschi, W.W. Stinchcomb. Stiffness Reduction as an indicator of Damage in Graphite/Epoxy Laminates, Composite Materials: Testing and Design (Sixth Conference), ASTM STP 787, American Society for Testing and Materials, Philadelphia, PA, pp 225-246, 1982.

[16] R. Talreja. Transverse Cracking and Stiffness Reduction in Composite Laminates. Journal of Composite Materials, 19: 355-375, 1985.

[17] S.L. Ogin, P.A. Smith, P.W.R Beaumont. Matrix Cracking and Stiffness Reduction during the Fatigue of a (0/90)ₛ GFRP Laminate, Composites Science and Technology, 22: 23-31, 1985.

[18] L.E. Crocker, S.L. Ogin, P.A. Smith, and P.S. Hill. Intra-laminar fracture in angle-ply laminates. Composites Part A, 28A: 839-846, 1997

[19] J. Tong, P.A. Smith, S.L. Ogin, and F.J. Guild. A comparative study of matrix cracking under quasi-static and mechanical fatigue loading. Fatigue '96: Proceedings of the 6th international fatigue conference, G.Lutjering, H. Nowack (ed.), Pergamon press: pp.1573-1578, 1996

[20] V. L. Tahiri, C. Henaff-Gardin and M.C. Lafarie-Frenot. Damage and in-plane shear behaviour of a [±45°] carbon/epoxy laminate under quasi-static and fatigue tensile loadings. Fatigue '96: Proceedings of the 6th international fatigue conference, G.Lutjering, H. Nowack (ed.), Pergamon press: pp. 1561-1566, 1996

[21] M.C. Lafarie-Frenot, C. Henaff-Gardin. Formation and Growth of 90° Ply Fatigue Cracks in Carbon/Epoxy Laminates, Composites Science and Technology, 40: 307-324, 1991.

[22] J.Hoover. Angle Ply Cracking of $[\pm\theta/-45_3/+45_3]_s$ Glass Fibre/Epoxy Resin Laminates Subject to Monotonic Loading. University of Alberta Mechanical Engineering 409 Report: 1-24, 1996

[23] J.W. Hoover, D. Kujawski, F. Ellyin. Transverse cracking of symmetric and unsymmetric glass-fibre/epoxy-resin laminates. Composites Science and Technology, 57:1513-1526, 1997

[24] D. Kujawski. Width effects on the tensile strength and fatigue behaviour of angle-ply laminates. International Journal of Fatigue, 20:575-580, 1998

[25] D. Kujawski and F. Ellyin. Rate/Frequency-dependant behaviour of Fibreglass/epoxy laminates in tensile and cyclic loading, Composites, 26:719-723, 1995

[26] J.W. Hoover, J.D. Wolodko, F. Ellyin. Transverse Cracking of $[\pm\theta/90_3]_s$ Composite Laminates: Part I – Experimental Results 1999.(In preparation)

[27] C. Rorhbacher. Investigation of the effect of aqueous environment on glass-fibre reinforced epoxy resin. Department of Mechanical Engineering Report no. 102, University of Alberta, Edmonton, Alberta, 1998

[28] J.D. Wolodko, J.W. Hoover, F.Ellyin. Detection of Transverse Cracks in GFRP Composites using Digital Image Processing. Proceedings of ICM8 Conference, Volume II, F. Ellyin, J.W. Provan (ed.), Fleming printing ltd.:pp. 483-487, 1999

[29] J.D. Wolodko, Biaxial fatigue and leakage characteristics of fibre reinforced composite tubes. Ph.D. Thesis, University of Alberta, Edmonton, Alberta, 1999.

[30] J.W. Hoover, Transverse Cracking of $[\pm\theta/90_3]_s$ Composite Laminates. M.Sc. Thesis, University of Alberta, Edmonton, Alberta, 1999.

[31] D.J. Thornton, Finite Element Analysis of Fibre-Reinforced Composite Pipeline. M.Sc. Thesis, University of Alberta, Edmonton, Alberta, 1999.

[32] G.P. Sendeckyj, NDE Techniques for Composite Laminates. AGARD Conference Proceedings No. 355,London, United Kingdom, 2:1-22, 1983

[33] K.L Reifsnider and R. Jamison. Fracture of fatigue-loaded composite laminates. International Journal of Fatigue, 4: 187-197, 1982

[34] W.D. Rummel, T.L. Tedrow, H.D. Brinkerhoff. Enhanced X-Ray Stereoscopic NDE of Composite Materials. Air Force Wright Aeronautical Laboratories Technical Report, Wright Patterson Air Force Base, Ohio, pp 313-322, June 1980.

[35] C. Henaff-Gardin, M.C. Lafarie-Frenot, J.P. Amirault, D. Lang. Influence sur l'endommagement de stratifies carbone-epoxyde d'un radio-opacifiant a base d'iodure de zinc. Materiaux et Techniques, 82: 20-24, 1994

[36] C. Scarponi, R. Barboni, Delaminations onset and propagation for CFRP angle ply laminates under uniaxial fatigue loads. Journal of reinforced plastics and composites, 16:1181-1195, 1997

APPENDIX A

A variety of damage examination techniques were investigated, some of which performed well and were adopted herein, and some whose performance was not deemed satisfactory. This section includes those damage examination techniques which were not used, as well as some examination techniques that were not fully examined, yet may prove useful in future examination of damage initiation and propagation in composite structures.

1.0   X-Radiography of Specimens

A NDE technique that has become increasingly popular with composite materials testing is radiography. Radiography consists of bombarding a composite structure with X-rays, similar to medical examination of human bone structures. By taking x-rays successively throughout a cyclic test, or by just taking a single x-ray at some point in the test a good representation of crack growth in the specimen can be found.

A correctly exposed x-ray had two variables that can be adjusted: the voltage inputted to excite the x-rays, and the time the x-rays are subjected on the specimen. Research showed that by decreasing the voltage, and increasing the exposure time, the contrast between the crack and the composite material is increased. Typical x-ray parameters for composite specimens are around 10-20 KV, with exposure times between 30 and 60 seconds.

A problem with radiography of composites was that both the glass-fibres and the resin matrix absorb X-radiation only slightly differently than does air. To remedy this a

contrast enhancing material needed to be introduced. Studies found that the best method was the addition of a contrast enhancing penetrant into the crack voids [34].

Various X-ray penetrants have been used in the past:

- Tetrabromoethane – (TBE)

- 1,4 Diiodobutane – (DIB)

- Diiodomethane – (methylene iodide)

- Amipaque (Metrizamide)

Unfortunately all of these materials are halogenated organic compounds which are carcinogenic and dangerous to deal with.

A recipe for X-Ray Penetrant using Zinc Iodide was found to work well for Sendeckyj [32]. The Zinc Iodide penetrant solution is non-carcinogenic, has both polar and non-polar solvent properties that allow good penetration, and it also has high x-ray absorption characteristics. The mixture used in initial tests at the University of Alberta was as follows:

Zinc Iodide (ZnI_2)	- 60 grams
Water (H_2O)	- 10 mL
Isopropyl Alcohol	- 10 mL
Kodak "PhotoFlo 200"	- 1 mL

Results show that this penetrant was able to soak into most matrix cracks. Early x-ray pictures displayed penetrant that had entered through-width matrix cracks. This penetrant was thicker near the edges of the specimen than it was at the center. This suggests that there is a decreasing penetration rate, which could result in incomplete

damage characterization. Further research needed to be done on this subject to see the total effect of penetration.

The method has proved useful to other researchers when examining very thin ply thickness specimens. Optical image processing becomes increasingly difficult when the ply thickness is thinner, due to reduced contrast between the crack and the matrix. As well, in carbon-fibre composites, which aren't transparent, this is the only method of examining new crack growth.

Work using radiography to examine matrix cracking in composites has been done previously by Reifsnider and Jamison [33], Rummel, Tedrow, and Brinkerhoff [34], and Lafarie-Frenot, Henaff-Gardin et al [20,21,35]. Previous X-ray test parameters are presented in the following table:

RESEARCHERS: RUMMEL, TEDROW, BRINKERHOFF				
Penetrant: ZnI_2 mixture				
X-ray source: Balteau 5-50 kV, 20 Amp				
Film: Kodak Industrex R, double coated film w/ automatic processing.				
# of Plies	Killivolts	Milliamps	Exposure Time	Focal Distance
8	15	20	240 s	127 cm
16	15	20	480 s	127 cm
24	15	20	960 s	127 cm

RESEARCHERS: REIFSNIDER, JAMISON				
Penetrant: ZnI_2 mixture				
X-ray source: Hewlett Packard Faxitron				
Film: Kodak Industrex R, double coated film.				
# of Plies	Killivolts	Milliamps	Exposure Time	Focal Distance
8	25	25	30 s	?

RESEARCHERS: HENAFF-GARDIN, M.C. LAFARIE-FRENOT, ET AL.				
Penetrant: ZnI_2 mixture				
X-ray source: Pantak HF 100				
Film: Kodak Industrex R, double coated film.				
# of Plies	Killivolts	Milliamps	Exposure Time	Focal Distance
18	13	35	42 s	?

Because of limitations on the type of machine that was accessible, as well as types of films available, the following configuration was used in University of Alberta tests:

RESEARCHERS: WHARMBY, WOLODKO, ELLYIN				
Penetrant: ZnI_2 mixture				
X-ray source: Pantak HF 100				
Film: Kodak X-Omat AR-2 double coated film with automatic processing.				
# of Plies	Killivolts	Milliamps	Exposure Time	Focal Distance
8-10	50	10	3 s	94 cm

These parameters were found found to give poor contrast between the cracks and the composite material, especially as the thickness of the cracks grew smaller with decreasing number of similar plies.

2.0   Fluorescent Penetrant

Fluorescent penetrant had been examined as a method of examining crack initiation and growth in a specimen. By coating a specimen in the fluorescent penetrant and then placing the specimen under a dark-light. This method has proved useful in examining the damage growth in tubes undergoing pressure loading. The fluorescent penetrant is placed inside the specimens and as the fluid leaks out it shows where the damage is. In the coupon tests the fluorescent penetrant didn't prove to be any more

effective than the visual penetrant, while still requiring the darklight to view where it had penetrated the specimen.

3.0 Edge Replication of the Specimens

Edge replication of specimens is a method of recording crack initiation and growth along the edges of specimens. This is done by holding replicating tape over acetone fumes that soften the tape, then applying the tape to the side of the specimen and letting it harden. The hardened acetone records the crack pattern along the edge of the specimen. This method can be hard to perform, since the tape curls and is hard to place on the specimen.

4.0 Acoustic Emissions

Detection of damage by acoustic emissions consists of picking up noise emitted from the specimen due to microcracking as the specimen is damaged. Triangulation of individual microphones can be used to determine the location of damage growth, although when more than one crack emits noise at the same time the exact location of crack growth can become difficult to determine. This method is a good indicator of when significant damage happens (large acoustic emission), although it gives very little information about the nature of the damage growth.

5.0   Thermography

Damage detection by thermography is performed by examination of heat flow through the composite material. Temperature contours of a specimen can be detected and mapped out using either photochromatic coatings or infrared photography.

Two different approaches to this method exist. One of them examines damage growth due to hysteresis heating of the specimen, whereby internal heat generation causes the stress contours. The other approach is to induce a heat flow through the specimen. This idea relies on the fact that any defects and damage in the composite can restrict heat flow and these temperature contours can be seen. This method provides no information of the type of damage growth, and details of the damage magnitude are very poor.

6.0   Ultrasonic testing

Ultrasonic testing is a damage examination technique whereby a high frequency sound beam is directed through a composite, and the affected waveform is picked up on the other side of the specimen. Any changes in the waveform can be correlated with damage growth in the specimen. This method has proven most useful in delamination detection, since the delaminations affect a large in-plane section between two plies. Damage such as matrix cracking, which is thin in relation to the outer surface of the specimen, is very hard to detect unless the resolution of the ultrasonic testing is very fine. A problem with this detection method is that careful control of the acoustic parameters must be adhered to, since any variances can cause inaccuracy in damage predictions.

7.0   Sectioning

Damage examination by sectioning consists of soaking a specimen in visual penetrant and then cutting the specimen into sections for examination under the microscope. This has been shown to provide an accurate description of the matrix cracking and delamination damage in a cross-section of a specimen. It is a very difficult method to implement, mainly because new damage can be introduced when the sectioning operation is being performed. As well, it is a destructive damage examination technique that prevents further examination of the specimen.

8.0   Deplying

Deplying is a destructive damage examination technique. This method of specimen examination consists of soaking a specimen in a penetrant solution of gold chloride diethylether, then performing a burn-out test on the specimen. This removes the resin from the specimen, so that each of the individual plies can be removed. The residual gold penetrant remains showing where damage such as matrix cracking, delamination, and fibre failures had been. The benefits of this method are that it provides extremely accurate information on matrix cracking, and delamination in a specimen. The drawbacks are that because it is a destructive damage examination technique, it can't be used to document damage accumulation in a specimen.